DALHOUSIE UNIVERSITY

Tiny Recorder of the Evolution of Major Crustal Faults in the Bhutan Himalaya: An Integrated Mineralogical, Morphological, and Geochemical Study of Clay Minerals from fault gouges

Yuqiu Zhao

SUBMITTED IN PARTIAL FULFILLMENT OF THE REQUIREMENTS FOR
THE DEGREE OF BACHELOR OF SCIENCES, HONOURS
DEPARTMENT OF EARTH SCIENCES
DALHOUSIE UNIVERSITY, HALIFAX, NOVA SCOTIA

April 2017

Distribution License

DalSpace requires agreement to this non-exclusive distribution license before your item can appear on DalSpace.

NON-EXCLUSIVE DISTRIBUTION LICENSE

You (the author(s) or copyright owner) grant to Dalhousie University the non-exclusive right to reproduce and distribute your submission worldwide in any medium.

You agree that Dalhousie University may, without changing the content, reformat the submission for the purpose of preservation.

You also agree that Dalhousie University may keep more than one copy of this submission for purposes of security, back-up and preservation.

You agree that the submission is your original work, and that you have the right to grant the rights contained in this license. You also agree that your submission does not, to the best of your knowledge, infringe upon anyone's copyright.

If the submission contains material for which you do not hold copyright, you agree that you have obtained the unrestricted permission of the copyright owner to grant Dalhousie University the rights required by this license, and that such third-party owned material is clearly identified and acknowledged within the text or content of the submission.

If the submission is based upon work that has been sponsored or supported by an agency or organization other than Dalhousie University, you assert that you have fulfilled any right of review or other obligations required by such contract or agreement.

Dalhousie University will clearly identify your name(s) as the author(s) or owner(s) of the submission, and will not make any alteration to the content of the files that you have submitted.

If you have questions regarding this license please contact the repository manager at dalspace@dal.ca.

Grant the distribution license by signing and dating below.

Yuqiu Zhao	April 28, 2017
Name of signatory	Date

DALHOUSIE UNIVERSITY

Department of Earth Sciences
Halifax, Nova Scotia
Canada B3H 4R2
(902) 494-2358

DATE: 28 April 2017

AUTHOR: Yuqiu Zhao

TITLE: Tiny Recorder of the Evolution of Major Crustal Faults in the Bhutan Himalaya: An Integrated Mineralogical, Morphological, and Geochemical Study of Clay Minerals from fault gouges

Degree: B. Sc. Honours Earth Sciences Convocation: May Year: 2017

Abstract

The Himalayan Orogen was formed during ~ 50 million years of the on-going collision of India and Eurasia plates. The detachment at the base of the Himalayan orogenic wedge is the major active fault called the Main Himalayan Thrust (MHT). Its movement transferring gradually from ductile shear zone in the metamorphic orogenic core to brittle upper crust caused the formation of sequence of ductile shear zone and brittle thrust faults. From north to south, from older to younger, these mainly include the Main Central Thrust (MCT), the Main Boundary Thrust (MBT), and the Main Frontal Thrust (MFT). The Himalayan frontal faults, MBT and MFT, are the most important places for the study of how brittle fault formed and even understanding seismicity in the Himalayan orogen, due to its crucial role on accommodating deformation. This paper aims to characterize the mineralogy, morphology and geochemistry of clay minerals dominant in fault gouges, in order to understand the evolution of brittle fault and to reconstruct the conditions of faulting, as well as to further date faults for a larger project.

To identify clay and associated minerals, X-ray diffraction (XRD) analysis was primarily used, combining with petrographic microscope, scanning electron microscopy and energy dispersive spectroscopy (SEM/ EDS), and transmission electron microscopy (TEM). For the condition of clay formation, hydrogen (δD) and oxygen ($\delta^{18}O$) stable isotope analysis was also applied. The mineralogical and morphological investigations of 11fault gouge samples from the major crustal faults in the eastern Bhutan suggest that the fault gouges and protoliths are clay dominant with two types: (a) 2:1 layers, smectite, illite-smectite, and illite and (b) 1:1 layers, kaolinite. Both illite and kaolinite present in all samples, and illite and illite-smectite coexist only in Siwalik samples 182 while illite and smectite only in MFT samples 89. Such mineral aggregations suggest that no metamorphism happened but clay authigenesis occurred in fault gouges, combining with $\delta^{18}O$ and δD data. For the three samples that have three grain size fractions (0.1μm, 0.4μm, &2μm), the $\delta^{18}O$ and δD isotopic data show that there is no evident relation between grain size and isotopic composition. The isotope fractionation processes that occurred between fluids and clay minerals, establish the relation of the isotopic composition of clay minerals and the conditions of clay formation. Based on both smectite and kaolinite geothermometers, the equilibration temperatures of clay formation show two main results: 1) only the MFT sample 89C may have formed near surface at the lowest temperature, 35. 8 °C (± 1.6°C)$_{sm}$ and 20.6 °C (± 1.6°C)$_{K}$; 2) other samples yield the same result that they have formed

within the equilibration depth of ~ 2 km with ~ 35 °C − 46.3 °C (± 1.6°C)$_K$ of other samples. Using only known kaolinite fractionation factors, the isotopic composition of the meteoric waters is obtained with -10.6 − -9.0 ‰ $\delta^{18}O_{K\text{-}W}$ and -74.8 − -62.2‰ $\delta D_{K\text{-}W}$. It suggests that the paleo-meteoric water was derived from elevations between 2000 and 2500 m, which are ~1500 – 2000 m higher than the outcrops of fault gouges. Therefore, the formation condition of fault gouges is reconstructed, and it is concluded that the fault gouges have formed within the equilibration depth of ~ 2 km and at ~ 3 km or longer horizontal distance from the site of the source of the paleo-meteoric waters. However, the deduction would not work for the MFT fault gouge, which was formed after the MBT and is still active, due to the fault barriers between the source site of paleo-meteoric water and the MFT. Therefore, the interpretation of the stable isotopic compositions of clays from the MFT fault gouge requires further research.

Keywords: Clay gouges, Authigenic illite, Meteoric water, Isotopic composition, XRD

TABLE OF CONTENTS

Table of Figures

Chapter 1: Introduction

Chapter 2: Geological Setting

Chapter 3: Methodology

Chapter 4: Results

Chapter 5: Discussion

List of Tables

List of Abbreviations

Mineral Abbreviations with Chemical Formula

Sm	Smectite	$(0.5Ca,Na)_{0.7}(Al,Mg,Fe)_4[(Si,Al)_8O_{20}]nH_2O$
I/S	Illite-Smectite	
I	Illite	$K_{1-1.5}Al_4[Si_{7-6.5}Al_{1-1.5}O_{20}](OH)_4$
K	Kaolinite	$Al_2Si_2O_5(OH)_4$
Chl	Chlorite	$(Mg,Al,Fe)_6[(Si,Al)_4O_{10}](OH)_8$
M	Mica	
	Muscovite	$KAl_3Si_3O_{10}(OH)_2$
	Glauconite	$(K,Na)(Fe^{+3},Al,Mg)_2(Si,Al)_4O_{10}(OH)_2$
	Phlogopite	$K(Mg,Fe^{+2})_3[Si_3AlO_{10}](OH,F)_2$
Qtz	Quartz	SiO_2
F	Feldspar	
	Orthoclase	$K(Al,Fe)Si_2O_8$

Term Abbreviations

MHT	Main Himalayan Thrust
MCT	Main Central Thrust
MBT	Main Boundary Thrust
MFT	Main Frontal Thrust
STD	South Tibetan Detachment
KT	Kakhtang thrust
RT	Ramgarh Thrust
LHD	Lesser Himalayan duplex
TSS	Tethyan Sedimentary Sequence
GHS	Greater Himalayan Sequence
LHS	Lesser Himalayan Sequence
XRD	X-ray diffraction

NaOCl	Sodium hypochlorite bleach
G	Glycol Treatment
H	~550° Heating
SEM	Scanning Electron Microscopy
EDS	Energy Dispersive Spectroscopy
TEM	Transmission Electron Microscopy
GMWL	Global Meteoric Water Line
LMWL	Local Meteoric Water Line
S/H	Supergene/hypogene
VSMOW	Vienna Standard Mean Ocean Water

Acknowledgement

I would like to express my sincere thanks to my supervisor, Dr. Djordje Grujic, for providing me with the research opportunity to work on such a worthwhile project, for guiding me through the whole research project with his expertise, rich research experience, and patience, and for understanding and encouraging me to make substantial progress, especially during the tough writing period. His guidance and help have made completing my honours program a valuable and fun learning experience. He helped me a lot not only in improving academic research skills, but also in communication skills.

I would like to thank another my supervisor, Dr. Catherine Mottram, who have helped me a lot with lab instructions and technical support in the various tasks I have worked over the course of summer research and honour program. Working with her, I studied a lot from her rigorous research attitude and active thinking way.

I would also like to thank Dr. Isabelle Coutand for providing us with good experimental space and for helping us timely solve lab-related issues. I also thank Dr. Ricardo Silva for his guidance and help for the questions related to clay minerals. Thank you to Technologists Andrew George and Thomas Duffett for assistance and advice in my research processes.

Finally, I would like to express my hearty gratitude to all the professors and instructors who put faith in me and encourage me in the process of learning and experiencing the beauty of Earth Science.

Chapter 1: Introduction

The Himalaya mountain belt is one of the most dramatic creations of intercontinental collision with east-west trending shear zones and high altitude. It is the youngest and tectonically most active large hot orogen recording complex geological features and structures. Its growth involved a series of tectonic processes: crustal shortening, energy accumulation, pervasive ductile deformation, large-scale thrusting, uplifting, and high-temperature metamorphism (Yin & Harrison 2000; Hodges, 2000). However, there is still a lot of unknown locked in rocks and hidden in structures in the Himalayan Orogen. For example, while the deformation history of the ductile shear zones is fairly well constrained, the timing of the brittle thrust at the orogenic front is not known. My research is part of a larger international project, which is primarily concerned with the movement history of frontal major crustal faults in the eastern Himalaya. The main research questions are about how and under what conditions fault gouges formed in the frontal Himalaya.

1.1 Why Study Fault Evolution in the Eastern Himalayan Orogen

The Himalayan Orogen was formed during the approximately 50 million years of the on-going collision of two continental tectonic plates, India and Tibet (Najman et al., 2010; Figure 1.1). As a result of its growth with about 2500 km length, the largest thrust fault system extending along the whole orogen was produced in sequence, propagating from north to south. The detachment at the base of the Himalayan orogenic wedge is the major active fault called the Main Himalayan Thrust (MHT) (Nelson et al., 1996; Figure 1.2). Its movement transferring gradually from ductile shear zone in the metamorphic orogenic core to brittle upper crust caused the formation of sequence of ductile shear zone and brittle thrust faults. From north to south, from older to younger, these mainly include the Main Central Thrust (MCT), the Main Boundary Thrust (MBT), and the Main Frontal Thrust (MFT) (Hodges, 2000; Figure 1.2). The durations of ductile shearing along the three main structures have been fairly well constrained by in situ dating of zircon and monazite: respectively 23 Ma – 14 Ma for the MCT, less than 12 Ma for the MBT, and less than 2 Ma for the MFT (Grujic et al., 2011; Mottram et al., 2014; Mottram et al., 2015; kellett et al., 2009; Tobgay et al., 2012; Figure 1.2). With the average shortening rate of ~ 20 mm/yr (Robinson and McQuarrie, 2012), the development of these parallel thrust accommodated at least 1400 km of the north-south shortening caused by northward movement of

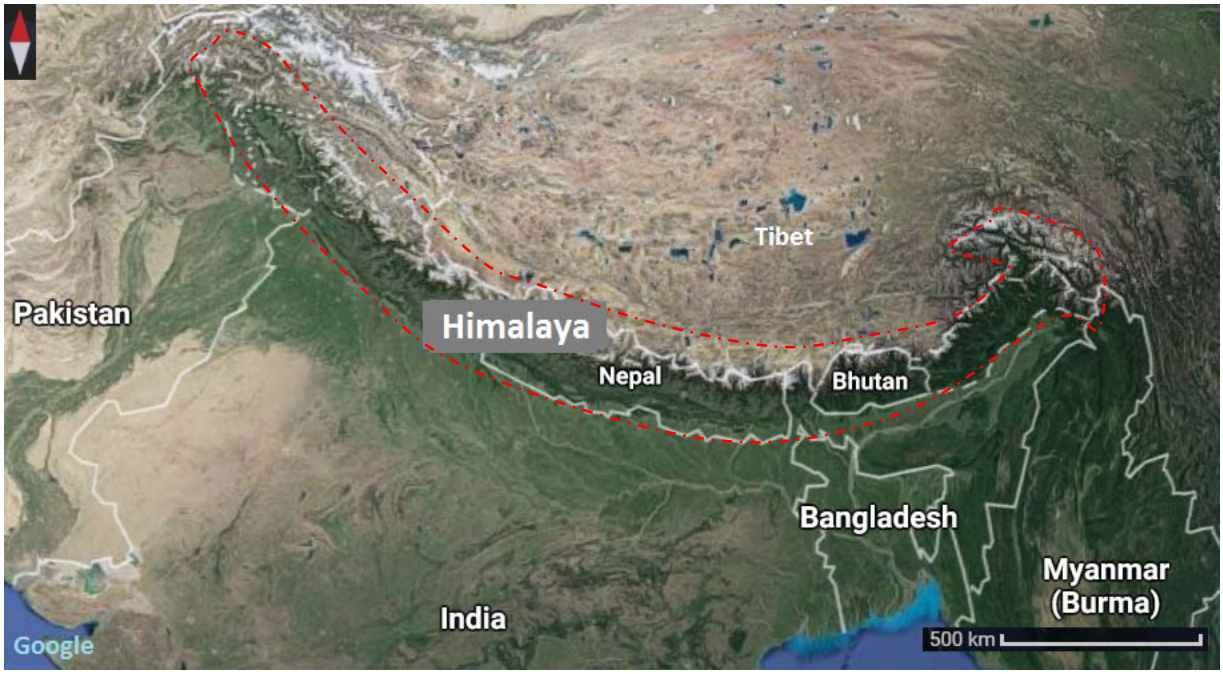

Figure 1.1 The Himalayan Orogen with ~ 2500 km length formed by the on-going collision of India plate and Tibetan plateau (Modified after Google satellite map).

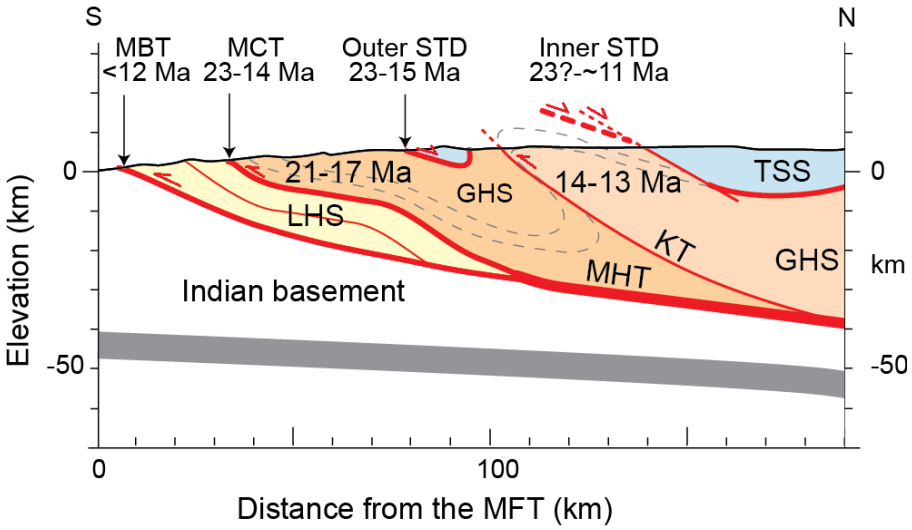

Figure 1.2 Structural cross section of the Himalayan-Tibet Orogen along ~90°E (Modified after Grujic et al. 2011). Ages point out the duration of ductile shearing along main structures. TSS—Tethyan sedimentary sequence; GHS—Greater Himalayan Sequence; LHS—Lesser Himalayan Sequence; STD—South Tibetan detachment; MHT—Main Himalayan thrust; MCT—Main Central thrust; MBT—Main Boundary thrust; KT—Kakhtang thrust.

India (Yin and Harrison, 2000; Yin, 2006). Moreover, within the Himalayan orogen, the ongoing shortening ranging from 17-20 mm/yr has resulted in great destructive earthquakes in the densely populated Himalayan region (Avouac, 2015; Bilham et al., 2001; Stevens and Avouac, 2016;

Mishra, 2014). Therefore, the younger thrust faults at the Himalayan front, MBT and MFT, are the major sources of earthquake threat. However, these onsets of movement along these structures have been only determined indirectly but imprecisely, and their activity cannot be determined by these indirect methods, like thermochronological analysis, magnetostratigraphy, and the method using the difference of cooling histories of faulting rocks to constrain the structural timing (Meigs et al., 1995; Van der Beek et al., 2006; Hirschmiller et al., 2014), because these are upper crustal brittle structures. Knowledge of the exact timing of the movement along these geologically young structures is important to determine because their age constrains the slip rates and therefore provides a crucial parameter in determining the stress accumulation (loading) rates along the currently seismically active faults in the area. This research traces the evolution of the MBT and MFT in the Bhutan Himalaya through the study of clay-rich gouges.

1.2 Why Clay Minerals are Important

Clay is the dominant mineral group in fault gouges, common products of near-surface faulting. It has two main origins: one is detrital, derived from other place like the wall rock while the other is authigenic, generated in the brittle fault zone during the movements of faults (Haines and Van der Pluijm, 2008). Authigenic component is critical to study the faulting time, especially K-bearing authigenic clay minerals like illite. It is because using K/Ar dating techniques, K-bearing authigenic clay minerals can provide us with a reliable age of faulting. Therefore, the presence of K-bearing authigenic clay minerals is the key to this research and the larger project.

Since the K-bearing clay minerals are crucial for fault dating, it is very important to investigate possible multiple generations of clay and to characterize clay morphology and composition. For example, the presence of clay minerals may control mechanical behavior of fault systems like weakening faults (Yan et al., 2001). Moreover, the composition of clay minerals in the gouges might be controlled by fluids, consequently, fluid evolution can be reflected by clay geochemistry (Choo and Chang, 2000). Therefore, the importance of clay minerals for brittle faulting is not only to record its evolution and reconstruct the faulting condition but to reflect the source of fluids and paleo-environment and especially to date fault gouges.

1.3 Thesis Objectives and Structure

The aims of this study are to understand the formation of fault gouges, the evolution of faulting, the importance of fluids, and the role of clay minerals during deformation, and to reconstruct the detailed history of faulting, as well as to further date faults for the larger project of dating paleoseismic events in the eastern Himalaya. To achieve these aims, I have characterized the mineralogy, morphology, composition, and geochemistry of clay minerals dominant in fault gouges within the frontal Himalaya. This was implemented by using ultrasonic-separation and analytical techniques mainly including X-ray diffraction and microscopy analysis, as well as Oxygen and Hydrogen stable isotope analysis. The specific research questions I tried to answer in this project are: 1) how fault gouges along these major faults (MBT and MFT) formed; 2) what is the role of clays during deformation; 3) why fluids are important for clay formation; 4) under what conditions fault gouges formed. Table 1.1 shows thesis objectives, used methods, and persons or organizations who have done corresponding parts.

Table 1.1 Thesis objectives with used methods and researchers

Objectives	Methods	Researchers
1. Collect samples in field	- Field Methods	Catherine & Djordje
2. Structurally characterize faults from data collected in field within the frontal Himalaya (MFT, MBT, minor faults in Siwaliks)	- Literature Review and Summary	Yuqiu
3. Prepare fault gouges samples for clay separation, chemical pretreatments, and sample mounting	- Particle-Size Separation - Sample Mounting - Chemical pretreatments	Yuqiu
4. Identify clay mineralogy	- XRD analysis	Yuqiu
5. Describe clay morphology and composition	- TEM and SEM/EDS	Catherine & Yuqiu
6. Characterize clay geochemistry	- O & H stable isotope analysis	Andreas Mulch, University Frankfurt (Germany) & Torsten Vennemann, University Lausanne (Switzerland)
7. Understand fluid composition and reconstruct the conditions of fault gouge formation	- Isotopic data analyses	Djordje & Yuqiu

This thesis includes six chapters as main body and is structured as a research paper with an abstract, acknowledgements, introduction, geological setting, methodology, results, discussion, conclusion, references, and appendices that consist of specific procedures and supplementary

data. The first chapter introduces the context, motivation, importance, and objectives of this research, the geological setting provides pertinent information about the study area whereas sufficient details of used methods are shown in the methodology. The descriptions of results include the mineralogy, morphology and composition, and geochemistry of clay, and the chapter of discussion is organized in a way to address scientific questions in this research. The conclusion summarizes all the findings and proposes further research.

Chapter 2: Geological Setting

2.1 Geology of the Eastern Himalayas

According to regional variations in geomorphology, the Himalaya can be divided into western (70°E-77°E), central (77°E-88°E), and eastern (88°E-98°E) sectors (Yin et al., 2009). There are four main lithotectonic units extending along the entire Himalayan orogen: the Tethyan Sedimentary Sequence (TSS), the Greater Himalayan Sequence (GHS), the Lesser Himalayan Sequence (LHS), and the Sub-Himalayan sediments (Le Fort, 1975; Hodges, 2000; Gehrels et al. 2003; Figure 2.1 & 2.2). In the higher Himalaya, the TSS were deposited from Neoproterozoic to Cretaceous and locally Eocene as sedimentary sequences along the northern passive margin of Gondwana and later, of the Indian plate. It is separated from the GHS by the South Tibetan Detachment (STD), a shallowly northward dipping normal ductile shear zone (Kellett and Grujic, 2012). The GHS are amphibolite to granulite metamorphic grade metamorphic rocks occupying the core of the orogen, and bounded by the Main Central Thrust (MCT) to the south side. The MCT is a few kilometers thick ductile shear zone with top-to the south shear sense which was active during Middle and Late Miocene (~23 Ma – 14 Ma) (Grujic et al. 2011; Mottram et al., 2014; Mottram et al., 2015; Searle et al., 2008). Below the GHS, greenschist to low-grade LHS mostly comprises Messo Proterozoic clastic sediments and granitoids, and Neo Proterozoic to mid Permian clastic sediments. The LHS is deformed in a series of thrust duplexes (Long et al., 2011) and is separated from the Sub-Himalaya sediments by the Main Boundary Thrust (MBT). The MBT is brittle top-to the south thrust. So far, using the indirect method of contrasting the cooling histories of faulting blocks, onset of its movement has been estimated, in the northwest Himalaya to approximately 10 Ma (Meigs et al., 1995). In the eastern Bhutan, the timing of the MBT has been estimated by sequential restoration of balanced cross sections (McQuarrie et al., 2014). All the ductile and brittle thrusts merge at depth of approximately 10 – 12 km into the basal detachment of the Himalaya, the Main Himalayan Thrust, MHT (Nelson et al., 1996; Figure 2.2).

The eastern Himalaya including the Sikkim, Bhutan, and Arunachal Pradesh regions shows distinct geological features. This segment of the orogen displays a basement-involved uplift in its foreland with the length of 400 km, called the Shillong Plateau, and locally lack the foreland basin (Biswas et al., 2007). Moreover, the eastern Himalaya may have developed major

contraction structures at 5-10 Ma, later than that in the central Himalaya (Yin et al., 2009). In addition, there are two major features different from the rest of the Himalayas in the area of Bhutan: one is extensive klippen of the STD, overlying the GHS; the other is an out-of-sequence thrust, the Kakhtang thrust (KT), which structurally lies above the klippen and results in the exposure of double thickness of the GHS (Grujic et al., 2002; Grujic et al., 2011; Figure 2.1). Since the Bhutan Himalaya has similar structure to the Sikkim, the following section includes several citations about the Sikkim Himalaya.

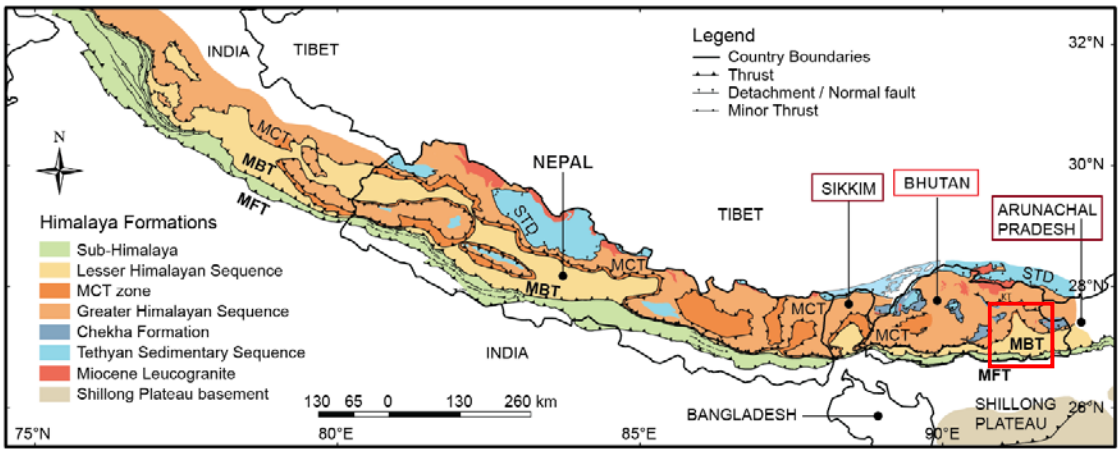

Figure 2.1 Geological map of the Himalayan Orogen (Based on Hirschmiller et al. 2014). The red rectangles show the main regions of the eastern Himalaya. The red rectangle with thick border points out the location of the study area. STD—South Tibetan detachment; KT—Kakhtang thrust MCT—Main Central thrust; MBT—Main Boundary thrust; MFT—Main Frontal thrust.

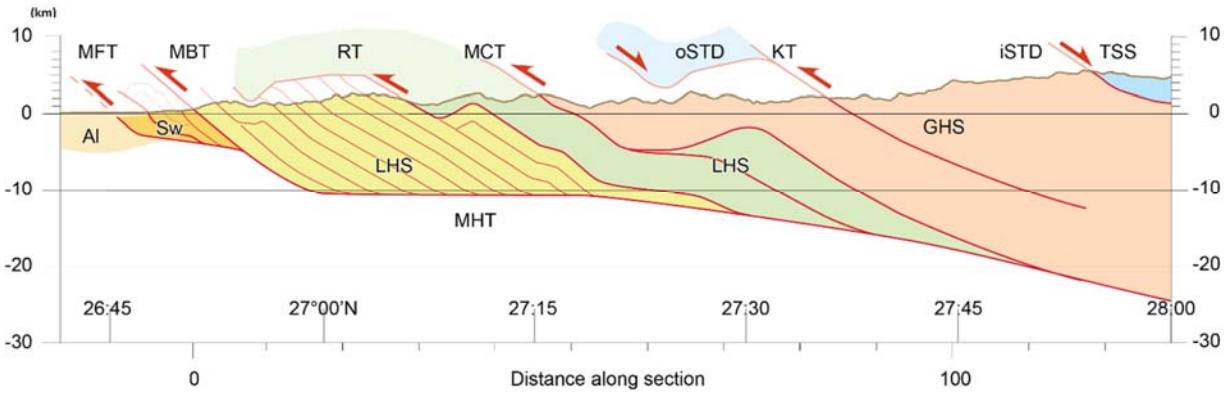

Figure 2.2 Structural cross section of the eastern Bhutan along ~ 91.5˚E (From Long et al. 2011). TSS—Tethyan sedimentary sequence, GHS—Greater Himalayan Sequence, LHS—Lesser Himalayan Sequence, Sw – Siwalik, Al- Alluvium, oSTD & iSTD—outer & inner South Tibetan detachment, KT—Kakhtang thrust, MHT—Main Himalayan thrust, MCT—Main Central thrust, RT – Ramgarh Thrust, MBT – Main Boundary Thrust, MFT – Main Frontal Thrust.

2.2 Geology of the Bhutan Himalaya

2.2.1 Lesser Himalayan Sequence

The LHS has two subgroups: Lower and Upper Lesser Himalaya. The upper Shumar-Daling Group is the main member in the Lower LHS while the Baxa Group, Diuri Formation, and Gondwana Sequence are the units of the Upper LHS (Figure 2.3 & 2.4). The Proterozoic Daling-Shumar Group and associated granitoids can be divided into two independent subgroups, the quartzite-rich Shumar Formation and the overlying phyllite-dominant Daling Formation, both of which have good outcrops in the Kuru Chu Valley (McQuarrie et al., 2008; Long et al., 2011). The Proterozoic-Cambrian Baxa Group involves a combination, from quartzite to siltstone, from slate to dolomite and limestone, all in diverse colors and in distinct sizes and structures. Baxa group is divided into four formations: the Manas, Jaiti, Phuentsholing and Pangsari Formations (Gansser, 1983; McQuarrie et al., 2008; McQuarrie et al., 2013). The Carboniferous-Permian Diuri Formation is described as diamictite with ~ 2 – 2.5 km thickness, mainly contains slates, shale, and sandstone in distinct sizes and roundness, and include clast types like quartzite and dolomite (McQuarrie et al., 2008; Long et al., 2011). The Gondwana Sequence bounded by faults in both sides involves dominantly continental sediments with differently sandstone, quartzite, shale, and slate with coal deposits (McQuarrie et al., 2008; Grujic et al., 2017).

The prominent and composite structure, called the Lesser Himalayan duplex (LHD) has been developed during the shortening and stacking of the LHS rocks (Landry et al., 2016). The LHD consists of two overlapping duplexes, the Daling and Rangit duplex (Landry et al., 2016; McQuarrie et al., 2008). Bounded by the MBT at the bottom, the Daling duplex has been developed during the formation of its roof thrust, the MCT zone (Anczkiewicz et al., 2014; Mottram et al., 2014; Landry et al., 2016). The Rangit duplex united the Daling Formation, Baxa Group, and Gondwana Sequence and structurally underlay the Daling duplex with two boundaries: the floor thrust of the MBT and the roof thrust of the Ramgarh Thrust, RT (Bhattacharyya and Mitra, 2009; Mitra et al., 2010; Mukul, 2010; Landry et al., 2016). The Rangit duplex shows its structure with three parts: the southern part has a foreland-dipping structure as the frontal horses, the middle part is an antiformal stack, and the northern part is called as the rear hinterland-dipping horses (Bhattacharyya and Mitra, 2009; Mitra et al., 2010; Landry et al., 2016).

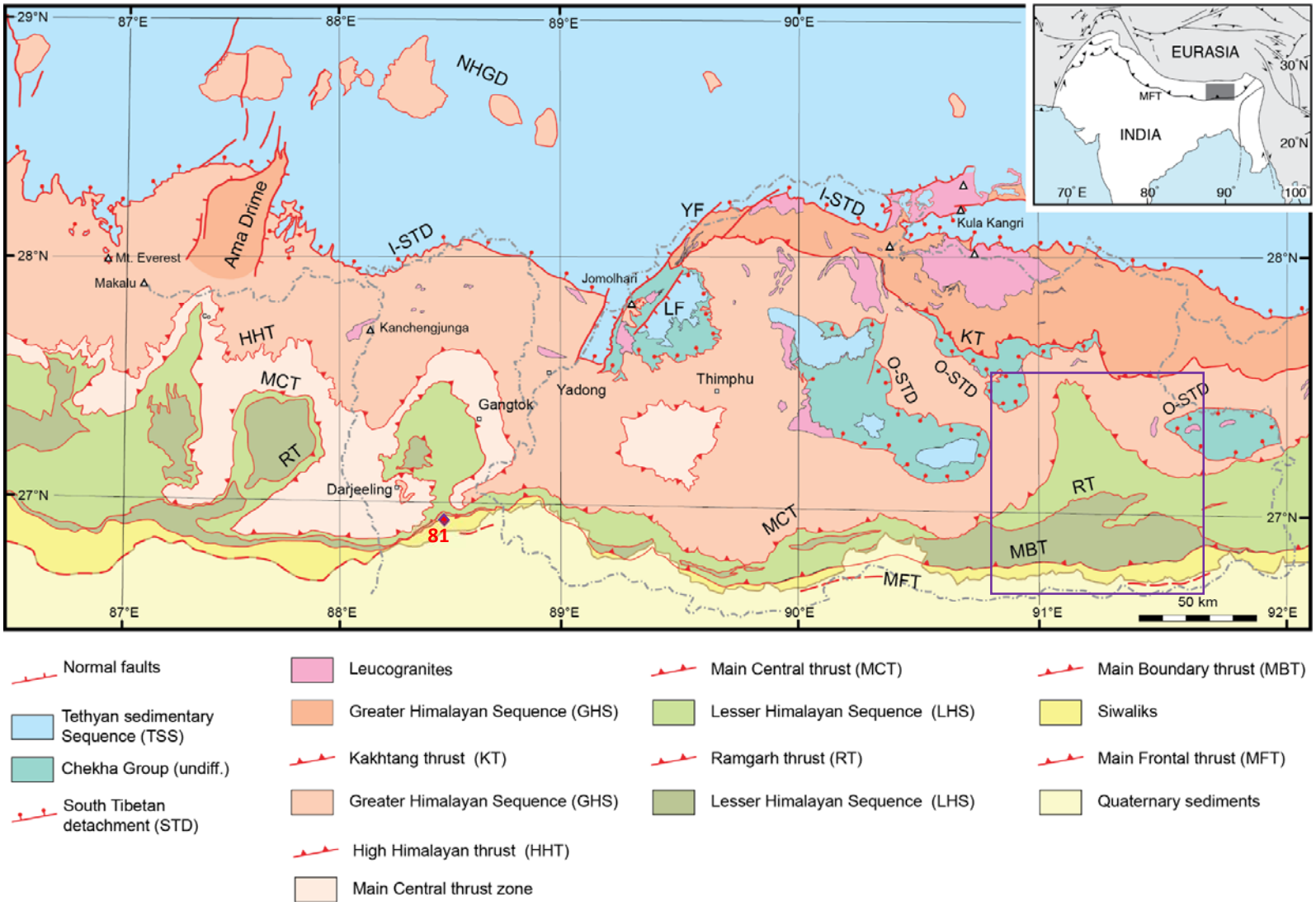

Figure 2.3 Geological map of the eastern Himalaya (Based on Grujic et al., 2011). The purple rectangle refers to the location of the study area. Only one Siwalik sample from Sikkim is labelled as red diamond with sample number. O-STD, I-STD—outer and inner South Tibetan detachment system, respectively; HHT—High Himalayan thrust; MBT—Main Boundary thrust; MCT—Main Central thrust; MFT—Main Frontal thrust; KT—Kakhtang thrust; RT—Ramgarh thrust; LF—Lingshi fault; YF—Yadong fault, NHGD—North Himalayan gneiss domes. Inset shows location of Figure 2.3.

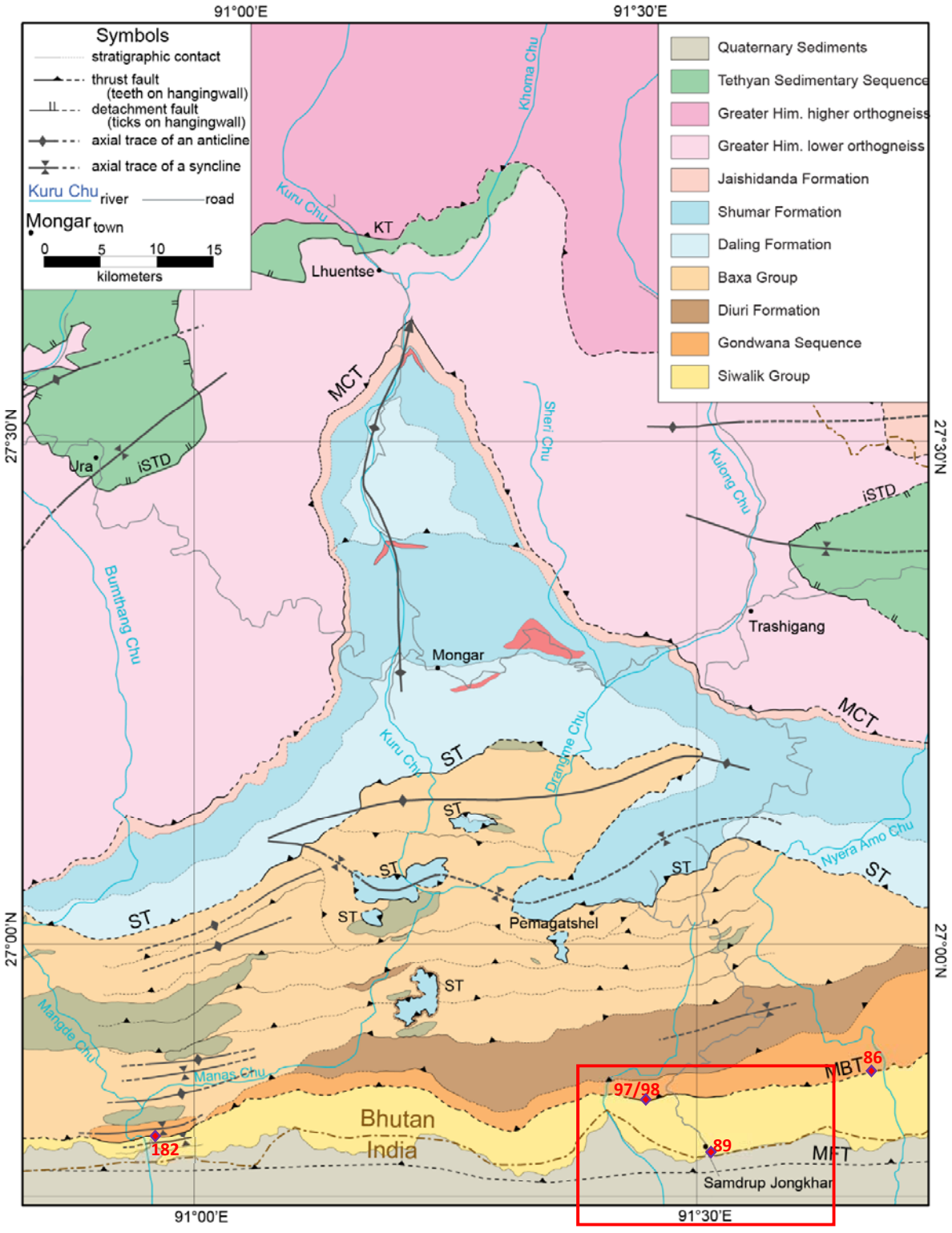

Figure 2.4 Geological map of the eastern Bhutan (Based on Long et al., 2011). All samples from the eastern Bhutan are labelled as red diamonds with sample numbers. The red rectangle labels the geological map of the Siwalik Group as seen in figure 2.5. I-STD—inner South Tibetan detachment system; MBT—Main Boundary thrust; MCT—Main Central thrust; MFT—Main Frontal thrust; KT—Kakhtang thrust; ST—Shumar thrust.

2.2.2 Siwalik Group

The Miocene-Pliocene Siwalik Group in Bhutan contains conglomerate, sandstone, and siltstone without metamorphism (Coutand et al., 2016). It can be informally divided into three groups, from oldest to youngest: lower, middle, and upper (Coutand et al., 2016; Figure 2.5). From lower to upper, the grain size increases, from medium to clast, and each group involved siltstone and sandstone, but mudstones only show in the lower group while conglomerates only display in the upper (Coutand et al., 2016). Moreover, the Siwalik Group shows northward dipping with the range of 25˚ to 84˚, and most of dip angles are within 25˚ – 45˚ (Coutand et al., 2016; Figure 2.5). Also, this group is underlying the MBT as a foot wall but overlying the MFT as a hanging wall. It is confirmed as the non-repeating section with a continuous thickness of 6 km, but the movement of MFT resulted in its uplifting (McQuarrie et al., 2008).

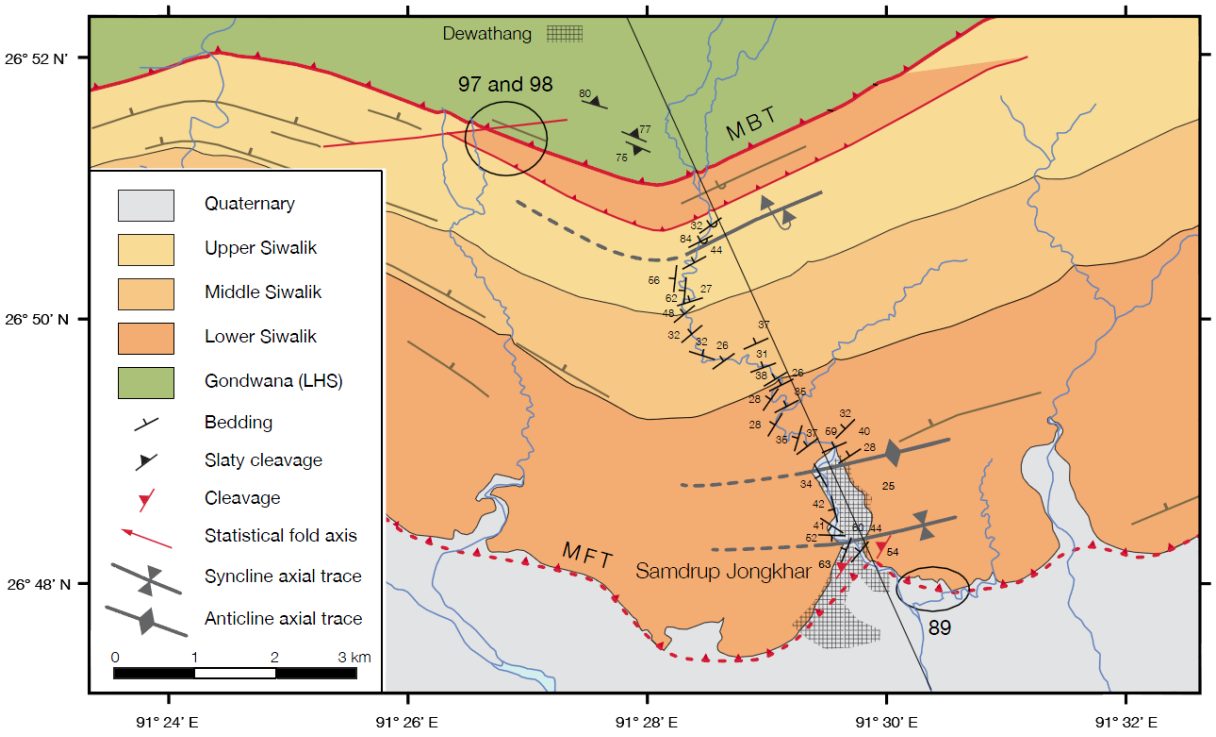

Figure 2.5 Geological map of the Siwalik Group showing subunits and geological structures, around the Dungsam Chu (Based on Coutand et al., 2016). The black circles label sample locations with sample names. MBT – Main Boundary Thrust, MFT – Main Frontal Thrust.

2.2.3 Main Boundary Thrust and Main Frontal Thrust

The MBT in Bhutan is the lower boundary of the LHS and overlies on the Siwalik Group. Its motion not only separated the Upper LHS but truncated the Siwalik Group. The MBT got folded and shortened in the eastern Himalaya within 10 Ma (McQuarrie et al., 2014; McQuarrie et al., 2008). However, the onset age of the MBT is less well-constrained, because there are no data to record the amount of slip along the structure (Hodges, 2000; McQuarrie et al., 2014).

The MFT is the youngest active structure and was formed approximately 2 Ma in the eastern Himalaya (Hodges 2000; Jouanne et al., 2004). The MFT which at the surface dips at 20-40 degrees (Figure 2.6). At the depth of 10-11 km, it merges with the subhorizontal MHT (Coutand et al., 2014). The motion of MFT contributed to the tilting of Late Miocene to Pleistocene foreland basin deposits (Hirschmiller et al., 2014, Coutand et al., 2016). The folding and shortening process of siwalik sediments started at approximately 1 – 2 Ma (Coutand et al., 2016).

2.2.4 Geological Observations

The fault gouge samples of the MBT and MFT were collected at six locations. At each location sample was taken from the fault gouge, (the fault core) and from the immediate hanging wall rocks and footwall rocks (Figure 2.3 – 2.5). All samples are briefly described in Table 2.1. Figure 2.7 shows the view of the MBT exposure in Deothang coal mine where up to five strands of the fault have been mapped by Catherine Mottram and Djordje Grujic. From figure 2.7, the MBT shows northward dipping with the Quaternary Siwalik sediments in the footwall and Permian coal-bearing Gondwana sediments in the hanging wall. All the details of figure 2.7 are shown in figure 2.8 a) – d). The fault gouge of the northward dipping MFT is displayed in figure 2.6, with the Pliocene Siwalik siltstone and mudstone in the hanging wall and the Holocene river terraces in the footwall.

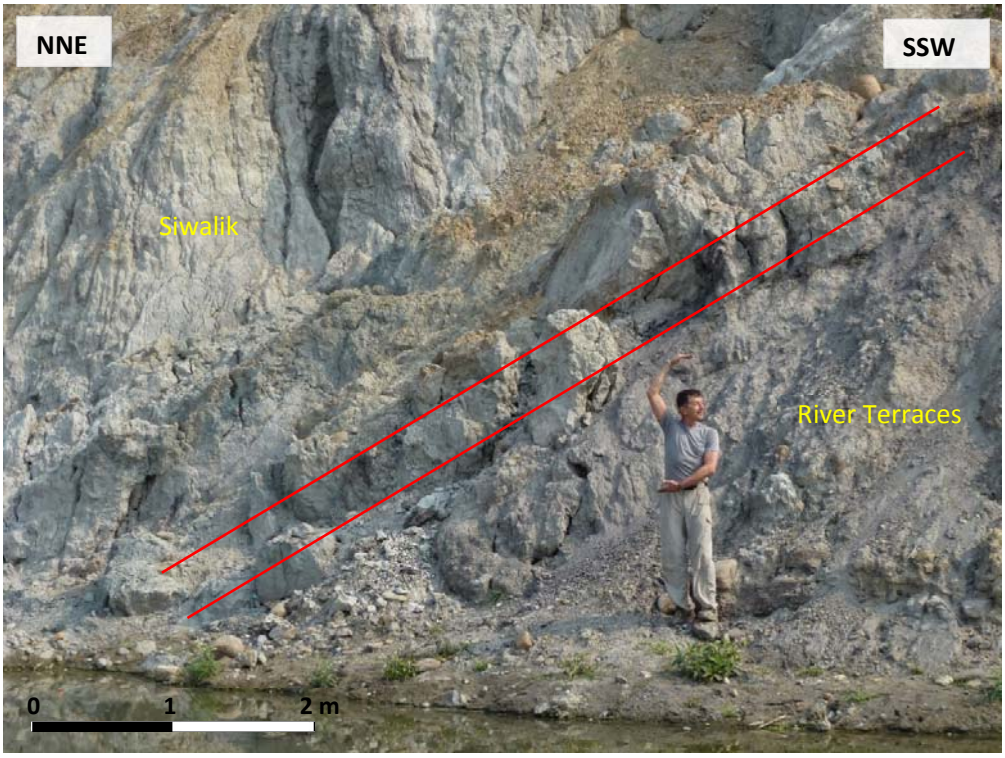

Figure 2.6 Main Frontal Thrust. Photo by Catherine Mottram.
The red lines label the fault gouge in the MFT.

Figure 2.7 Larger view of MBT exposure in Deothang coal mine. Photo by Catherine Mottram. The red outline shows the southernmost branch of the MBT. The red arrow indicates that the hanging wall moved upward.

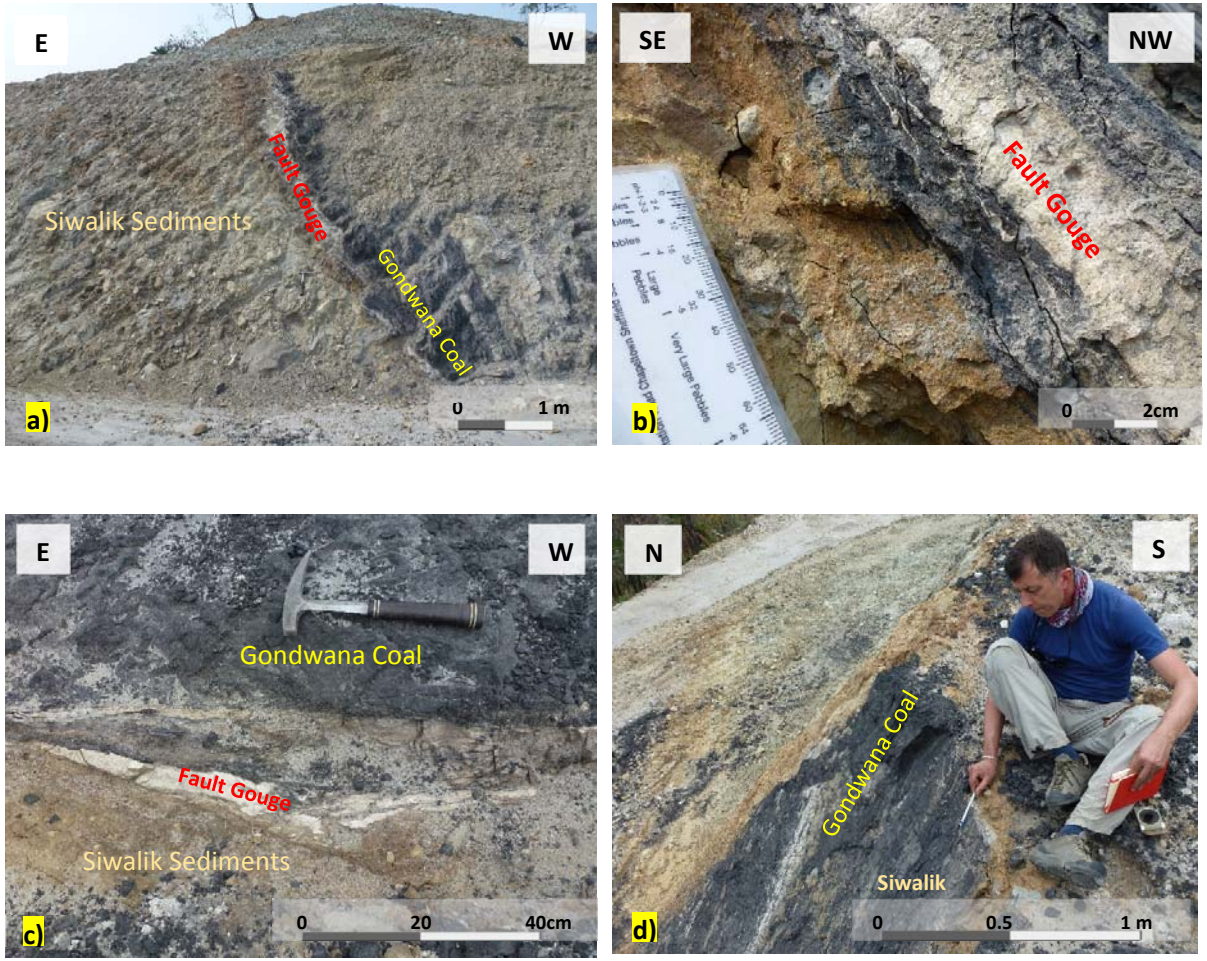

Figure 2.8 a) Main Boundary Thrust from Deothang coal mine with coal-bearing Gondwana sediments thrust over Siwalik sediments; b) Close-up of fault gouge along MBT; c) Plan view of MBT; d) The slip direction of the MBT as indicated by pencil. Photos by Catherine Mottram.

Table 2.1 Catalog of Hand Samples. In sample name, SK – Sikkim; BH – Bhutan; the first letter after number is the sample from the foot wall while the second is from the hanging wall. The subscript number in the second letter is the number of samples.

Sample	Unit/Structure	type	Number	Latitude	Longitude	Altitude	Location	Description
BH16-86B, C	Diuri	fault gouge	2	N26.87905	E91.66777	573 m	Bangtar	Graywacke/Diamictite, Gondwana-Diuri contact
BH16-97D	MBT	fault gouge	3	N26.84909	E91.44968	604 m	Deothang coal mine	Graywacke, Gondwana-Siwaliks contact
BH16-98D, C_2	MBT	fault gouge	3	N26.84879	E91.45037	623 m	Deothang coal mine	Graywacke, Gondwana-Siwaliks contact
BH16-182A, C	Siwalik	fault gouge	2	N26.8089	E90.95769	190 m	Dogar - Panbang	Sandstone, Siwalik sandstones
BH16-89D, A	MFT	fault gouge	3	N26.79199	E91.5108	144 m	Daranga Mella, S.Jongkhar	Alluvial Sandstone, MFT

Chapter 3: Methodology

Fault gouge samples were collected by Catherine Mottram and Djordje Grujic from the Himalayan frontal faults, the MBT and the MFT, in the eastern Bhutan in February 2016 (Figure 2.3-2.5). Since only the clay minerals formed during the fault movement can provide a reliable age for faulting, separating comminuted rock-forming minerals and those formed by surface weathering with large grain sizes from clay-size minerals should be done using clay separation techniques (Choo and Chang, 2000). X-ray diffraction (XRD) analysis was primarily used to identify clay and associated minerals, combined with petrographic thin section microscopy, scanning electron microscopy and energy dispersive spectroscopy (SEM/ EDS), and transmission electron microscopy (TEM). Finally, to further characterise clay forming environment, H and O stable isotopes analysis was applied.

3.1 Clay Mineral Separation

Using SELFRAG device at the Federal Insitute of Technology (ETH) in Zurich Switzerland, fault gouge samples were fragmented without grinding or pulverizing, which could reduce non-clay minerals to clay sizes. Overnight soaking followed by blending have been also done to suspend clay minerals (Appendix B.1). To determine whether the samples include carbonates and organic materials, small amount for each sample was treated by acetic acid and sodium hypochlorite bleach (NaOCl) (Appendix B.2). In the test of carbonates, acetic acid less than 0.3 molar was used because this amount has no effect on clay minerals extracted (Moore and Reynolds, 1997). If the test revealed a presence of carbonate because of the effervescence, the entire sample was treated to remove the carbonates. In addition, organic matter must be removed due to its effect on XRD peaks (Moore and Reynolds, 1997). Diluting bleach (NaOCl) to pH 9.5 by HCl, heating the mixture of the sample and the bleach in a boiling-water bath for about 15 minutes, and centrifuging for 3 minutes, the procedure was repeated until organic materials is sufficiently removed, which was shown by the color change of the sample to white, gray, or red. Centrifugation with deionized water at least five times was used to rinse out the sample.

Prepared clay samples were separated into clay-size fractions of 2μm, 0.4μm, and 0.1μm by ultrasonic disaggregation, gravity settling, and centrifugation (Appendix B.3). The gravity

settling time was calculated, based on Stokes's law (Equation 3.1) and the relation of velocity = distance/time ($V=h/t$) (Moore and Reynolds, 1997).

$$V_T = \frac{g(d_p - d_l)D^2}{18\eta} \quad (3.1)$$

Where V_T is a terminal settling velocity of the solid particle (in m/s), g is gravitational acceleration (9.807 in m/s^2), d_p is the density of settling particle (2650 in kg/m^3), d_l is the density of water (1000 in kg/m^3), D is the diameter of particle (in m), and η is dynamic viscosity of water (0.001005 in Pa·s), based on T = 20 ˚C, average lab temperature. Thus,

$$t = \frac{18\eta h}{g(d_p - d_l)D^2} \quad (3.2)$$

Where h is the distance that a particle falls (in m), and t is settling time for gravity sedimentation of particles in water (in sec).

The settling time for a specific centrifuge for sedimentation of particles was calculated by equation 3.3 (Moore and Reynolds, 1997).

$$T = \frac{\eta \, log_{10}(\frac{R_2}{R_1})}{3.81 r^2 N^2 (\rho - \rho_0)} + \frac{2(t_a + t_d)}{3} \quad (3.3)$$

Where T is total time (in sec), t_a is the time of acceleration (in sec), t_d is the time of deceleration (in sec), η is viscosity (in poises), R_1 is initial distance from rotation axis (in cm), R_2 is final distance from rotation axis (in cm), r is particle radius (in cm), N is angular velocity (in rev/s), ρ is the density of the particle (in g/cm3), and ρ_0 is the density of water (in g/cm3).

After the centrifugation, all clay-size fractions of the samples were placed in an oven at a temperature below 60 ˚C to dry. The dried sample fractions were weighted by a high precision balance for further quantitative analysis (Appendix B.4).

3.2 Analytical Methods

3.2.1 X-Ray Diffraction

XRD is a rapid mineral identification technique relying on the dual wave of X-ray to discover information about crystalline structure (Nesse, 2000). It is the primary method to identify clay and relative minerals due to very fine grain size and multiple generations and

transformation of clays with similar principal characteristics (Moore and Reynolds, 1997). XRD can be used for phase identification of a crystalline material because the wavelength of X-rays is similar to the spacing *d* of planes in a crystal lattice. X-rays have uniform diffractions and pass through materials at specific angles, and constructive interference will be produced (Figure 3.1). Therefore, any crystalline solid can be identified through its intensity peak at unique special angle. This procedure satisfies Bragg's Law (Equation 3.4), which demonstrates the relationship among the angle (θ), the interplanar spacing of atoms (d), and the wavelength of X-rays (λ).

$$n\lambda = 2d\,sin\,\theta \qquad (3.4)$$

Where n is an integer number of λ when constructive interference occurs (Nesse, 2000).

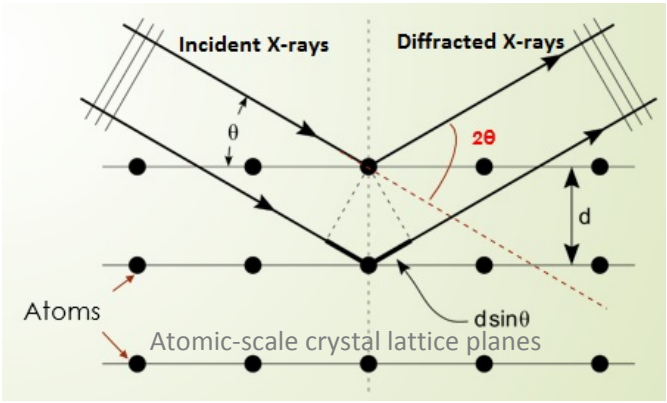

Figure 3.1 Diffraction diagram illustrating Bragg's Law. Complying with nλ = 2d sin θ, the incident X-rays diffract through the atom layer at a special angle of θ, and constructive interference of the diffracted rays will generate a peak in intensity. Modified on the diagram from Concept Web Alliance (CWA, 2010).

Two types of samples for XRD were prepared: one is oriented clay mineral aggregates using glass slide mount method, the other is random orientation of the grains with the smear mount method (Appendix C.1.1). For all non-separated fine samples and three separate fractions (2μm, 0.4μm, and 0.1μm), oriented sample mounting slides (2.7 by 4.6 cm) dried at room temperature, were made with approximate 4 ml of mixture containing approximately 200 mg of sample and deionized water. Non-oriented samples were prepared by mixing non-separated sample powder with one or two drops of deionized water onto a slide using microspatula. The purpose was to compare the basal reflections of XRD for each method to select a good diffraction pattern to do analysis. Table 3.1 lists all the XRD preparations with operating 2θ range.

Table 3.1 Sample preparations for X-ray diffraction with operating range of 2θ. Non-separated fine samples are labelled as "✓" while three separate fractions (2μm, 0.4μm, and 0.1μm) are marked by "✓". For glycolated and heating treatments, only 86AI used 2μm fraction labelled as "$✓_{2μm}$".

Samples	Unit	Smear Mount	Glass Slides		Heating	2θ Range
			Air-Dried	Glycolated		
86AI	Diuri	✓	✓✓	$✓_{2μm}$	$✓_{2μm}$	2-35°
86AII	Diuri	×	✓✓	✓	✓	2-35°
97AII	MBT	✓	✓✓	✓	✓	2-35°
97B	MBT	×	✓✓	✓	✓	2-35°
98A	MBT	✓	✓✓	✓	✓	2-35°
98B	MBT	✓	✓✓	✓	✓	2-30°; 2-35°
182BI	Siwalik	×	✓✓	✓	✓	2-30°; 2-90°
182BII	Siwalik	✓	✓✓	✓	✓	2-30°; 2-35°
89BI	MFT	✓	✓✓	✓	✓	2-35°
89BII	MFT	×	✓✓	✓	✓	2-35°; 2-90°
89C	MFT	×	✓✓	✓	✓	2-35°

The Siemens D500 X-Ray Diffractometer at the Department of Chemistry, Dalhousie University, was operated with an accelerating voltage of 35 kV and current of 30 mA, with 0.3° and 0.15° opening slits, using a Cu anode x-ray tube and a graphite monochrometer (Appendix C.1.2). The working principle of X-ray diffractometer is that as the sample and detector rotate at twice the incident angle, the detector reports the intensities of X-ray photons (Figure 3.2). The positions and shapes of peaks in X-ray diffractogram are diagnosed to identify different minerals. Since the main minerals in these samples are clay, most samples were examined in the 2θ range of 2-35° with scanning step of 0.05° and dwell time of 1.5 s, but after preliminary XRD analysis, the samples 182BI and 89BII were selected as representatives of respective mineralogical group to run the 2-90° 2θ range to further analyze present non-clay minerals (Table 3.1).

By comparing the first XRD results of 18 slides of the select samples, it was found that the slides for each sample showed same spectra, that peaks have similar intensities except for the sample 86AI, and that the coarse minerals like quartz and feldspar might be contained in these samples. Therefore, considering both the better diffraction pattern and probable presence of some coarse minerals, 86AI used 2μm fraction to do the following XRD analysis while other samples applied non-separated ones (Table 3.1).

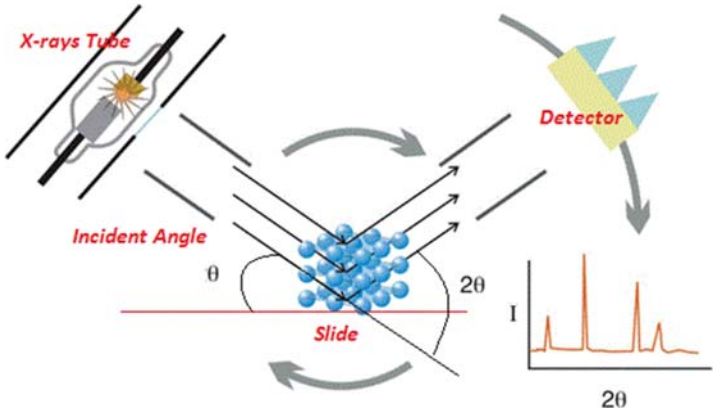

Figure 3.2 The illustration diagram about how to determine crystalline structure by XRD. Modified on the diagram from Rensselaer Polytechnic Institute (RPI).

The XRD data analysis was done by software "X'Pert HighScore". To identify clay minerals with similar basal spacing, such as illite, smectite, and interstratified illite-smectite, air-dried and ethylene glycol-solvated samples were prepared for XRD (Appendix C.1.3). The presence of smectite can be identified by the shift of diffraction pattern in the 001 reflection from around 6° to about 5.2° 2θ after glycol solvation (Moore and Reynolds, 1997; Figure 3.3). The changes of intensities before and after glycol treatment can be used to identify illite-smectite from pure smectite: the intensity of pure smectite gets stronger whereas interstratified illite-smectite becomes weaker (Moore and Reynolds, 1997; Figure 3.4).

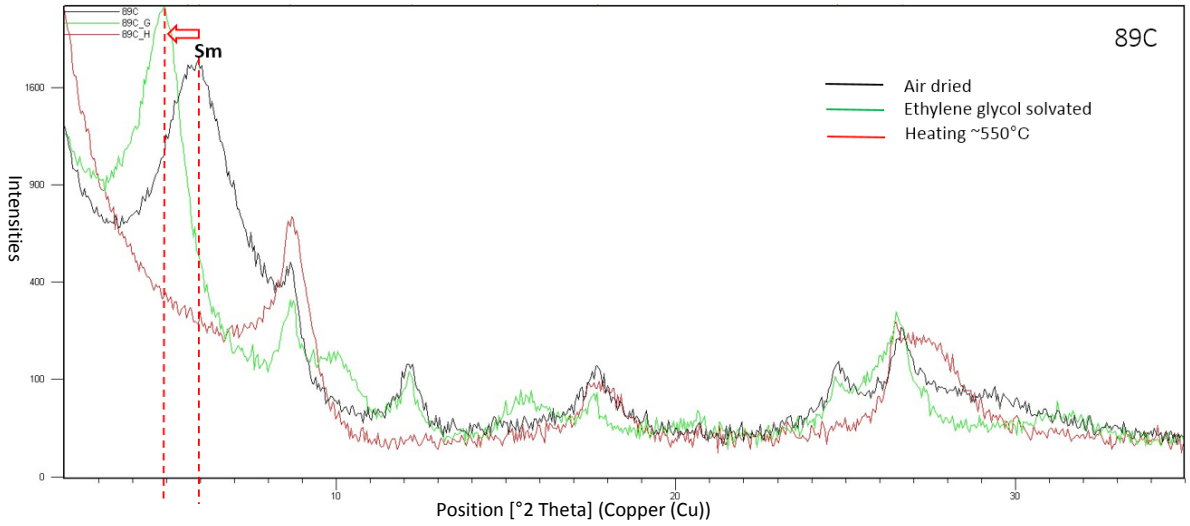

Figure 3.3 The presence of smectite (Sm) in sample 89C evidenced by the shift of diffraction pattern from ~6° to ~5° 2θ with broad shape in the 001 reflection after glycol treatment. The red dash lines label 2θ positions in both air-dried and glycol solvated conditions. The red arrow shows the shift direction.

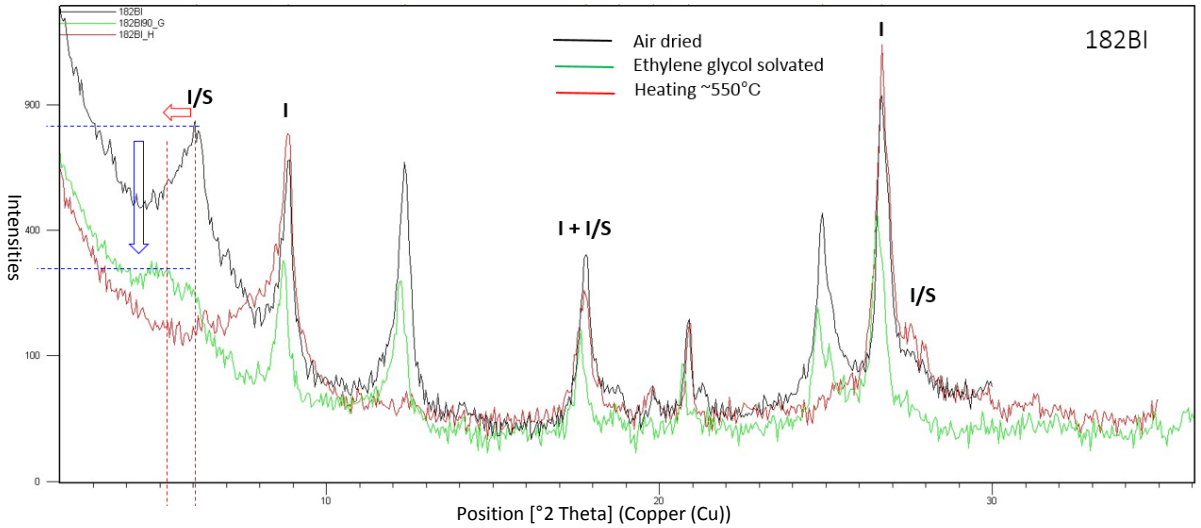

Figure 3.4 The presence of illite-smectite (I/S) in sample 182BI mainly evidenced by both the shift of diffraction pattern from ~6° to ~5.2° 2θ, the drop of intensity, and a high low-angle shoulder in the 001 reflection after glycol treatment. The red dash lines label 2θ positions in both air-dried and glycol solvated conditions while the blue dash lines point out the change of the intensities with the blue arrow. The red arrow shows the shift direction.

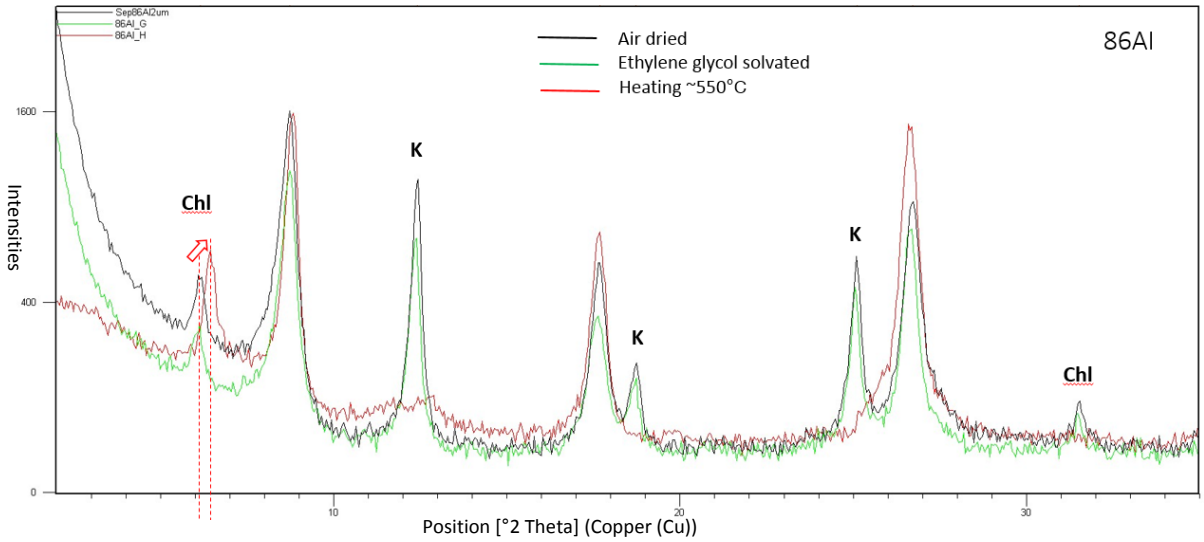

Figure 3.5 The presence of chlorite (Chl) and kaolinite (K) in sample 86AI. For chlorite, the main evidence is the shift of diffraction pattern from ~6° to 6.4° 2θ and intensity increase in the 001 refection. The red dash lines label 2θ positions in both air-dried and heating conditions. The red arrow shows the change direction. Kaolinite is evidenced by the disappearance of diffraction pattern after ~550°C heating.

Owing to similar patterns of peak intensities of some minerals, like kaolinite and chlorite groups, heating treatment about 550°C for an hour was done before the XRD analysis (Appendix C.1.3). Chlorite group will shift the 001 reflection to about 6.3 to 6.4° 2θ with the increase of intensity after heating to 550°C whereas the diffraction pattern of kaolinite group will disappear

(Moore and Reynolds, 1997; Figure 3.5). Thus, the changes of intensities before and after treatments were also diagnostic to differentiate similar minerals besides the change of peak position. The annotated XRD diagrams for clay mineral phases will be shown in the next chapter.

3.2.2 Scanning Electron Microscopy and Energy Dispersive X-Ray Spectroscopy

SEM is a technique for grain shape and microstructure analyses, and their distribution by micrography while EDS is an analytical technique used for qualitative elemental and chemically compositional analyses. SEM/EDS system is applied to characterize morphologies and compositions of clay minerals in this project.

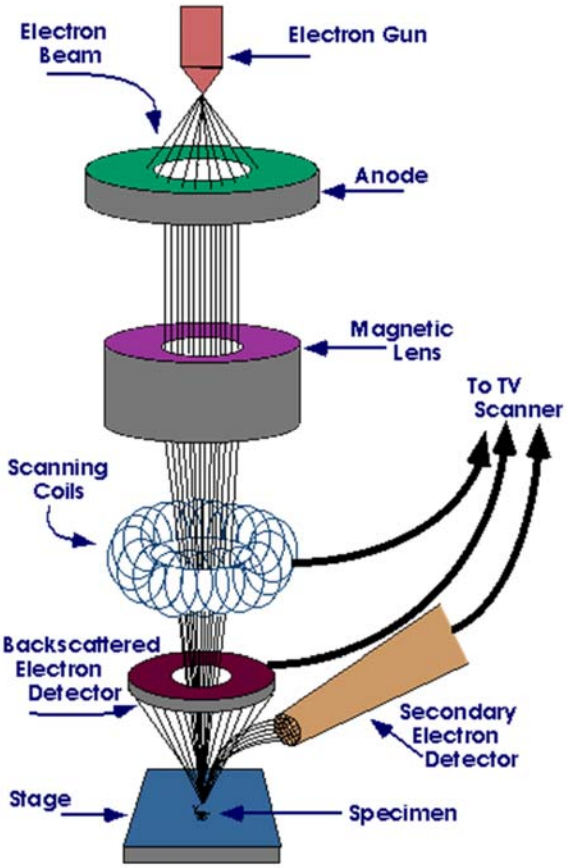

Figure 3.6 Schematic SEM system. From Purdue University, 2014.

The SEM uses a scanning beam of electrons instead of light to form an image. The incident electron beam is produced at the top of the microscope by heating a metallic filament. After it passes through the column of the microscope and electromagnetic lenses, it hits the sample. The energy exchange between the electron beam and the sample results in the reflection of high-energy electrons by elastic scattering, emission of secondary electrons by inelastic scattering and the emission of electromagnetic radiation, each of which can be detected by specialized detectors (Welton, 2004; Figure 3.6). The secondary or backscattered electrons are used for the SEM micrograph while the characteristic X-rays are for the EDS analysis. Unique energy level of X-rays produced by each element will yield a peak in the EDS spectrum diagram (Welton, 2004).

Clay samples were mounted on aluminium specimen mounts with ½ inch head, followed by overnight dry. The sample was coated with thin carbon layer using LEICA EM CED 030 carbon

coater before the SEM/EDS analysis, to make the sample conductive and avoid its charging (Appendix C.2). Using the SEM/EDS system of TESCAN MIRA3 in the Department of Geology at Saint Mary's University, the SEM was operated with the accelerating voltage of 20 kV. The micrographs were collected in secondary electron mode. Identification of each peak on the EDS spectrum was done with MIRA3 software. After the identification of all peaks, mineral identification was done by comparing the relative concentrations of the elements with the crystal morphology and the chemical formula of the suspected mineral (Welton, 2004).

3.2.3 Transmission Electron Microscopy

TEM is applied to further characterize morphologies of clay minerals with high magnification and high resolution. It forms detailed images with spacial resolution of 0.2 nm by passing a beam of electrons through a very thin slice (about 100 nm) of the object. The TEM produces a beam of electrons by using a tungsten filament. The electrons are accelerated through an electromagnetic field and get focused. As the beam passes through the sample, the electrons hit a phosphor screen and produce an image (Gard, 1971; Figure 3.7; Appendix C.3).

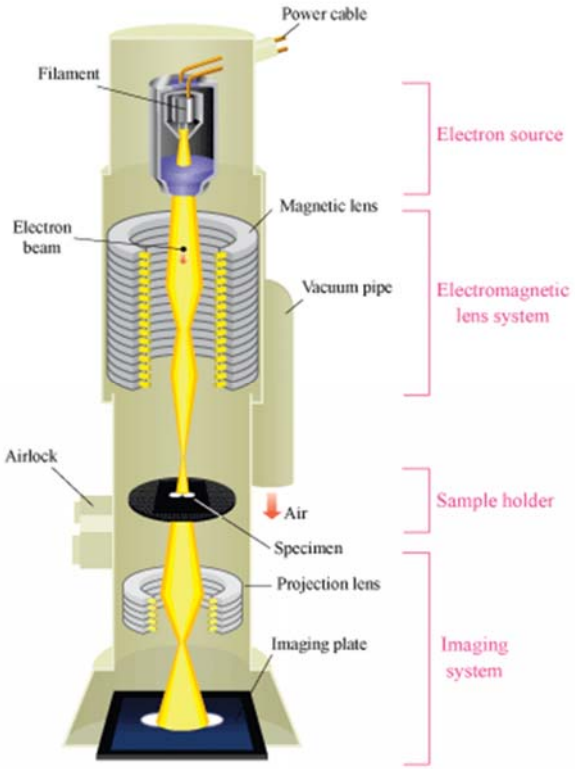

Figure 3.7 Schematic TEM system. From Atomic World.

Clay samples were diluted in 1:1 ratio at least twice to make less concentration and avoid grains clustering together. Mounting thin film on electrodeposited copper specimen grids of 3.05mm diameter was done with 1 or 2 drops of dilution for each clay separate before TEM analysis, to ensure electrons transmitting through samples (Appendix C.3). TEM observations were made with the Philips Tecnai-12 TEM system at 80 kV at the Department of Biology, Dalhousie University. The TEM was operated in the "bright field" imaging mode. Images were captured with up to 135k magnification using the software "Digital Micrograph".

3.2.4 H and O Stable Isotopes

The general characteristic of isotopes having the same atomic number but different atomic masses determines isotope fractionation processes in nature. The process involves the partitioning of isotopes between different substances or between two phases of the same substance with different isotope ratios. So, stable isotopes are applied for various areas like hydrosphere, atmosphere, biosphere, and lithosphere to study paleo-environmental conditions (Hoefs, 2015). The applications of stable isotopes to clay minerals are depending on isotope partitioning factors between clay minerals and water, the temperature, and the time in that isotopic exchange within clays ceased (Hoefs, 2015). The formation of clay minerals is always related to waters, therefore O and H isotope compositions in clay minerals reflect the changes in temperature and in water composition (Bauer and Vennemann, 2014; Hoefs, 2015). For clay minerals formed in contact with meteoric waters, the isotopic compositions should plot on lines sub-parallel to the Meteoric Water Line, and the offset is determined by respective fractionation factor (Hoefs, 2015; Figure 3.8). To determine clay minerals with hypogene and supergene origins, the supergene-hypogene line is used as a reference (Sheppard et al., 1996). Hypogene refers to the process of hydrothermal alteration while supergene is the process of residual deposits caused by weathering of parent rocks (Dill et al., 2008).

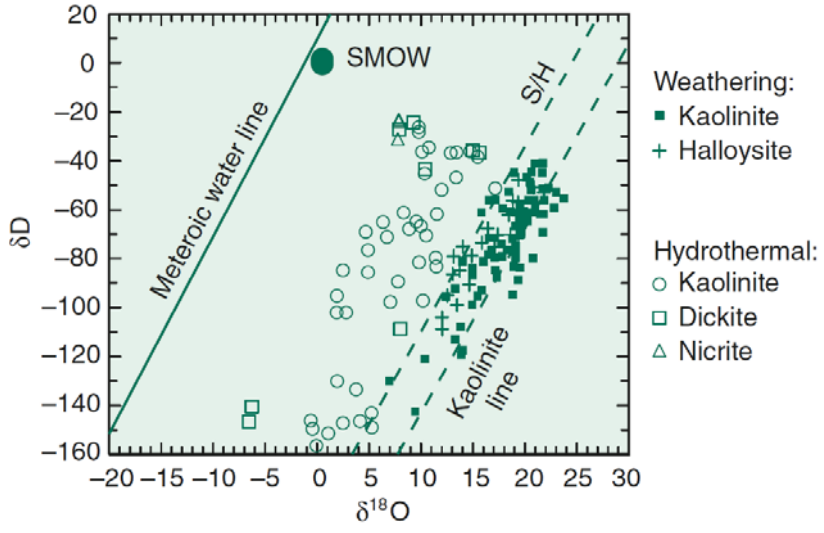

Figure 3.8 Meteoric Water Line shown with the reference of kaolinite weathering and supergene/hypogene (S/H) lines. (From Hoefs, 2015.) δ D and $\delta^{18}O$ values of kaolinites and related minerals from weathering and hydrothermal environments.

The precision with the determination of relative difference in isotope abundances between two samples is substantially richer than the accuracy for the measurement of absolute isotope abundance. As a standard, delta notation (δ) is used for isotope ratio measurements and expressed as:

$$\delta in‰ = \frac{R_{(sample)} - R_{(standard)}}{R_{(standard)}} \times 1000 \qquad (3.5)$$

where δ is given in per mil (‰) and R represents the measured isotope ratio (Hoefs, 2015). All isotopic values are reported in ‰ relative to Vienna Standard Mean Ocean Water (VSMOW).

3.2.4.1 Oxygen mass spectrometry

Oxygen isotopic composition of fractional clay samples was measured by using a Finnigan MAT 253 isotope ratio mass spectrometer in the Stable Isotope Laboratory at the University of Lausanne, Switzerland. The weights of all air-dried fractions (2μm, 0.4μm, and 0.1μm) were measured to prepare for analysis. For each fraction, 0.5 to 2 mg of clay separate was mixed with 1 to 4 mg of BaF to reduce the amount of sample splash during the analysis. The mixture was loaded onto a Pt-sample holder and placed within the analysis chamber, where the vacuum of 10^{-6} Mbar was set and pure fluorine BrF_5 was used to pre-fluorinate the chamber overnight (Rumble and Hoering, 1994). During the analysis, a CO_2 laser beam was used to heat clay minerals and make them react with the F to release O_2 while there was no reaction with the surrounding material (Rumble and Hoering, 1994). To separate excess fluorine from the O_2, KCl was used at 150℃ to react with it. The extracted O_2 was collected in a molecular sieve (mesh size 5 Å) immersed in liquid nitrogen. With reheating, the O_2 expanded into the inlet of the mass spectrometer. The average precision of the in-house standard, NBS-28 quartz is ± 0.1‰ with a standard value of +18.1‰, and the accuracy for $\delta^{18}O$ values is better than ± 0.2‰.

3.2.4.2 Hydrogen mass spectrometry

Hydrogen isotopic analysis of clay fractions was completed with a TC/EA coupled to a gas chromatographic column and a mass spectrometer (Bauer and Vennemann, 2014) at Goethe University, Germany. To remove moisture from the surrounding air and avoid the effect of H in the air on analysis, the measured samples were separately placed into a quartz glass tube, connected to a vacuum extraction line of ca. 0.045 mbar, and put into an external tube furnace to preheat to 200℃ through overnight. The released water vapour was pumped. Under the

conditions without noticeable degassing but with stable pressure, the isolated sample was reheated with a torch to up to 1500℃ to liberate hydrogen gas. The water vapour was produced with the oxidation of hydrogen gas caused by a heated reservoir of CuO, trapped with the liquid nitrogen, and separated from other gases like CO_2 by distinct cold traps. Eventually, the water vapour was trapped into a glass tube filled with Zn, and heated with the tube to 500℃ to form H_2 gas, which was analyzed in the mass spectrometer.

Two standards were used to normalize the measured isotopic composition: in-house biotite (G-1) and kaolinite (K-17). While the δD value of G-1 biotite is −66‰, of K-17 kaolinite is −125‰. Hydroxyl contents are 3.19 wt% for biotite but 14.5 wt% for kaolinite (Vennemann and O'Neil, 1993). Precision on the in-house standards was better than ± 2‰ for this method.

Chapter 4: Results

4.1 Petrography and Thin Section Images of Wall Rocks

There are 10 thin sections from wall rocks along the Gondwana-Diuri contact, the MBT, and the MFT (Table 2.1). They are described with 4 parts.

Diuri samples 86 taken from the Gondwana-Diuri contact show coarse grains with more than 15% matrix, and the hand sample from the hanging wall is coarser than that in the footwall (Figure 4.1, top). The samples contain quartz, mica (most muscovite), feldspar, kaolinite, and clay minerals which is too fine to identify. They are graywackes/diamictites.

Samples 97 and 98 come from the Gondwana-Siwalik contact (the MBT). From the middle two micrographs in figure 4.1, samples 98 contain sub-rounded coarse grains and ~ 15% matrix with the minerals of quartz, mica (most muscovite), feldspar, and very fine clay minerals. Like samples 89, the hanging wall sample look coarser than the footwall, but the footwall sample includes more broken grains than the hanging wall. They are graywackes.

Samples 182 are from the Siwalik Group and contain much smaller coarse grains but less broken in the footwall than those in the hanging wall (bottom views in Figure 4.1). The matrix is ~ 10%. The footwall sample shows lamination texture formed by the alignment of mica minerals. The samples involve quartz, mica (most muscovite), plagioclase, and very fine clay minerals. They are sandstones.

The MFT Samples 89 inversely show relatively finer grains in the hanging wall but coarser in the footwall (Figure 4.2). From the footwall micrograph, the matrix is ~ 10%. The present minerals include quartz, mica (most muscovite), feldspar, and very fine clay minerals. They are alluvial sandstones.

Comparing these micrographs, we found that Diuri samples 86 show the largest grains, and that the grain size decreases from the Diuri Formation, MBT, Siwalik to MFT. Almost all samples contain quartz, feldspar, mica (most muscovite), and clay minerals. However, based on structural texture, 86 and 98 include more than ~ 15% of matrix while 182 and 89 do not. Also, only the footwall sample182 shows perfect lamination. The acquired micrographs are summarized in Appendix A.

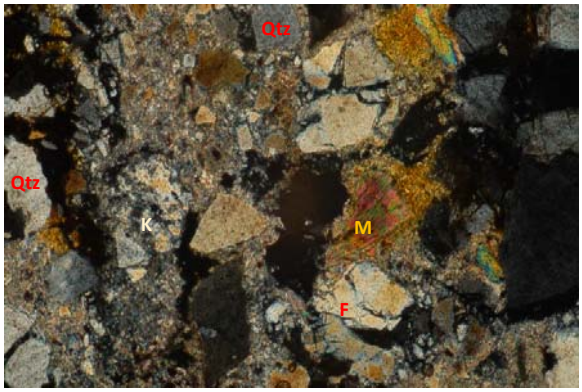

2.5 mm

BH86B_FW

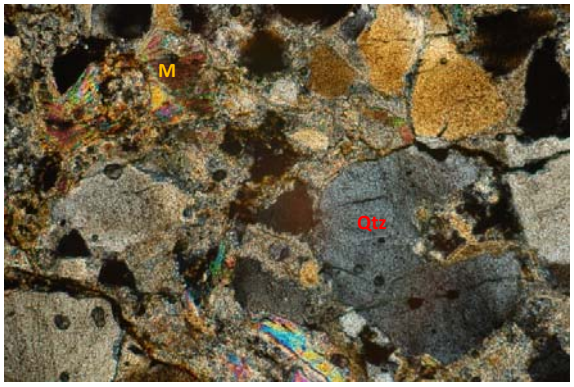

2.5 mm

BH86C_HW

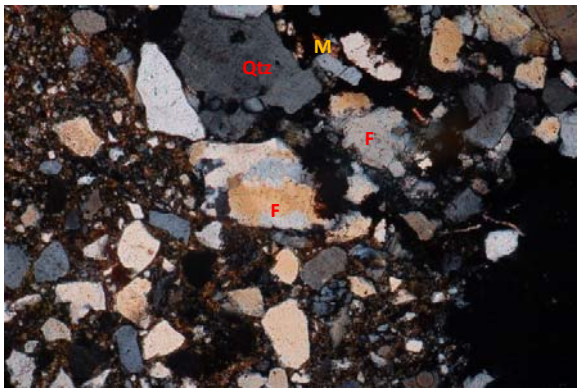

2.5 mm

BH98D_FW

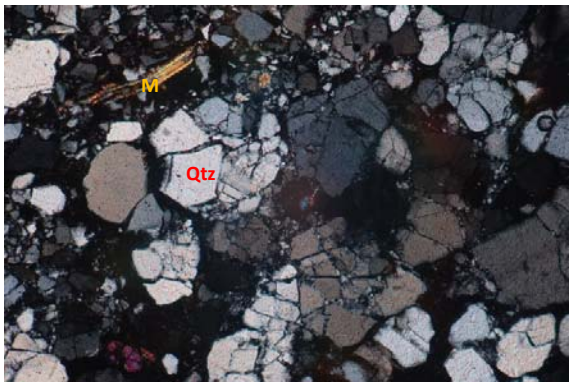

2.5 mm

BH98CI_HW

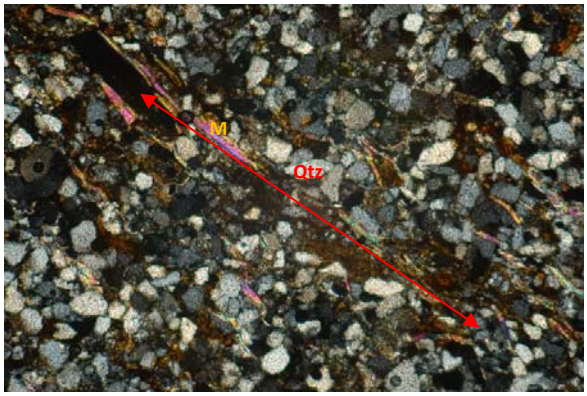

2.5 mm

BH182A_FW

2.5 mm

BH182C_HW

Figure 4.1 Micrographs of Diuri samples 86, MBT samples 98, and Siwalik sample 182, using cross polarized light. FW – Foot Wall; HW – Hanging Wall. The red line with arrows in both ends shows lamination texture. Qtz – quartz, M – Mica, F – Feldspar, and P – Plagioclase.

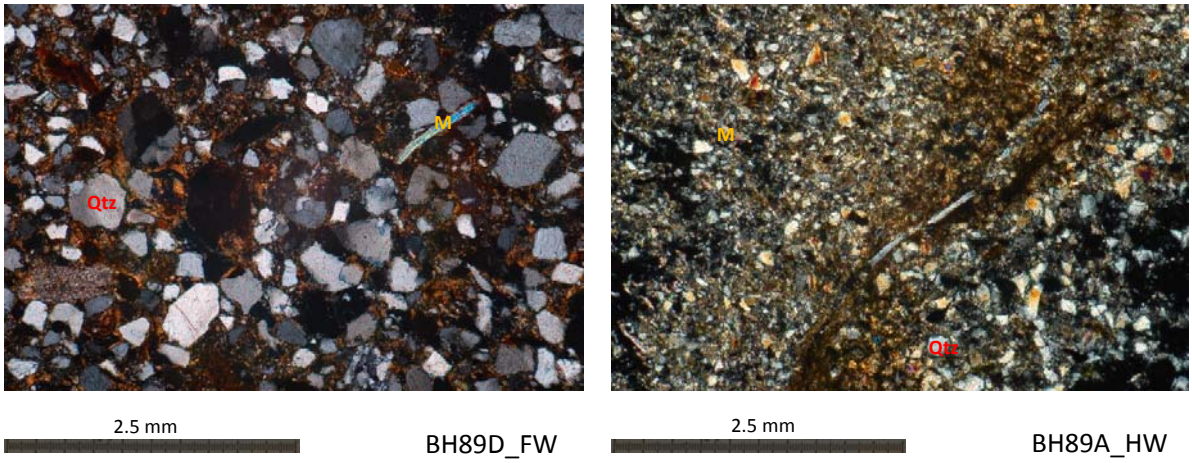

Figure 4.2 Micrographs of MFT samples 89, using cross polarized light. FW – Foot Wall; HW – Hanging Wall. Qtz – quartz and M – Mica.

4.2 Mineralogy of fault gouge samples

All gouge samples consist predominantly of illite, kaolinite, mica, and quartz, and some involve accessory minerals like chlorite. The identification procedure was completed by the software, which lists mineral patterns with the highest probabilities after comparing sample peaks with net profile data, as well as by geological background and knowledge from my supervisors and me. The XRD results are summarized in Table 4.1, representative diffraction patterns are shown in Figure 4.3, and all acquired XRD patterns are given in Appendix C.

Only fault gouge from the MFT site was found to contain smectite, the presence of which is evidenced by the shift of the peak in the 001 reflection at around 6° 2θ after glycolation with increasing intensity. Likewise, 182 series from Dogar-Panbang location, Siwalik unit are merely gouge samples containing illite-smectite identified by the same shift as smectite but decreasing intensity after glycol treatment. Other gouge samples including 86 series from Diuri unit and 97-98 series from the MBT site, contain variations of chlorite. In addition, some feldspar might be present in samples 182BI, 182BII, and 98B, but further evidence is still required. Based on the similarities of clay minerals and associated minerals determined, 11 gouge samples are divided into 4 groups shown by distinct colors in Table 4.1: Diuri samples 86 and MBT sample 98B in the most lightly orange group, MBT samples 97and 98A in the pink group, Siwalik samples 182 in the orange group, and MFT samples 89 in the blue group.

Table 4.1 Catalogue of Samples

Sample	Location	Latitude/ Longitude	Unit	Lithology	Sm	I/S	I	K	Chl	M	Qtz	F
86AI	Bangtar	N26.87905 E91.66777	Diuri	Graywacke /Diamictite			**	*	**	**	*	
86AII	Bangtar	N26.87905 E91.66777	Diuri	Graywacke /Diamictite			**	*	**	**	*	
98B	Deothang coal mine	N26.84879 E91.45037	MBT	Graywacke			*	*	**	**	*	?
97AII	Deothang coal mine	N26.84909 E91.44968	MBT	Graywacke			*	**	*	**	**	
97B	Deothang coal mine	N26.84909 E91.44968	MBT	Graywacke			*	**	*	**	**	
98A	Deothang coal mine	N26.84879 E91.45037	MBT	Graywacke			*	**	*	*	**	
182BI	Dogar-Panbang	N26.8089 E90.95769	Siwalik	Sandstone		*	**	**		**	**	?
182BII	Dogar-Panbang	N26.8089 E90.95769	Siwalik	Sandstone		*	**	**		**	**	?
89BI	Daranga Mella, S.Jongkhar	N26.79199 E91.5108	MFT	Alluvial Sandstone	*		**	**		**	*	
89BII	Daranga Mella, S.Jongkhar	N26.79199 E91.5108	MFT	Alluvial Sandstone	*		**	**		**	*	
89C	Daranga Mella, S.Jongkhar	N26.79199 E91.5108	MFT	Alluvial Sandstone	**		**	**		**	*	

** abundant; * present; ? not sure.

Illite, kaolinite, and mica are notable by their presence in all samples examined. Illite and kaolinite are abundant in most samples while mica is rich in almost all samples. Thus, fault gouge samples are dominantly a mixture of clay minerals and detrital mica. Furthermore, kaolinite is present in all samples, and it coexists with either smectite, illite and mica, or illite-smectite mixed layers, illite and mica, or illite and mica, besides quartz and possible feldspar. These mineralogical combinations probably suggest that the protoliths and fault gouges have well interacted with fluids (Buatier et al., 2012). In addition, the existence of illite indicates the presence of K-bearing phases, which are crucial for fault dating. However, illite may be formed by five distinct processes: diagenesis, metamorphism, surface weathering, dissolution / precipitation, and faulting (Lanson et al., 2009; Gharrabi et al., 1998; Vrolijk and Van der Pluijm, 1999; Pevear, 1999; Fowler and Yang, 2003; Huang et al., 1986). Moreover, for quite similar polytypes of illite and mica, it is impossible to be exactly identified by XRD analysis with available instruments. Therefore, illite formation conditions cannot be determined through only XRD analysis. Besides, the presences and characteristics of these minerals still need to be supplemented by information from other analytical techniques, like SEM/EDS and TEM

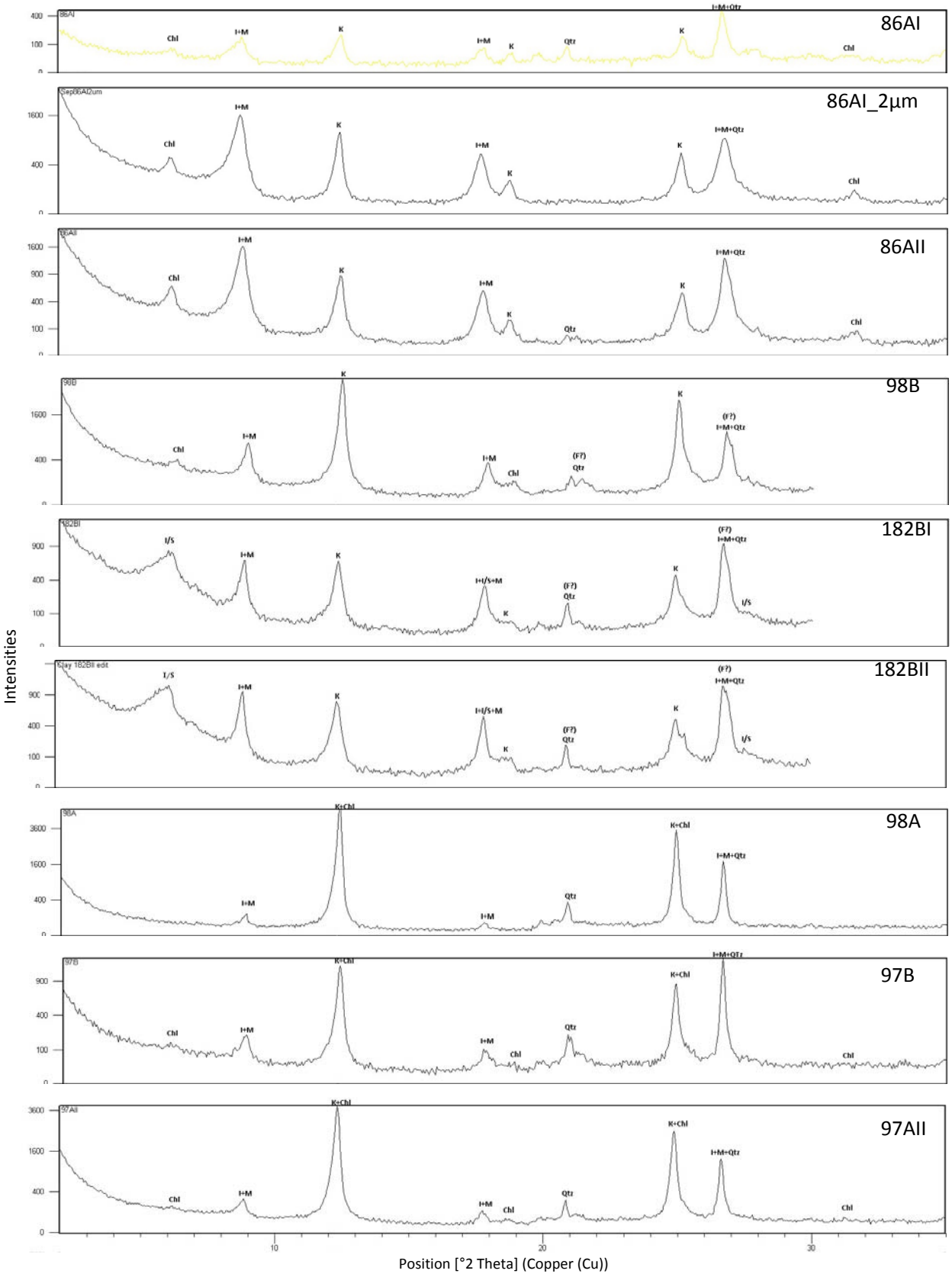
86AI
86AI_2µm
86AII
98B
182BI
182BII
98A
97B
97AII
Intensities
Position [°2 Theta] (Copper (Cu))

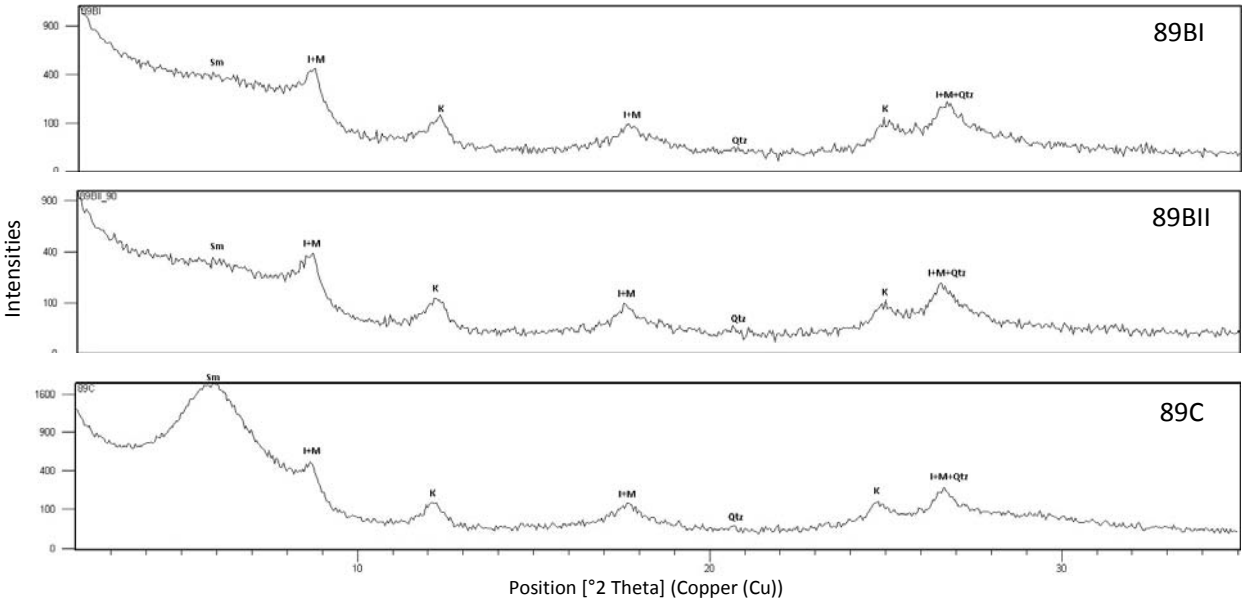

Figure 4.3 Representative X-ray diffractograms of fine fault gouge samples. Symbols: Sm – smectite, I/S – illite-smectite, I – illite, K – kaolinite, Chl – chlorite, M – mica, Qtz – quartz, and F – feldspar.

analysis, due to uncertainties of some mineral phases determined caused by similarity of illite-mica polytypes.

4.3 SEM/EDS and TEM Results on Clay Morphology and Composition

On the SEM micrographs, illite shows thin flakes in the Diuri samples and Sikkim Siwalik but has interwoven ribbon or needle-like shape within 1 μm in length in the MBT samples (Figure 4.4 a) & b)). The SEM image of the only Sikkim Siwalik sample was used as a reference. EDS indicates that these samples contain major elements as Si, Al and K, and a minor amount of Mg and Fe. I could not obtain good SEM images displaying illite in the MFT samples. However, illite with less than 0.5 μm in size and lath shape was found by TEM observations (Figure 4.5 a)-e)). Comparing to illite, mica shows platy or elongated shape with approximately 0.5 – 2.5 μm, and it contains more K and Fe than illite in EDS spectrum (Figure 4.4 d); 4.5 a)-c) & f)). Additionally, EDS analysis shows that mica particles contain Si, Al, K, Mg, Fe and Ti. The presence of both illite and mica in SEM/EDS and TEM results confirms the quantitative XRD determinations.

Smectite from MFT samples 89 is characterized by slightly flaky appearance with around 1 μm in size and equigranular crystallites in SEM images (Figure 4.4 c)). Samples contain the major elements of Si, Al, Ca, Mg, Fe, and K, as well as trace Na. The Ca and trace Na probably

represent interlayer cations. However, smectite shows either a fluffy appearance as aggregations of very small grains or curled edges as darker colored spheres in TEM images (Figure 4.5 d)-f)).

Table 4.2 Formulas and Morphological Features of minerals identified in fault gouge samples (Welton, 2004; Beutelspacher and Van der Marel, 1967; Sudo et al., 1981)

Samples with Formula	Features in SEM/EDS	Features in TEM
Smectite $(0.5Ca,Na)_{0.7}(Al,Mg,Fe)_4[(Si,Al)_8O_{20}]nH_2O$	- Major elements: Si, Al, Ca, Mg, Fe, and K; - webby, flaky, crenulated, or ragged-edged;	- Amorphous admixtures considered as aggregations of very small grains with a fluffy appearance; - Or partly folded irregular lamellae, curled edges, or steep parts as darker colored spheres;
Illite $K_{1-1.5}Al_4[Si_{7-6.5}Al_{1-1.5}O_{20}](OH)_4$	- Major elements: Si, Al, and K with a minor amount of Mg, Ca, and Fe; - thin flakes with ribbon-like projections, or needle-like shape;	- Angular platy particles and some laths with relative smaller size
Mica $AB_{2-3}(X, Si)_4O_{10}(O, F, OH)_2$ where A might be K or Na, and B can be Al, Fe, or Mg.	- Major elements: Si, Al, K, Mg, Fe and Ti; - large and platy particles;	- Large and platy shape with angular borders; - Sometimes platy or elongated pseudo-hexagonal shape;
Kaolinite $Al_4[Si_4O_{10}](OH)_8$	- Major elements: Si and Al; - Nearly equal peak heights of Si and Al; - Face-to-face stacks of pseudo-hexagonal plates, or book shape, or blocky morphology;	- Pseudo-hexagonal shape; - Some may be very small and sometimes curled platy particles;
Chlorite $(Mg,Al,Fe)_{12}[(Si,Al)_8O_{20}](OH)_{16}$	- Major elements: Si, Al, Mg, and Fe; - Most are Fe-rich; - Small stacks of platelets, pseudo-hexagonal shape, and irregular edges;	- Only platy particles appear with perfect cleavage towards the base; - Sometimes interference figures, resulting from stress after weathering, are found;
Quartz SiO_2	- Major elements: Si; - large and blocky particles;	- Rhombohedral morphology, or large crystal with hexagonal morphology;

Interstratified illite-smectite is very hard to identify through SEM/EDS analysis, but platy shape and admixtures of very small grains with a fluffy appearance in TEM micrographs point out their presence (Figure 4.5 c)). On the other hand, kaolinite is observed with ~ 0.5 – 2.5 μm size and blocky morphology in SEM observation and mainly contains Si and Al (Figure 4.4 e)). Likewise, quartz shows largely blocky shape with about 10 μm in size in SEM micrograph and only Si as major element (Figure 4.4 f)). Additionally, chlorite might be identified from SEM/EDS analysis with uncertainty caused by the quite broad scanning range of the interaction between electron beam and sample, but it cannot be determined by TEM image due to its similarity with mica. Chemical formulas and morphological features in SEM and TEM observations of clay and associated minerals determined are summarized in Table 4.2. The acquired SEM/EDS and TEM results are given in Appendix C.

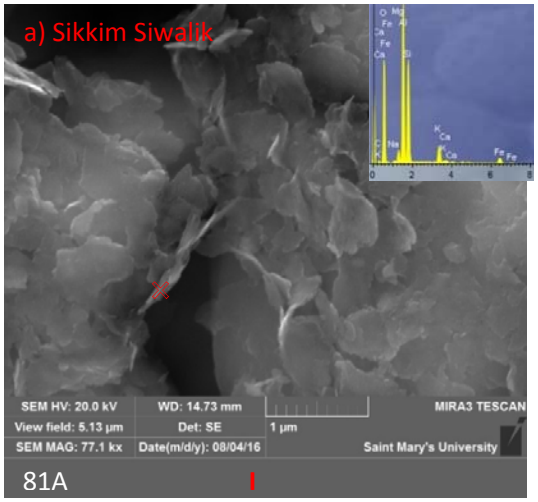

Note: EDS spectrum with point composition "X"

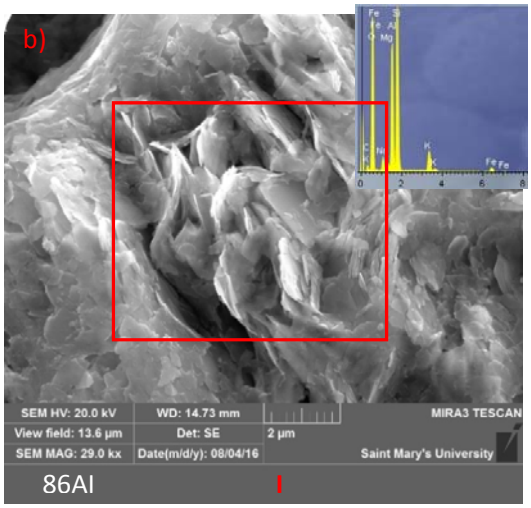

Note: EDS spectrum with average scan

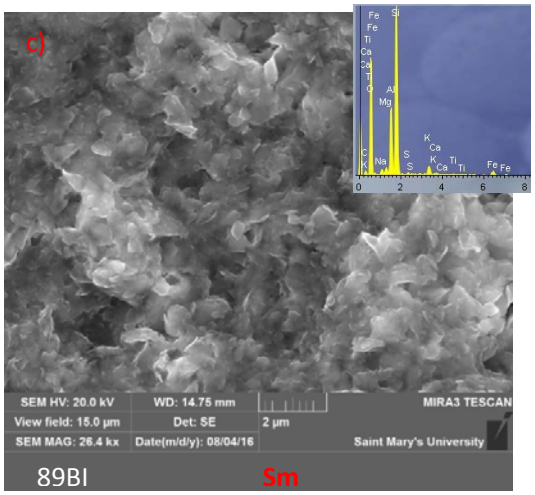

Note: EDS spectrum with average scan

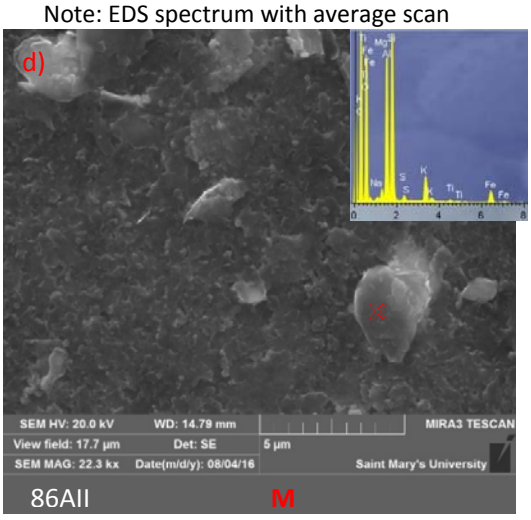

Note: EDS spectrum with point composition "X"

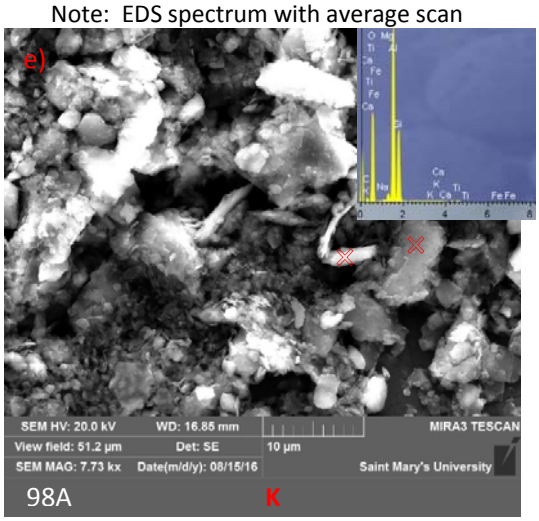

Note: EDS spectrum with point composition "X"

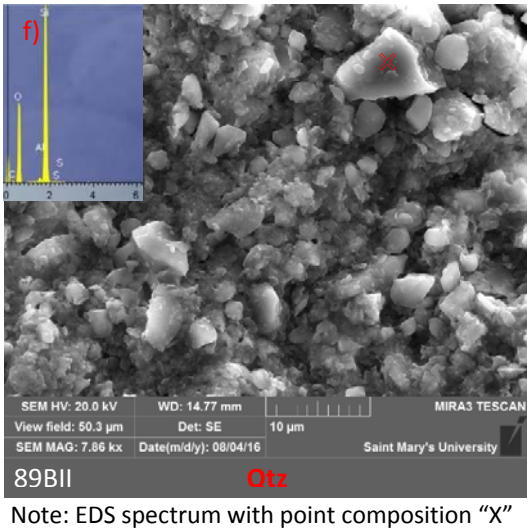

Note: EDS spectrum with point composition "X"

Figure 4.4 SEM images with EDS spectrums show the presence of dominant minerals. I – illite, Sm – smectite, M – mica, K – kaolinite, and Qtz – quartz.

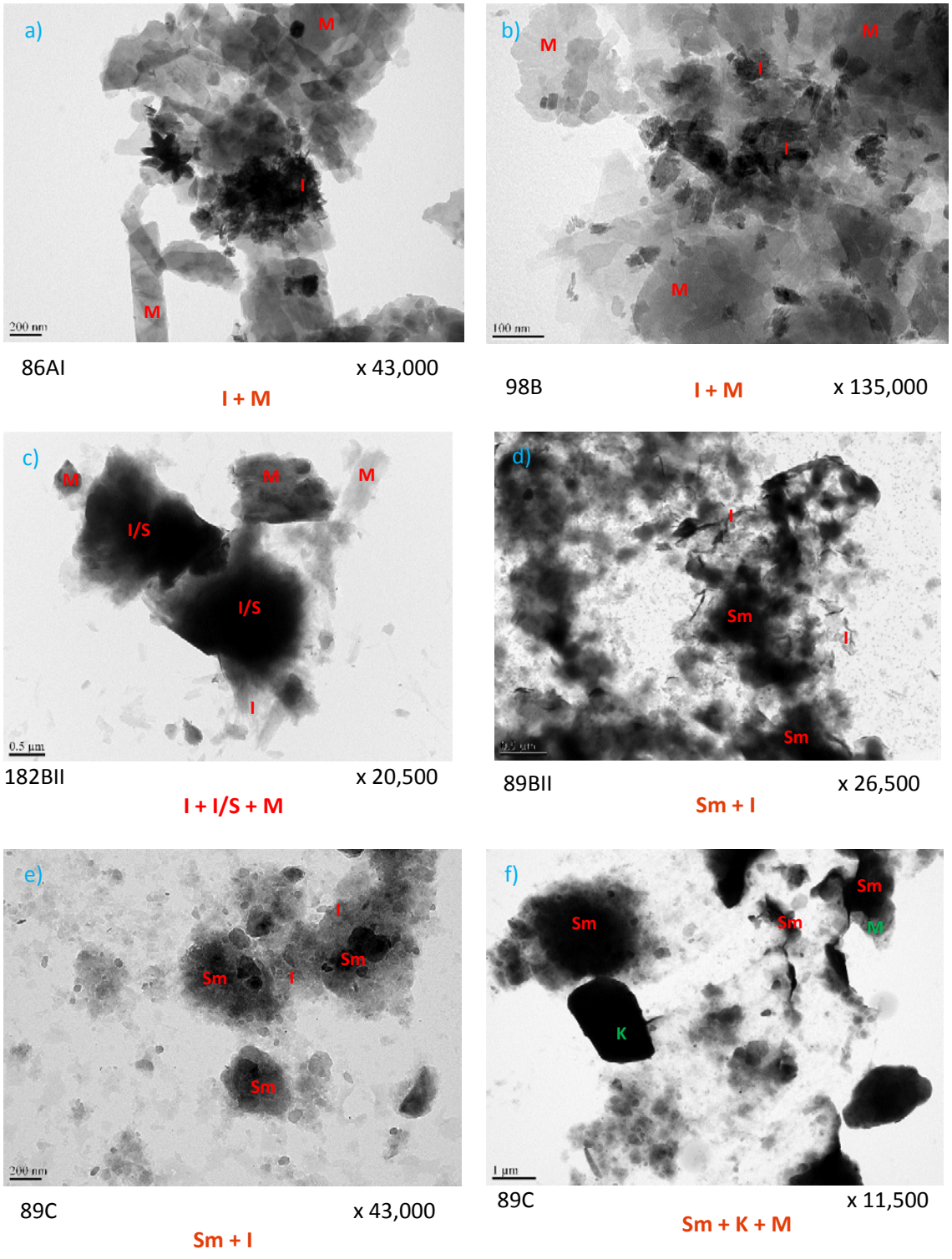

Figure 4.5 TEM images show the presence of smectite (Sm), illite (I), illite-smectite (I/S), kaolinite (K), and mica (M) as representatives.

4.4 Isotope Geochemistry

The VSMOW values of $\delta^{18}O$ and δD stable isotopes for extracted clay samples are shown in Table 4.3. Since there is very little mass (< 0.2 g) obtained from separated fractions (0.1μm, 0.4μm, 2μm) of Diuri samples 86 and MBT sampe 97 AII, as well as from 0.1μm fraction of MBT samples 97B and 98A, we don't have any isotopic data for them. Briefly, the $\delta^{18}O$ isotope values range from 10.9 (89BI_0.1μm) to 15.1 ‰ (89C_0.1&0.4μm) except six pending fractions. δD values cover the range from -105.6 (182BI_0.1μm) to -90.3 ‰ (98A_2μm). According to isotopic result of $\delta^{18}O$, Siwalik samples have relatively smaller values while MBT samples and MFT samples 89 BI&BII show relatively higher ones, but MFT sample 89C has the largest $\delta^{18}O$ isotopic value. In addition, there is no evident relation between grain fraction and isotopic composition (Figure 4.6 (a)-(b)). Siwalik samples and MFT sample 89C are relatively more depleted in δD than MFT samples 89 BI&BII, and MBT samples are relatively least depleted in δD.

Table 4.3 Measured Isotopic Values of Clay Samples

Unit	Location	Gouge Sample	Size Fraction (μm)	$\delta^{18}O$ (‰ SMOW)	δD (‰ SMOW)
MBT	Deothang coal mine	97B	0.4	12.5	-95.8
MBT	Deothang coal mine	98A	0.4	13.4	-93.2
			2		-90.3
MBT	Deothang coal mine	98B	0.1		-101.5
			0.4	12.8	-97.7
			2		-97.5
Siwalik	Dogar-Panbang	182BI	0.1	11.6	-105.6
			0.4	11.6	-101.1
			2		-101.8
Siwalik	Dogar-Panbang	182BII	0.1		-104.5
			0.4	11.2	-103.7
			2		-99.2
MFT	Daranga Mella, S.Jongkhar	89BI	0.1	10.9	-99.7
			0.4	11.6	-100.3
			2	12.3	-100.6
MFT	Daranga Mella, S.Jongkhar	89BII	0.1	11.2	-97.2
			0.4	11.4	-95.8
			2	12	-101.8
MFT	Daranga Mella, S.Jongkhar	89C	0.1	15.1	-104.3
			0.4	15.1	-102.0
			2	14.9	-103.3

Since illite presents in all gouge samples, the mean isotopic composition for each sample are plotted in Figure 4.7 (A), to compare with references in Data Repository Files DR5 and DR6 (Haines et al., 2016). The plot of illite data shows that illites are like the ones from "meteorically reset" sedimentary basins, which formed during the flushing of basin with meteoric water. Likewise, smectites only in MFT samples 89 demonstrate the similarity to smectites in sedimentary basins or from bentonites or even from hydrothermal systems, based on the plots in Figure 4.7 (B). However, chlorites from MBT samples are different with chlorites produced in given geological environment data (Figure 4.7 (C)). This suggests that chlorites have been formed neither in sedimentary basins (diagenesis) nor from hydrothermal systems or in metamorphic rocks (detrital component in the Siwalik sediments).

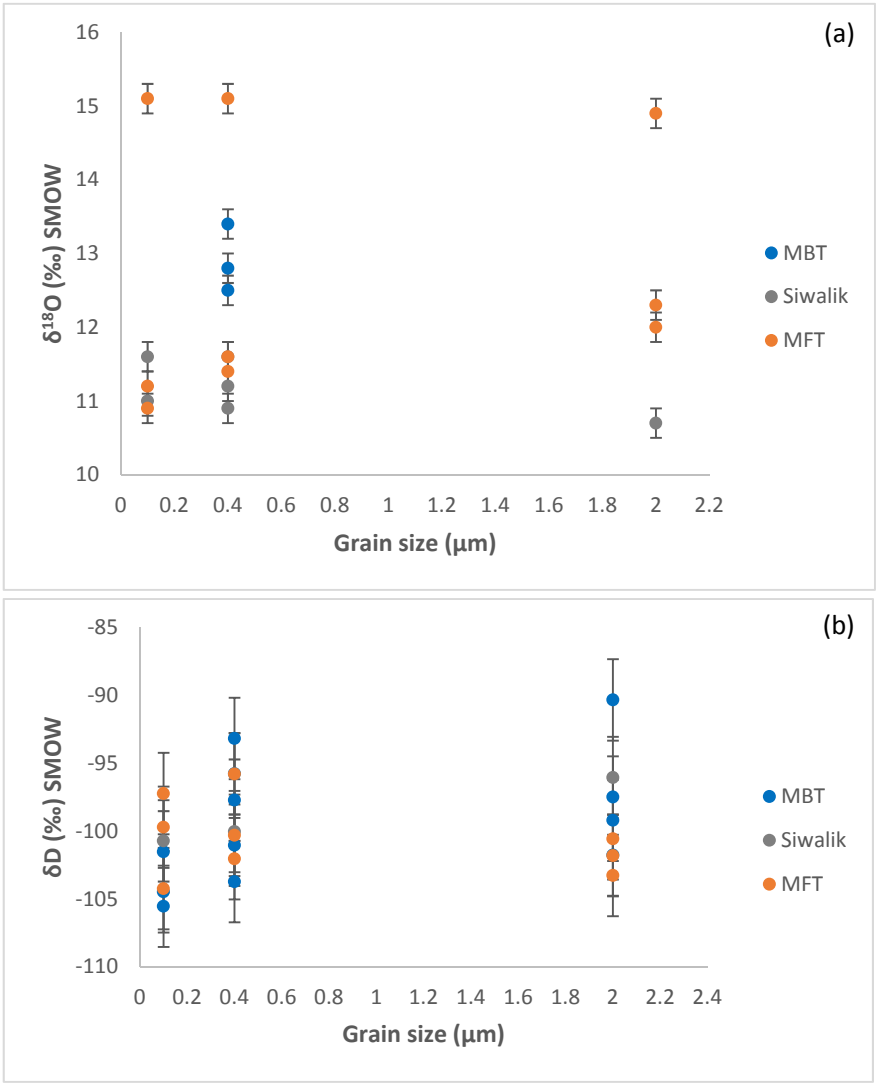

Figure 4.6 a) Relation between grain fraction and $\delta^{18}O$ isotopic composition; b) Relation between grain fraction and δD isotopic composition.

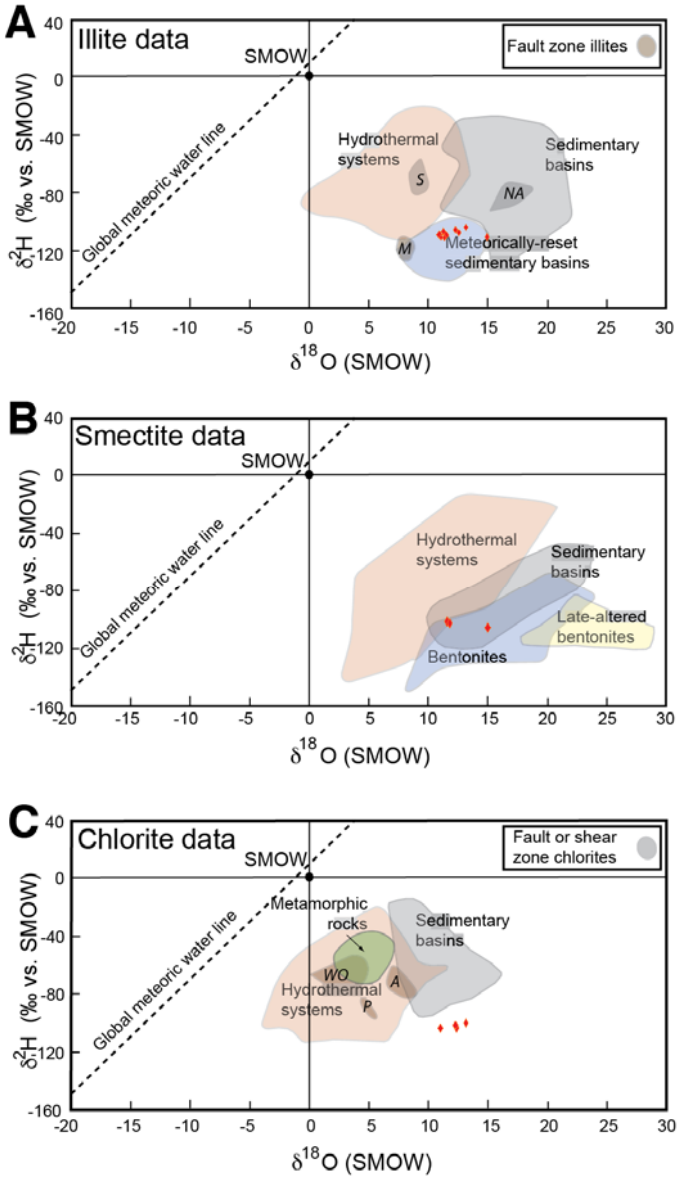

Figure 4.7 Illite, smectite, and chlorite isotopic data comparing with references in Data Repository Files DR5 and DR6. (Provenance fields modified after Haines et al., 2016.) Red diamond symbols represent the mean isotopic data for corresponding samples.

Chapter 5: Discussion

5.1 Origin of Clay Minerals

The mineralogical investigation of fault gouge samples from the frontal Himalaya in the eastern Bhutan implies that the fault gouges and protoliths contain two clay types: (a) 2:1 layers, such as smectite, illite-smectite, and illite; (b) 1:1 layers like kaolinite. Based on the δD negative values from ~ -106 to -90 ‰, clay minerals in this study have formed primarily from meteoric fluids.

Smectite has been crystallized by the interaction between fault gouge and meteoric water, evidenced by four points. (1) the coexistence of smectite and illite in MFT samples 89 indicate that there was no metamorphic reaction (Gharrabi et al., 1998; Mancktelow et al., 2015). (2) without interstratified illite-smectite layers, relatively pure smectite only forms at low temperature under near-surface conditions (Mancktelow et al., 2015). (3) the coexistence of smectite and illite suggests that they formed in meteorically-reset sedimentary basins, combining with the plotting results of sample data (Figure 4.5). (4) 89C containing the most abundant smectite has the most negative δD value among MFT samples (Mancktelow et al., 2015).

The origin of illite is the most complex. The presences of smectite in MFT samples 89 and of illite-smectite in Siwalik samples 182 indicate that there was no metamorphic illite formed in the two sites (Gharrabi et al., 1998; Mancktelow et al., 2015). Also, quite abundant illite with mixed illite-smectite layers in Siwalik samples 182, indicates that illite may form under the low temperature geological setting by K-rich and pervasive fluid flow, which helps overcome the kinetic barriers to reaction (Vrolijk et al., 1999). Eventually, the formation of authigenic illite is evidenced by O and H isotopic analyses (See section 5.2).

The presence of kaolinite in all samples suggests that faulting did not induce significant shear heating (Buatier et al., 2012). Kaolinite was directly precipitated from meteoric fluids as evidenced by mineral aggregation determined and isotope analyses (See section 5.2). The fluids reduce kinetic barriers and promote local dissolution-precipitation reactions to produce kaolinite (Vrolijk et al., 1999).

In short, clay authigenesis occurred in fault gouges along the MBT and MFT and involved the formation of smectite, illite-smectite, smectite, and kaolinite. These clay minerals have not

formed by surface weathering but most likely formed in the fault gouge by interaction with meteoric water (See section 5.2).

5.2 Condition of Faulting Deformation

5.2.1 The Temperature of Clay Formation

Clay minerals interact with fluids and undergo isotope fractionation processes, therefore the H- and O-isotope studies of clays can provide useful information about the conditions of formation (Sheppard and Gilg, 1996). Depending on the uncertainties caused by the variation of clay minerals, two approaches were used to calculate the temperature of clay formation.

Assuming that smectite represent all the clays in samples, one can apply the direct paleotemperature equation by Delgado and Reyes (1996):

$$3.54\times10^{6}T^{-2} = \delta^{18}O_{sm} - 0.125\delta D_{sm} + 8.95 \qquad (5.1)$$

Where *T* is temperature in *K*. The paleotemperatures of ~ 59.9˚C is obtained by the mean measured isotopic values.

The second geothermometer is based on kaolinite. Assuming that kaolinite is the only clay mineral formation and transformation of minerals in equilibrium with meteoric waters, the temperature for all samples with paired $\delta^{18}O_{kaol}$ and δD_{kaol} measurements can be calculated by the following equation (Mix et al., 2016):

$$3.0350\times10^{6}T^{-2} = \delta^{18}O_{kaol} - 0.1250\delta D_{kaol} + 7.0375 \qquad (5.2)$$

where *T* is the absolute temperature in *K*.

While smectite geothermometer yields the range of the equilibration temperature from 35. 8 °C to 61.2 °C, based on kaolinite thermometer, the equilibration temperatures range between 20.6 °C and 46.3 °C with the standard error of ± 1.6 ˚C (Table 5.1). Furthermore, both of them indicate that MFT sample 89C formed at the lowest temperature while other samples recorded relatively similar temperatures. Importantly, these data reveal that meteoric waters have been involved in the formation of clay minerals.

5.2.2 Paleo-meteoric Fluids

The global meteoric water line (GMWL) and the local meteoric water line (LMWL) of eastern Bhutan can be plotted, separately based on the linear relationships between $\delta^{18}O$ and δD values (Rozanski et al., 1993; Figure 5.1).

$$\delta D = 8.20 \times \delta^{18}O + 11.27 \quad (5.3)$$

$$\delta D = 7.24 \times \delta^{18}O - 0.97 \quad (5.4)$$

From the equations, the GMWL slope is 8.20, slightly higher than that of LMWL with 7.24, and the intersection point of the two lines is at -11 ‰ $\delta^{18}O$, -78‰ δD. According to Sheppard and Gilg (1996), the supergene-hypogene line (S/H) is equivalent to kaolinite at isotopic equilibrium with meteoric waters at temperature of ~ 35 ˚C (Figure 5.1). As shown in figure 5.1, the plot of clay isotopic data indicates that the majority of clay samples formed above ~ 35 ˚C with two MBT samples 98 around 35 ˚C and three fractions of MFT sample 89C below 35 ˚C. This further confirms the temperatures of clay formation as discussed in subsection 5.3.1.

To further interpret clay formation conditions, the isotopic composition of the waters involved in the transformation from initial minerals to clays must be done. Depending on fractionation processes involving meteoric water at isotopic equilibrium with variable clay minerals, the corresponding isotopic compositions of meteoric water can be determined assuming the temperature of equilibration.

The isotopic compositions of meteoric water can be calculated by subtracting fractionation factors for both O and H isotopes from the clay isotopic composition. However, such fractionation factors are known only for kaolinite (Sheppard and Gilg, 1996). The hydrogen kaolinite-water fractionation equation:

$$1000\, ln\, \alpha_{K-W} = -2.2 \times 10^6 \times T^{-2} - 7.7 \quad (5.5)$$

and the oxygen kaolinite-water fractionation equation is:

$$1000\, ln\, \alpha_{K-W} = 2.76 \times 10^6 \times T^{-2} - 6.75 \quad (5.6)$$

Where T is the temperature in K and α is the fractionation factor.

Using kaolinite-water fractionation equations, the paleo-meteoric water $\delta^{18}O_{K\text{-}W}$ value ranging from -10.6 to -9.0 ‰ and the $\delta D_{K\text{-}W}$ value between -74.8 and -62.2‰ (Table 5.1). The calculated isotopic values of the paleo-meteoric quite fit the GMWL (Figure 5.1). Which is

Table 5.1 Calculated Temperatures and Isotopic Composition of the Paleo-meteoric Water

Unit	Location	Gouge Sample	Size Fraction (μm)	$\delta^{18}O$ (‰ SMOW)	δD (‰ SMOW)	T_{sm} (˚C)	T_K (˚C)	$\delta^{18}O_{K\text{-}W}$ (‰ SMOW)	$\delta D_{K\text{-}W}$ (‰ SMOW)
MBT	Deothang coal mine	97B	0.4	12.5	-95.8	52.3	37.2	-9.4	-65.2
MBT	Deothang coal mine	98A	0.4	13.4	-93.2	49.5	34.4	-9.0	-62.2
MBT	Deothang coal mine	98B	0.4	12.8	-97.7	49.7	34.6	-9.6	-66.8
Siwalik	Dogar-Panbang	182BI	0.1	11.6	-105.6	50.7	35.6	-10.6	-74.8
			0.4	11.6	-101.1	53.5	38.4	-10.1	-70.7
Siwalik	Dogar-Panbang	182BII	0.4	11.2	-103.7	53.8	38.7	-10.4	-73.4
MFT	Daranga Mella, S.Jongkhar	89BI	0.1	10.9	-99.7	57.8	42.8	-10.0	-70.0
			0.4	11.6	-100.3	53.9	38.9	-10.0	-70.0
			2	12.3	-100.6	50.4	35.2	-10.0	-69.8
MFT	Daranga Mella, S.Jongkhar	89BII	0.1	11.2	-97.2	57.9	42.9	-9.7	-67.5
			0.4	11.4	-95.8	57.8	42.8	-9.5	-66.1
			2	12	-101.8	51.1	36.0	-10.1	-71.1
MFT	Daranga Mella, S.Jongkhar	89C	0.1	15.1	-104.3	35.8	20.6	-10.1	-71.1
			0.4	15.1	-102.0	37.0	21.8	-9.9	-69.1
			2	14.9	-103.3	37.2	22.0	-10.0	-70.3

caused by calculation of the temperature of kaolinite formation (T_K) assuming that the water involved into its forming process falls on the GMWL. Therefore, using the temperature T_K to obtain the isotopic composition of paleo-meteoric water ($\delta^{18}O_{K\text{-}W}$ and $\delta D_{K\text{-}W}$) by kaolinite-water fractionation equations, would cause the water isotopic values to fall on the GMWL. This is a circular reasoning based on the assumption that clays are in equilibrium with meteoric water. All the calculation results are summarized in Table 5.1.

5.2.3 Reconstruction of Brittle Faulting

The average annual temperature at the foot of the Himalaya is 25˚C with the lapse rate of 6˚C (Ohsawa, 1991; Quade et al., 2011). The geothermal gradient in the foreland basin of the Himalaya is 20-30 ˚C/km (Biswas et al., 2007; Landy et al., 2016). The calculated

temperature range of clay samples based on kaolinite geothermometer is the major consideration for the reconstruction of fault gouge formation due to the presence of kaolinite in all samples, while the temperature range based on smectite is only used for sample 89C as a reference because 89C is the only one containing abundant smectite. Therefore, based on the calculated temperature ranges of clay samples, 35. 8 °C (± 1.6 °C)$_{sm}$ for 89C, 20.6 °C (± 1.6 °C)$_{K}$ for 89C, and ~35°C − 46.3 °C (± 1.6 °C)$_{K}$ for other samples, it is suggested that 89C may have formed near surface at the surface temperatures (i.e. by surface weathering) whereas with relatively high equilibration temperatures, other samples may have formed within the depth of 2 km, where water can keep its isotopic composition unchanged (Hoefs, 2015).

The relationship between $\delta^{18}O$ and δD isotopic compositions and elevation can be estimated over moderate elevation range, based on empirical data (Blisniuk and Stern, 2005; Figure 5.2). Using as reference the linear best fit relation between elevation and the isotopic composition of the modern stream waters in the eastern Bhutan (Grujic et al., in review), the calculated isotopic composition ranges of the paleo-meteoric water, -10.6 − -9.0 ‰ $\delta^{18}O_{K\text{-}W}$ and -74.8 − -62.2‰ $\delta D_{K\text{-}W}$ suggests that the paleo-meteoric water originated from the elevations ranging from ~ 2000 to 2500 km (Figure 5.2), which are ~ 1500 – 2000 m higher than the outcrops of fault gouges. In addition, using in situ-produced ^{10}Be, the erosion rate around latitude 27˚00′ N in the Bhutan Himalaya was estimated to 388 ± 32 m/My (Portenga et al., 2015). This mean erosion rate can be used to estimate the time took to exhume the rocks formed at 1-2 km depths. According to the elevation range of ~ 2 – 2.5 km, considering the erosion rate, the meteoric waters may be derived from about 3 km or longer horizontal distance from the site of clay formation (Figure 5.3, blue arrows).

Using structural cross section of eastern Bhutan, the formation condition of fault gouges can be reconstructed, as shown in Figure 5.3. The position where the water penetrated downward may be ~ 3 km or more away to the outcrops of the MBT. For the long path, the horizontal hydrostatic pressure gradient caused by the high relief may contribute to the involvement of the meteoric water into clay formation (Whipp and Ehlers, 2007). However, for the formation of fault gouge from the MFT, which was formed after the MBT and is still active, this deduction cannot work well. It is because there are several fault barriers between the source site of paleo-meteoric water and the MFT. A series of questions is proposed for the formation condition of

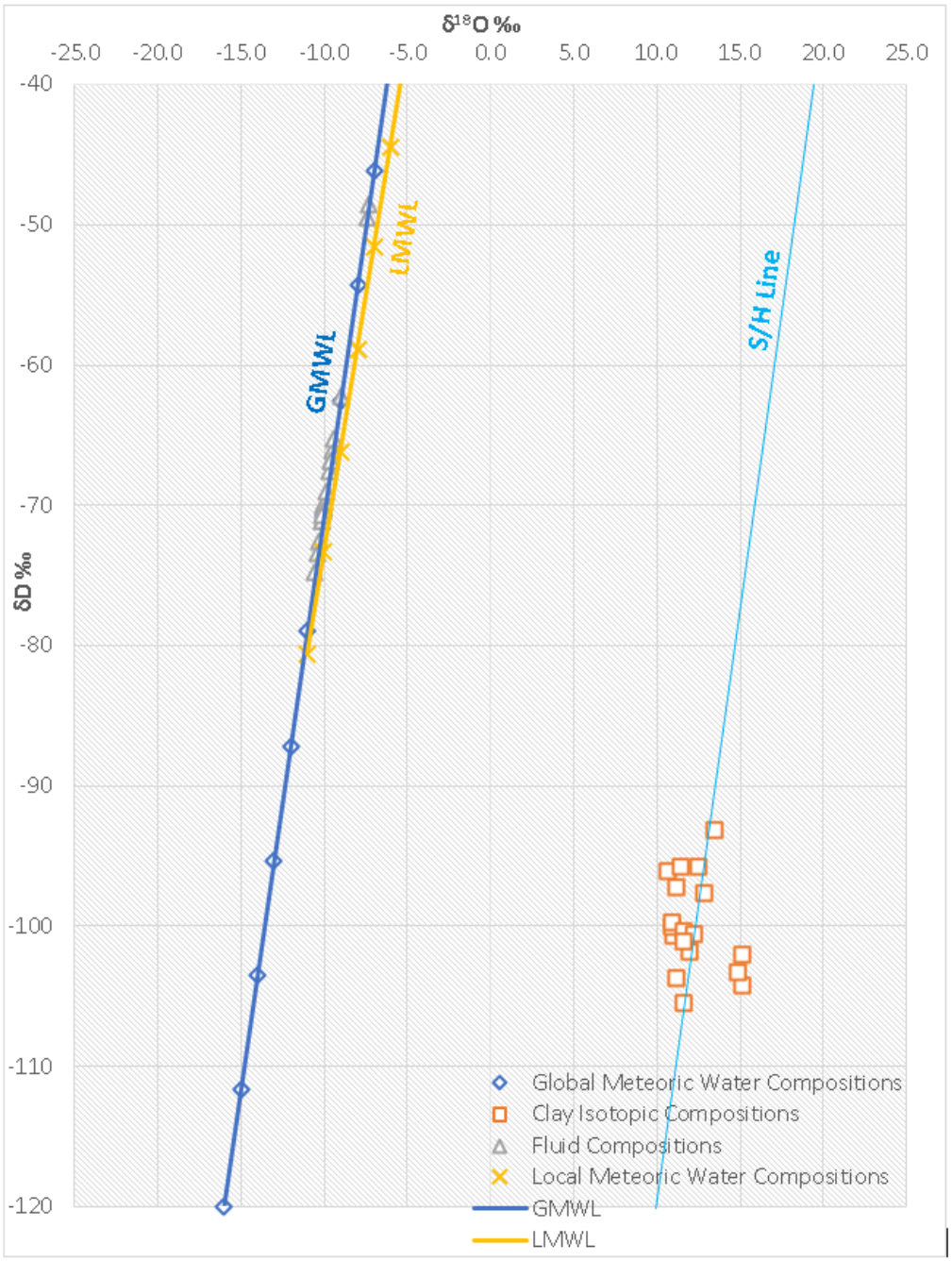

Figure 5.1 The plot of $\delta^{18}O$ against δD showing the isotopic compositions of both clay samples and the paleo-meteoric water (Based on Grujic et al., in review). The thick blue line shows the GMWL while the thick yellow line displays the LMWL. All the composition data for the GMWL and LMWL, labelled as blue diamond and yellow cross symbols, are separately produced by equations (5.3) and (5.4). Light blue S/H line refers to the supergene-hypogene line, which is equivalent to kaolinite in equilibrium with meteoric waters at temperatures of ~ 35˚C (Sheppard and Gilg, 1996). Due to a circular reasoning, all the calculated isotopic compositions of paleo-meteoric water, based on equations (5.1), (5.2), (5.5), and (5.6), fall on the GMWL.

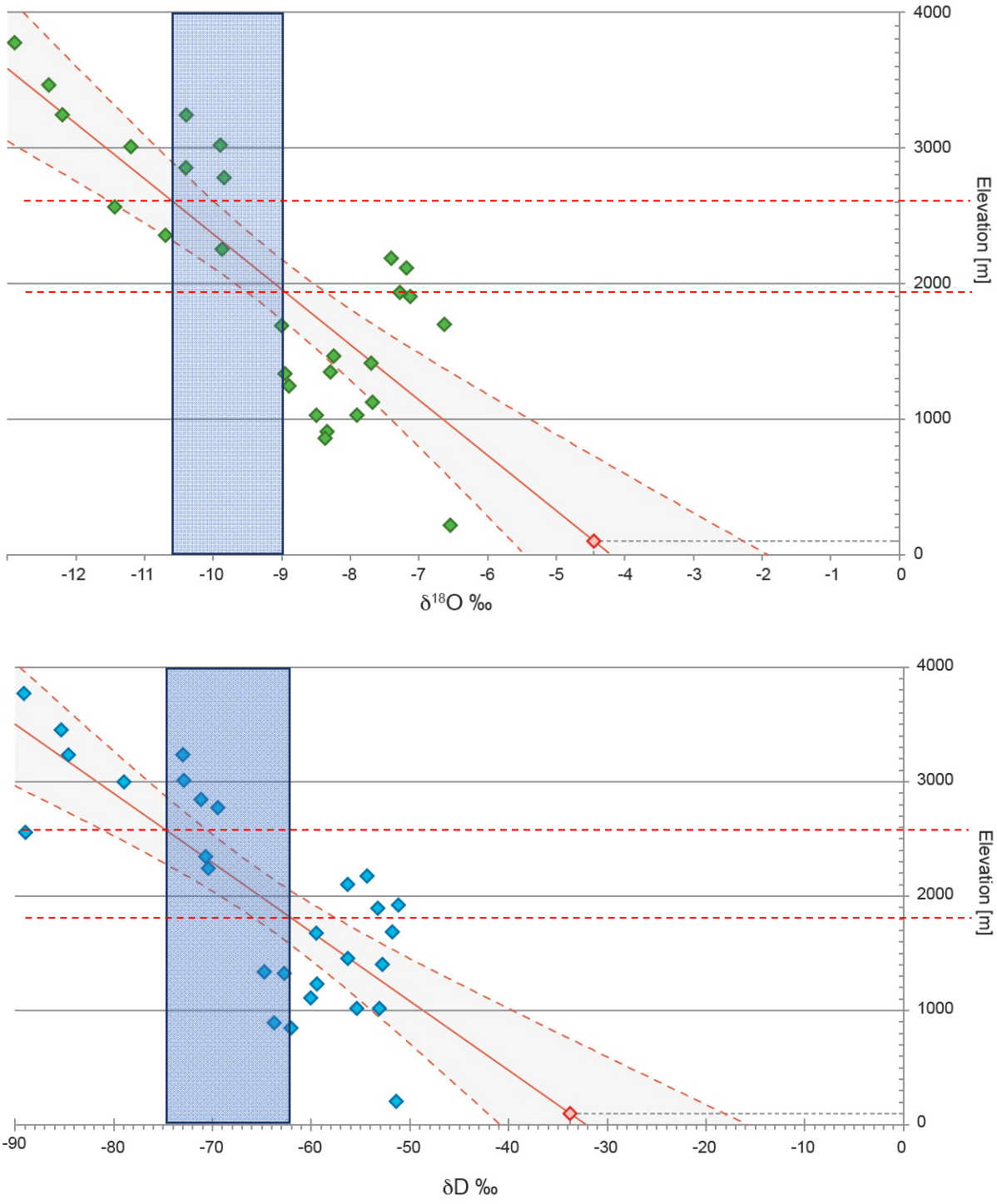

Figure 5.2 The elevation ranges based on the calculated isotopic composition ranges of the paleo-meteoric water, using the linear best fit line labeled as the orange straight line. (Based on Grujic et al., in review). The two transparently blue boxes label the calculated isotopic composition ranges of the water while the red dash lines mark the corresponding elevation ranges. Green and blue diamond symbols are from the original data (26.8 and 27.6 °N). Red symbols indicate the expected mean isotopic composition of meteoric water at 100 m. The dashed curved lines are the 2σ.

fault gouge along the MFT: 1) whether the surface water can pass through the fault barriers to the MFT site; 2) how; 3) if the answer of question 1) is no, where was the paleo-meteoric water derived from. Therefore, the interpretation of the stable isotopic compositions of clays from the MFT fault gouge requires further research.

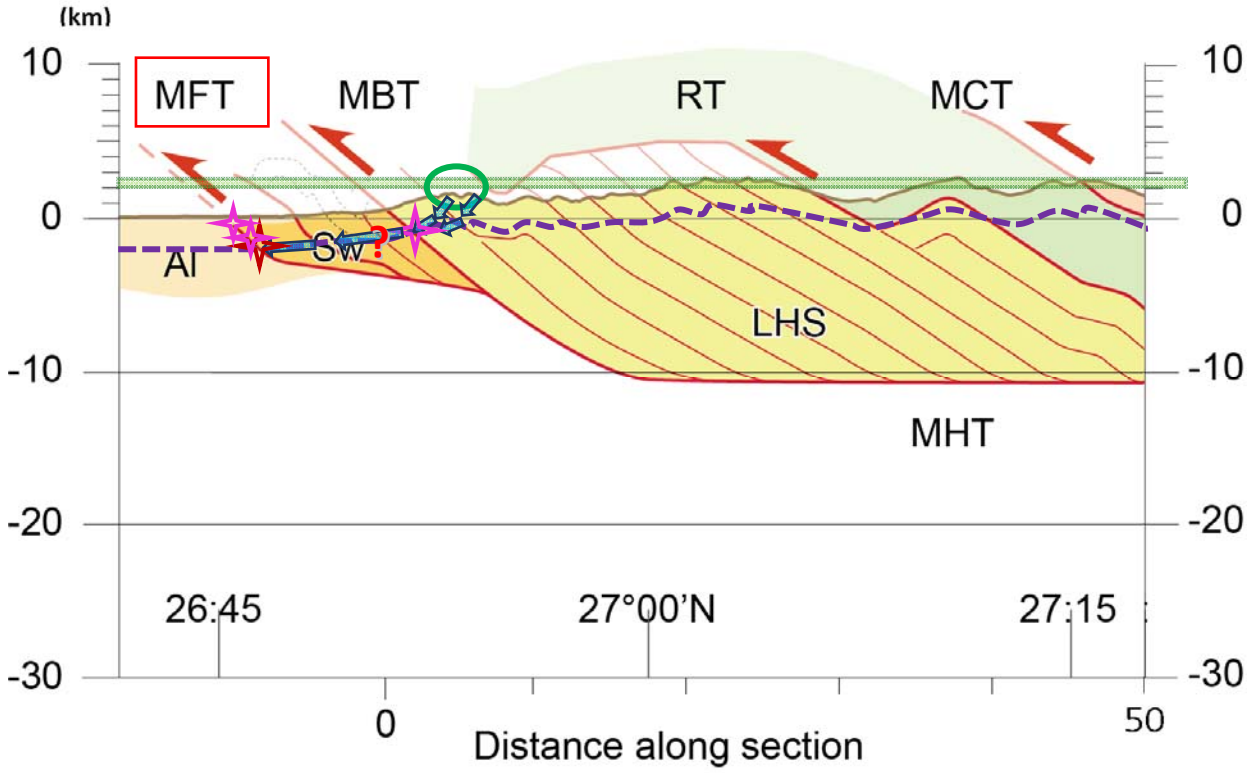

Figure 5.3 Schematic diagram showing the forming conditions of fault gouges along the MBT and MFT. (Modified on Long et al., 2011). Based on the temperature range of kaolinite geothermometer, the pink stars point out the locations where clay minerals have formed. The red star refers to the formation location of 89C based on the calculated temperature of smectite geothermometer. The transparent green stripe shows the elevation range of ~ 2 – 2.5 km while the purple curly dash line points out the maximum depth of ~ 2 km. The green ellipse symbol indicates the probably nearest location that the fluids were derived from. The blue arrows show the flow directions of the pervasive paleo-meteoric fluids and indicate the hypothetical paths of the meteoric waters towards the fault zones now exposed at the surface. MHT – Main Himalayan Thrust, MCT – Main Central Thrust, RT – Ramgarh Thrust, MBT – Main Boundary Thrust, MFT – Main Frontal Thrust, LHS – Lesser Himalayan Sequence, Sw – Siwaliks, and Al- Alluvium.

Chapter 6: Conclusion

6.1 Summary

The mineralogical, morphological, and geochemical data of 11 gouge samples from the major crustal faults in the eastern Bhutan show several conclusions:

1. From the mineralogical and morphological investigations, the fault gouges are clay dominant and contain two clay types: (a) 2:1 layers, involving smectite, illite-smectite, and illite; (b) 1:1 layers, kaolinite. Both illite and kaolinite present in all samples. In addition, mineral clasts mainly include mica, quartz, and chlorite.
2. These clay minerals have most likely formed in the fault gouge by interaction with the paleo-meteoric water during the movement of faults.
3. The presence of authigenic illite, as a K-bearing clay mineral, is crucial for dating fault.
4. For the three samples that have three grain size fractions analyzed (0.1μm, 0.4μm, &2μm), there is no evident relation between grain size and either $\delta^{18}O$ or δD isotopic composition.
5. Based on both smectite and kaolinite geothermometers, the equilibration temperature ranges of clay formation show two groups: (a) only the MFT sample 89C may have formed near surface at the lowest temperature, 35. 8 °C (± 1.6°C)$_{sm}$ and 20.6 °C (± 1.6°C)$_K$; (b) other samples yield the same result that they have formed within the equilibration depth of ~ 2 km with ~ 35 °C − 46.3 °C (± 1.6°C)$_K$ of other samples.
6. Comparing with corresponding data which show the relationship between water isotopic composition and sample elevation in the eastern Bhutan, the isotopic composition data of the waters with -10.6 − -9.0 ‰ $\delta^{18}O_{K\text{-}W}$ and -74.8 − -62.2‰ $\delta D_{K\text{-}W}$ suggest that the paleo-meteoric water was derived from elevations between 2000 and 2500 m, which are ~1500 – 2000 m higher than the outcrops of fault gouges.
7. By reconstructing the formation condition of fault gouges, it is deducted that the fault gouges along the MBT and MFT have formed in the equilibration depth of ~ 2 km and at ~ 3 km or longer horizontal distance from the site of the source of the paleo-meteoric waters. Besides, the meteoric waters penetrated, moved toward the clay formation sites by the horizontal hydrostatic pressure gradient, and were involved into fault gouge formation.

8. However, using the deduction for the MFT fault gouge, a series of questions is proposed about whether the meteoric waters can pass through the fault barriers, mainly the MBT, to the forming site of the MFT fault gouge, and how. If the answer is no, where is the meteoric waters derived from?

6.2 Further Research

Although this study achieved its overall aim, the interpretation of the stable isotopic compositions of clays from the MFT fault gouge requires further research, therefore, several further studies that could not be performed due to limited time and availability of instruments. Because the results of this study suggest that the K-bearing clays were formed in the fault gouge, the K-Ar dating of the samples will follow in the coming months. In addition, this study can contribute to related research, like how the fault zone in the eastern Bhutan links to other faults in the Himalaya orogeny. In brief, there are several further studies / research projects suggested:

1. The identification of both illite polytypes and quantitative mineralogical composition of the grain-size fractions is important not only for analyzing the processes of clay mineralogical aggregation, but for the reliable interpretation of the isotopic data. For example, if the coarse fraction is dominated by kaolinite and smaller fraction by smectite, the temperature differences would be more meaningful. Also, such precise identifications promote the analysis of the coexistence condition of smectite and illite in MFT samples 89, which may be useful for deducting the source of the meteoric waters involved into the clay formation in 89. To obtain these data, quantitative analysis is required, such as relatively advanced XRD analysis and illite crystallinity (Mancktelow et al., 2015; Huyghe et al., 2011).
2. To better characterize clay morphology and composition, the TEM connected with EDS system is more suitable for precise clay mineral identification.
3. Combining with δD isotopic data, the use of K/Ar dating technique provides the relation between restoration of the K-Ar system and interaction with the meteoric water introduced in fault gouges with apparent age on grain size (Mancktelow et al., 2015). Therefore, it is crucial to further analyze the interactions of brittle faulting and the influence of the meteoric water influx on apparent K-Ar ages (Mancktelow et al., 2015).

4. Siwalik sample 81A is from Sikkim. All the data for this sample and the contrast with other samples taken in the eastern Bhutan will be useful to the study along strike variations of faulting mechanisms and ages. This difference suggest that several sections of a same structure ought to be studied in order to reliably interpret the ages from one site in the context of the entire orogen. The more the sample data are collected, the more reliable the interpretation to restore the deformation evolution within the Himalayas.

References

Anczkiewicz, R., Chakraborty, S., Dasgupta, S., Mukhopadhyay, D. and Kołtonik, K., 2014. Timing, duration and inversion of prograde Barrovian metamorphism constrained by high resolution Lu–Hf garnet dating: A case study from the Sikkim Himalaya, NE India. Earth and Planetary Science Letters, 407, pp.70-81.

Atomic World. Basic Principle of Transmission Electron Microscope [online]. Available from http://www.hk-phy.org/atomic_world/tem/tem02_e.html [cited 22 January 2017].

Avouac, J.P., 2015. Mountain Building: From earthquakes to geological deformation. In Treatise on Geophysics (Vol. 6, pp. 381-432).

Bauer, K.K., Vennemann, T.W., 2014. Analytical methods for the measurement of hydrogen isotope composition and water content in clay minerals by TC/EA. Chemical Geology 363, 229-240.

Buatier, M.D., Chauvet, A., Kanitpanyacharoen, W., Wenk, H.R., Ritz, J.F. and Jolivet, M., 2012. Origin and behavior of clay minerals in the Bogd fault gouge, Mongolia. Journal of Structural Geology, 34, pp.77-90.

Bhattacharyya, K. and Mitra, G., 2009. A new kinematic evolutionary model for the growth of a duplex—an example from the Rangit duplex, Sikkim Himalaya, India. Gondwana Research, 16(3), pp.697-715.

Bilham, R., Gaur, V.K. and Molnar, P., 2001. Himalayan seismic hazard. Science, 293(5534), pp.1442-1444.

Blisniuk, P.M., Stern, L.A., 2005. Stable isotope paleoaltimetry: a critical review. American Journal of Science 305, 1033-1074.

Buatier, M.D., Chauvet, A., Kanitpanyacharoen, W., Wenk, H.R., Ritz, J.F. and Jolivet, M., 2012. Origin and behavior of clay minerals in the Bogd fault gouge, Mongolia. Journal of Structural Geology, 34, pp.77-90.

Choo, C.O. and Chang, T.W., 2000. Characteristics of clay minerals in gouges of the Dongrae fault, Southeastern Korea, and implications for fault activity. Clays and clay minerals, 48(2), pp.204-212.

Concept Web Alliance, 2010. X-ray crystallography [online]. Available from http://wikidraft.referata.com/wiki/X-ray_crystallography [cited 15 January 2017].

Coutand, I., Barrier, L., Govin, G., Grujic, D., Hoorn, C., Dupont-Nivet, G. and Najman, Y., 2016. Late Miocene-Pleistocene evolution of India-Eurasia convergence partitioning between the Bhutan Himalaya and the Shillong plateau: New evidences from foreland basin deposits along the Dungsam Chu section, Eastern Bhutan. Tectonics.

Coutand, I., Whipp, D.M., Grujic, D., Bernet, M., Fellin, M.G., Bookhagen, B., Landry, K.R., Ghalley, S.K. and Duncan, C., 2014. Geometry and kinematics of the Main Himalayan Thrust and Neogene crustal exhumation in the Bhutanese Himalaya derived from inversion of multithermochronologic data. Journal of Geophysical Research: Solid Earth, 119(2), pp.1446-1481.

Delgado, A. and Reyes, E., 1996. Oxygen and hydrogen isotope compositions in clay minerals: A potential single-mineral geothermometer. Geochimica et cosmochimica acta, 60(21), pp.4285-4289.

Dill, H.G., Kus, J., Dohrmann, R. and Tsoy, Y., 2008. Supergene and hypogene alteration in the dual-use kaolin-bearing coal deposit Angren, SE Uzbekistan. International journal of coal geology, 75(4), pp.225-240.

Fowler, A.C. and Yang, X.S., 2003. Dissolution/precipitation mechanisms for diagenesis in sedimentary basins. Journal of Geophysical Research: Solid Earth, 108(B10).

Gansser, A., 1983. Geology of the Bhutan Himalaya. Birkhauser Verlag, Basel, 1983, 181 pp.

Gard, J.A. ed., 1971. The electron-optical investigation of clays (Vol. 3). Mineralogical Society (Clay Minerals Group).

Gehrels, G.E., DeCelles, P.G., Martin, A., Ojha, T.P., Pinhassi, G. and Upreti, B.N., 2003. Initiation of the Himalayan orogen as an early Paleozoic thin-skinned thrust belt. GSA today, 13(9), pp.4-9.

Gharrabi, M., Velde, B. and Sagon, J.P., 1998. The transformation of illite to muscovite in pelitic rocks: Constraints from X-ray diffraction. Clays and Clay Minerals, 46(1), pp.79-88.

Gharrabi, M., Velde, B. and Sagon, J.P., 1998. The transformation of illite to muscovite in pelitic rocks: Constraints from X-ray diffraction. Clays and Clay Minerals, 46(1), pp.79-88.

Grujic, D., Coutand, I., Doon, M. and Kellett, D.A., 2017. Northern provenance of the Gondwana Formation in the Lesser Himalayan Sequence: constraints from 40Ar/39Ar dating of detrital muscovite in Darjeeling-Sikkim Himalaya. Italian Journal of Geosciences, 136(1), pp.15-27.

Grujic, D., Cowan, B., Hren, M. T., Coutand, I., Barrier, L. and Govin, G. (in review) Formation of a rain shadow: O and H stable isotope records in authigenic clays from the Siwalik Group in eastern Bhutan. Earth and Planetary Science Letters.

Grujic, D., Hollister, L.S. and Parrish, R.R., 2002. Himalayan metamorphic sequence as an orogenic channel: insight from Bhutan. Earth and Planetary Science Letters, 198(1), pp.177-191.

Grujic, D., Warren, C.J. and Wooden, J.L., 2011. Rapid synconvergent exhumation of Miocene-aged lower orogenic crust in the eastern Himalaya. Lithosphere, 3(5), pp.346-366.

Haines, S., Lynch, E., Mulch, A., Valley, J.W. and van der Pluijm, B., 2016. Meteoric fluid infiltration in crustal-scale normal fault systems as indicated by δ18O and δ2H geochemistry and 40Ar/39Ar dating of neoformed clays in brittle fault rocks. Lithosphere, 8(6), pp.587-600.

Haines, S.H. and Van Der Pluijm, B.A., 2008. Clay quantification and Ar–Ar dating of synthetic and natural gouge: application to the Miocene Sierra Mazatán detachment fault, Sonora, Mexico. Journal of Structural Geology, 30(4), pp.525-538.

Hirschmiller, J., Grujic, D., Bookhagen, B., Coutand, I., Huyghe, P., Mugnier, J.L. and Ojha, T., 2014. What controls the growth of the Himalayan foreland fold-and-thrust belt?. Geology, 42(3), pp.247-250.

Hodges, K.V., 2000. Tectonics of the Himalaya and southern Tibet from two perspectives. Geological Society of America Bulletin, 112(3), pp.324-350.

Hoefs, J., 2015. Isotope fractionation processes of selected elements. In Stable Isotope Geochemistry (pp. 47-190). Springer International Publishing.

Huang, W.L., Bishop, A.M. and Brown, R.W., 1986. The effect of fluid/rock ratio on feldspar dissolution and illite formation under reservoir conditions. Clay Minerals, 21(4), pp.585-601.

Huyghe, P., Guilbaud, R., Bernet, M., Galy, A. and Gajurel, A.P., 2011. Significance of the clay mineral distribution in fluvial sediments of the Neogene to Recent Himalayan Foreland Basin (west-central Nepal). Basin Research, 23(3), pp.332-345.

Jouanne, F., Mugnier, J.L., Gamond, J.F., Le Fort, P., Pandey, M.R., Bollinger, L., Flouzat, M. and Avouac, J.P., 2004. Current shortening across the Himalayas of Nepal. Geophysical Journal International, 157(1), pp.1-14.

Kellett, D.A. and Grujic, D., 2012. New insight into the South Tibetan detachment system: Not a single progressive deformation. Tectonics, 31(2).

Kellett, D.A., Grujic, D. and Erdmann, S., 2009. Miocene structural reorganization of the South Tibetan detachment, eastern Himalaya: Implications for continental collision. Lithosphere, 1(5), pp.259-281.

Landry, K.R., Coutand, I., Whipp, D.M., Grujic, D. and Hourigan, J.K., 2016. Late Neogene tectonically driven crustal exhumation of the Sikkim Himalaya: Insights from inversion of multithermochronologic data. Tectonics, 35(3), pp.831-857.

Le Fort, P., 1975. Himalayas: the collided range. Present knowledge of the continental arc. American Journal of Science, 275(1), pp.1-44.

Long, S., McQuarrie, N., Tobgay, T. and Grujic, D., 2011. Geometry and crustal shortening of the Himalayan fold-thrust belt, eastern and central Bhutan. Geological Society of America Bulletin, pp.B30203-1.

Mancktelow, N., Zwingmann, H., Campani, M., Fügenschuh, B. and Mulch, A., 2015. Timing and conditions of brittle faulting on the Silltal-Brenner fault zone, Eastern Alps (Austria). Swiss Journal of Geosciences, 108(2-3), pp.305-326.

McQuarrie, N., Long, S.P., Tobgay, T., Nesbit, J.N., Gehrels, G. and Ducea, M.N., 2013. Documenting basin scale, geometry and provenance through detrital geochemical data: Lessons from the Neoproterozoic to Ordovician Lesser, Greater, and Tethyan Himalayan strata of Bhutan. Gondwana Research, 23(4), pp.1491-1510.

McQuarrie, N., Robinson, D., Long, S., Tobgay, T., Grujic, D., Gehrels, G. and Ducea, M., 2008. Preliminary stratigraphic and structural architecture of Bhutan: Implications for the along strike architecture of the Himalayan system. Earth and Planetary Science Letters, 272(1), pp.105-117.

McQuarrie, N., Tobgay, T., Long, S.P., Reiners, P.W. and Cosca, M.A., 2014. Variable exhumation rates and variable displacement rates: Documenting recent slowing of Himalayan shortening in western Bhutan. Earth and Planetary Science Letters, 386, pp.161-174.

Meigs, A.J., Burbank, D.W. and Beck, R.A., 1995. Middle-late Miocene (> 10 Ma) formation of the Main Boundary thrust in the western Himalaya. Geology, 23(5), pp.423-426.,

Mishra, O.P., 2014. Intricacies of the Himalayan seismotectonics and seismogenesis: need for integrated research. Current Science, 106(2), pp.176-187.

Mitra, G., K. Bhattacharyya, and M. Mukul (2010), The Lesser Himalayan duplex in Sikkim: Implications for variations in Himalayan shortening, J. Geol. Soc. India, 75(1), 289–301.

Mix, H.T., Ibarra, D.E., Mulch, A., Graham, S.A., Chamberlain, C.P., 2016. A hot and high Eocene Sierra Nevada. Geological Society of America Bulletin 128, 531-542.

Moore, D.M. and Reynolds, R.C., 1997. X-Ray Diffraction and the Identification and Analysis of Clay Minerals. Oxford University Press, Inc., Oxford, New York.

Mottram, C.M., Argles, T.W., Harris, N.B.W., Parrish, R.R., Horstwood, M.S.A., Warren, C.J. and Gupta, S., 2014. Tectonic interleaving along the Main Central Thrust, Sikkim Himalaya. Journal of the Geological Society, 171(2), pp.255-268.

Mottram, C.M., Parrish, R.R., Regis, D., Warren, C.J., Argles, T.W., Harris, N.B. and Roberts, N.M., 2015. Using U-Th-Pb petrochronology to determine rates of ductile thrusting: Time windows into the Main Central Thrust, Sikkim Himalaya. Tectonics, 34(7), pp.1355-1374.

Mukul, M. (2010), First-order kinematics of wedge-scale active Himalayan deformation: Insights from the Darjiling-Sikkim-Tibet (DaSiT) wedge, J. Asian Earth Sci., 39, 645–657.

Najman, Y., Appel, E., Boudagher‐Fadel, M., Bown, P., Carter, A., Garzanti, E., Godin, L., Han, J., Liebke, U., Oliver, G. and Parrish, R., 2010. Timing of India‐Asia collision: Geological, biostratigraphic, and palaeomagnetic constraints. Journal of Geophysical Research: Solid Earth, 115(B12).

Nelson, K.D., Zhao, W., Brown, L.D. and Kuo, J., 1996. Partially molten middle crust beneath southern Tibet: synthesis of project INDEPTH results. Science, 274(5293), p.1684.

Nesse, W.D., 2000. Introduction to Mineralogy. *In* Introduction to X-ray Crystallography. Oxford University Press, Inc., Oxford, New York. pp. 184-193.

Pevear, D.R., 1999. Illite and hydrocarbon exploration. Proceedings of the National Academy of Sciences, 96(7), pp.3440-3446.

Portenga, E.W., Bierman, P.R., Duncan, C., Corbett, L.B., Kehrwald, N.M. and Rood, D.H., 2015. Erosion rates of the Bhutanese Himalaya determined using in situ-produced 10 Be. Geomorphology, 233, pp.112-126.

Purdue University, 2014. Scanning Electron Microscope [online]. Available from https://www.purdue.edu/ehps/rem/rs/sem.htm#3 [cited 20 January 2017].

Rensselaer Polytechnic Institute. The Electron Microprobe Method [online]. Available from http://ees2.geo.rpi.edu/probe/Images/concepts/concept2.html [cited 15 January 2017].

Robinson, D.M. and McQuarrie, N., 2012. Pulsed deformation and variable slip rates within the central Himalayan thrust belt. Lithosphere, 4(5), pp.449-464.

Rozanski, K., Araguás–Araguás, L., Gonfiantini, R., 1993. Isotopic patterns in modern global precipitation. Climate change in continental isotopic records 78, 1-36.

Rumble, D.I., Hoering, T.C., 1994. Analysis of oxygen and sulfur isotope ratios in oxide and sulfide minerals by spot heating with a carbon dioxide laser in a fluorine atmosphrere. Accounts of Chemical Research 27, 237-241.

Searle, M.P., Law, R.D., Godin, L., Larson, K.P., Streule, M.J., Cottle, J.M. and Jessup, M.J., 2008. Defining the Himalayan main central thrust in Nepal. Journal of the Geological Society, 165(2), pp.523-534.

Sheppard, S.M.F. and Gilg, H.A., 1996. Stable isotope geochemistry of clay minerals. Clay Minerals, 31(1), pp.1-24.

Stevens, V.L. and Avouac, J.P., 2016. Millenary Mw> 9.0 earthquakes required by geodetic strain in the Himalaya. Geophysical Research Letters, 43(3), pp.1118-1123.

Tobgay, T., McQuarrie, N., Long, S., Kohn, M.J. and Corrie, S.L., 2012. The age and rate of displacement along the Main Central Thrust in the western Bhutan Himalaya. Earth and Planetary Science Letters, 319, pp.146-158.

Van der Beek, P., Robert, X., Mugnier, J.-L., Bernet, M., Huyghe, P., and Labrin, E., 2006, Late Miocene– Recent exhumation of the central Himalaya and recycling in the foreland basin assessed by apatite fission-track thermochronology of Siwalik sedi- ments, Nepal: Basin Research, v. 18, p. 413–434, doi:10.1111/j.1365-2117.2006.00305.x.

Vennemann, T.W., O'Neil, J.R., 1993. A simple and inexpensive method of hydrogen isotope and water analyses of minerals and rocks based on zinc reagent. Chemical Geology 103, 227–234.

Vrolijk, P. and van der Pluijm, B.A., 1999. Clay gouge. Journal of Structural Geology, 21(8), pp.1039-1048.

Welton, J.E., 2004. SEM Petrology Atlas. The American Association of Petroleum Geologists, Tulsa, Oklahoma, U.S.A..

Whipp, D.M. and Ehlers, T.A., 2007. Influence of groundwater flow on thermochronometer-derived exhumation rates in the central Nepalese Himalaya. Geology, 35(9), pp.851-854.

Yan, Y., van der Pluijm, B.A. and Peacor, D.R., 2001. Deformation microfabrics of clay gouge, Lewis Thrust, Canada: a case for fault weakening from clay transformation. Geological Society, London, Special Publications, 186(1), pp.103-112.

Yin, A., 2006. Cenozoic tectonic evolution of the Himalayan orogen as constrained by along-strike variation of structural geometry, exhumation history, and foreland sedimentation. Earth-Science Reviews, 76(1), pp.1-131.

Yin, A., Dubey, C.S., Kelty, T.K., Webb, A.A.G., Harrison, T.M., Chou, C.Y. and Célérier, J., 2009. Geologic correlation of the Himalayan orogen and Indian craton: Part 2. Structural geology, geochronology, and tectonic evolution of the Eastern Himalaya. Geological Society of America Bulletin, pp.B26461-1.

Yin, A. and Harrison, T.M., 2000. Geologic evolution of the Himalayan-Tibetan orogen. Annual Review of Earth and Planetary Sciences, 28(1), pp.211-280.

Appendix A: Petrography

BH86B, C: Graywacke/Diamictite, Diuri Formation, Bangtar, Bhutan

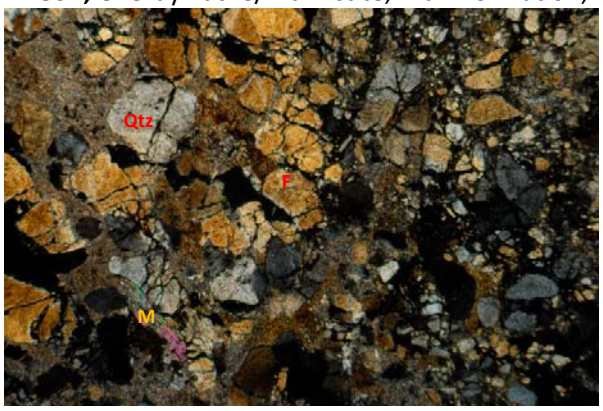

5 mm (XPL) 86B_FW

Mineralogy:

- Quartz-rich; muscovite; clays; feldspar.
- Monocrystalline and polycrystalline quartz.

Texture:

- Coarse grain size: 0.1 – 1 mm;
- Sub-rounded and broken grains;
- Matrix: ~ 15 – 20 %.

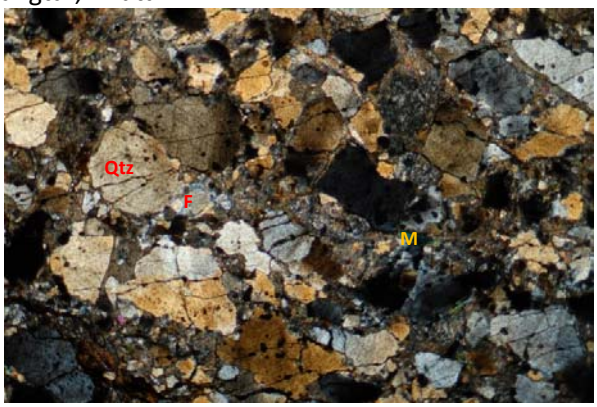

5 mm (XPL) 86C_HW

Mineralogy:

- Quartz-rich; muscovite; clays; feldspar.

Texture:

- Coarse grain size: 0.1 – 1.5 mm;
- Sub-rounded and broken grains;
- Altered rim in feldspar;
- Matrix: ~ 15 – 20 %.

2.5 mm (XPL) 86B_FW

Mineral:
Brightly colored illite cement around potassium feldspars.

2.5 mm (XPL) 86C_HW

Texture: Altered rim in feldspar

BH97D: Graywacke, Gondwana-Siwaliks contact, MBT, Deothang coal mine, Bhutan

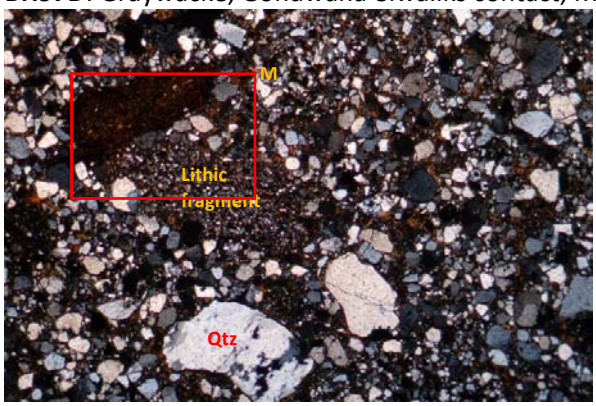

5 mm (XPL) 97D_FW

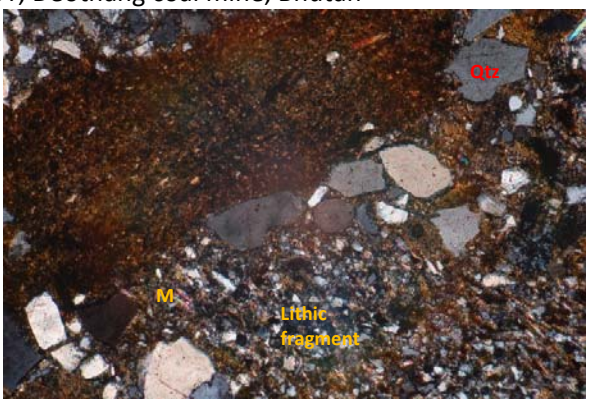

2.5 mm (XPL) 97D_FW

Enlargement of the red rectangle area in the left micrograph

Mineralogy:

- Quartz-rich; muscovite; clays; lithic fragments
- Monocrystalline and polycrystalline quartz;

Texture:

- Coarse grain size: 0.1 – 2.5 mm;
- Lithic fragment: ~ 3.5 mm; silt reworking grains;
- Sub-rounded and broken grains;
- Matrix: ~ 15 %.

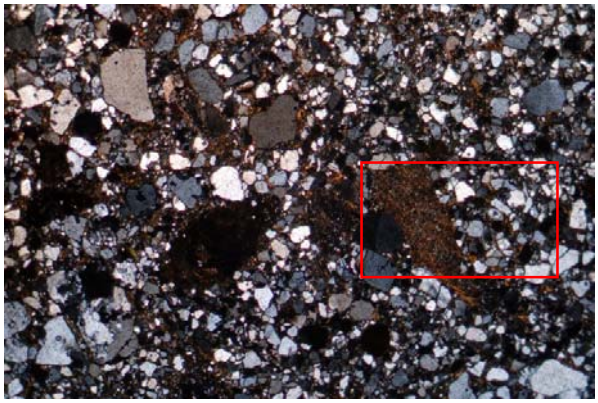

5 mm (XPL) 97D_FW

2.5 mm (XPL) 97D_FW

Enlargement of the red rectangle area in the left micrograph
Texture: Altered feldspar

BH98D, CI, CII: Graywacke, Gondwana-Siwaliks contact, MBT, Deothang coal mine, Bhutan

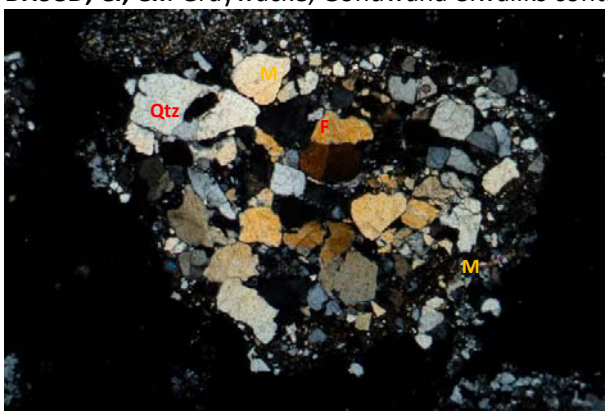

5 mm (XPL) 98D_FW

Mineralogy:

- Quartz-rich; muscovite; clays; lithic fragments;
- Monocrystalline and polycrystalline quartz;

Texture:

- Coarse grain size: 0.1 – 2 mm;
- Lithic fragment: silt reworking grains; (bottom view)
- Sub-rounded and broken grains;
- Matrix: ~ 15 %.

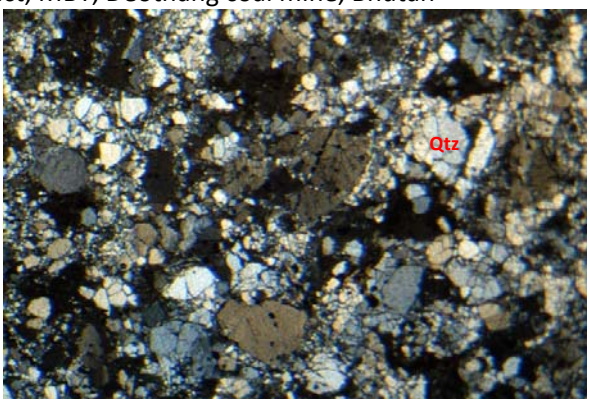

5 mm (XPL) 98CI_HW

Mineralogy:

- Quartz-rich; muscovite; clays; lithic fragments;
- Monocrystalline and polycrystalline quartz;

Texture:

- Coarse grain size: 0.1 – 1.5 mm;
- Sub-rounded and badly broken grains.

2.5 mm (XPL) 98D_FW

5 mm (XPL) 98CII_HW

Gondwana Coal

BH182A, C: Sandstone, Siwalik Group, Dogar - Panbang, Bhutan

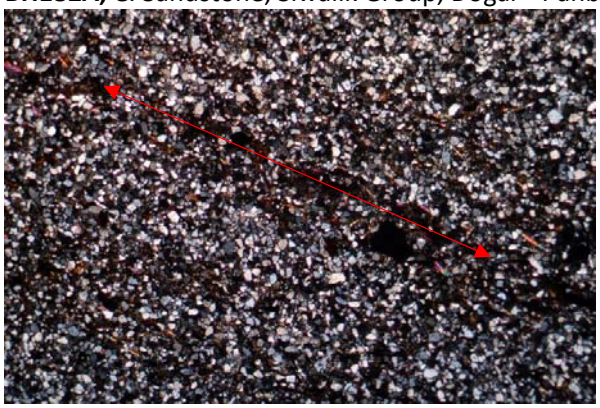

5 mm (XPL) 182A_FW

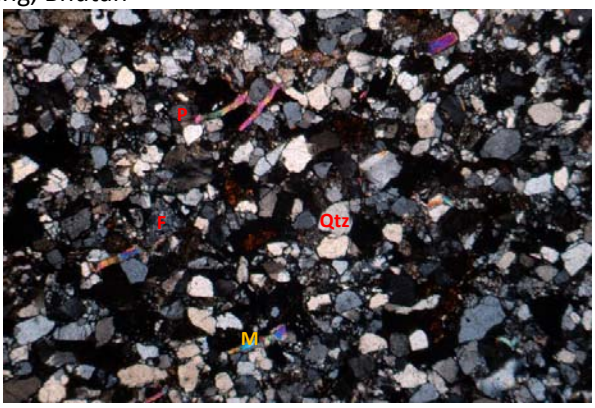

5 mm (XPL) 182C_HW

Mineralogy:

- Quartz-rich; muscovite; clays; feldspar.
- Monocrystalline and polycrystalline quartz.

Texture:

- fine grain size: very fine, up to 0.2 mm;
- Sub-rounded grains; well-sorted;
- Matrix: < 10 %;
- Lamination by the alignment of mica minerals.

Mineralogy:

- Quartz-rich; muscovite; clays; feldspar; plagioclase.
- Monocrystalline and polycrystalline quartz.

Texture:

- Coarse grain size: up to 1 mm;
- Sub-rounded and broken grains;
- Altered rim in feldspar;
- Matrix: ~ 5%.

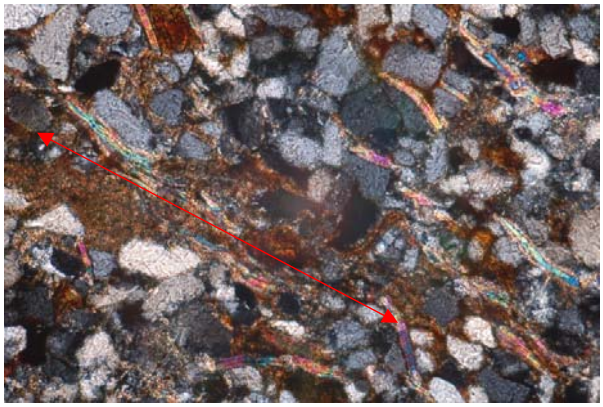

1.1 mm (XPL) 182A_FW

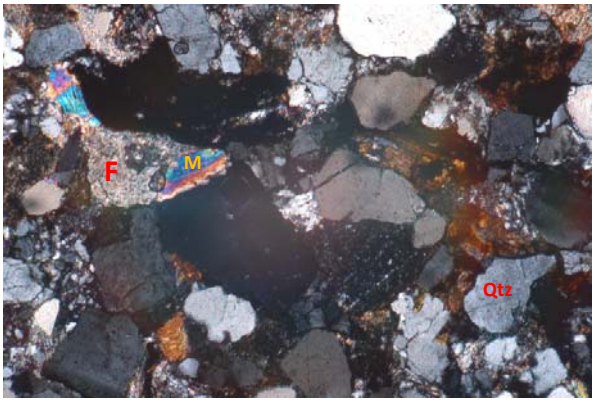

2.5 mm (XPL) 182C_HW

Texture: Altered rim in feldspar

BH89D, A: Alluvial Sandstone, MFT, Daranga Mella, S.Jongkhar, Bhutan

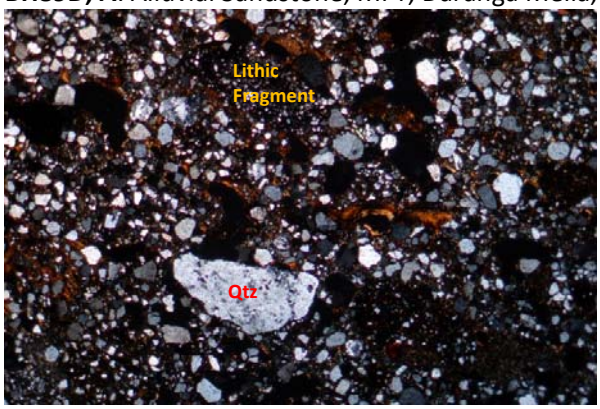

5 mm (XPL) 89D_FW

Mineralogy:

- Quartz-rich; muscovite; clays; feldspar; lithic fragments;
- Monocrystalline and polycrystalline quartz;

Texture:

- Coarse grain size: 0.1 – 2.5 mm;
- Lithic fragment;
- Sub-rounded grains;
- Matrix: ~ 10%.

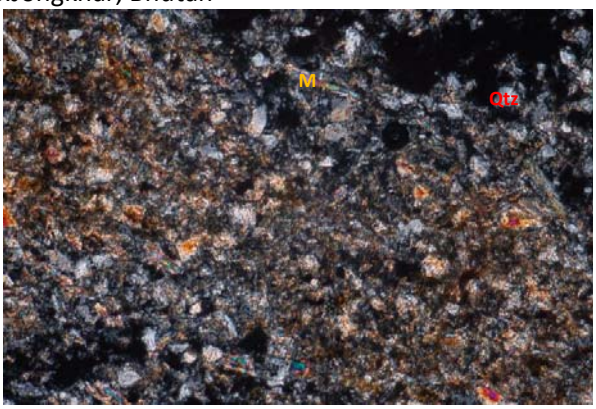

1.1 mm (XPL) 89A_HW

Mineralogy:

- Quartz and muscovite dominant; clays;

Texture:

- fine grain size: up to 0.2 mm;
- Sub-rounded grains.

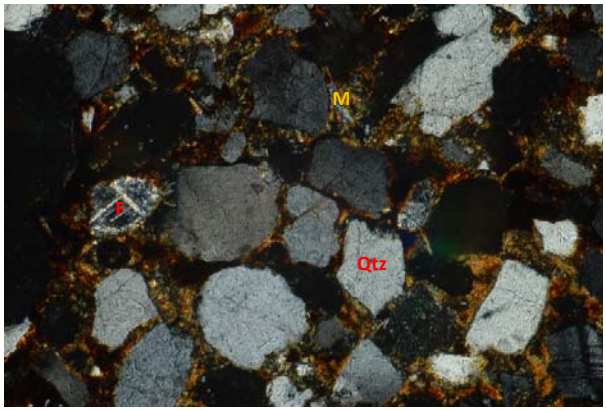

1.1 mm (XPL) 89D_FW

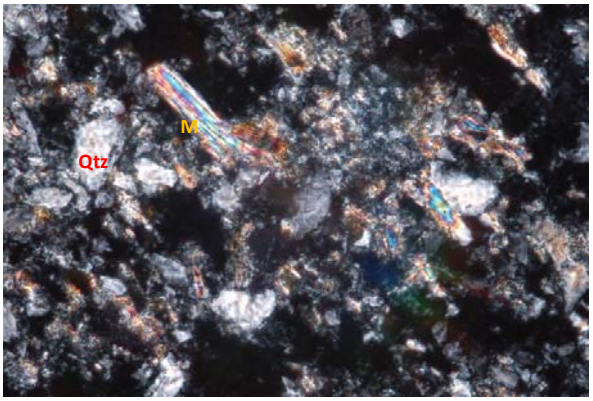

0.35 mm (XPL) 89A_HW

Reference: Sikkim

SK81B, C: Graywacke, Siwalik Group, Coronation Bridge, Sikkim

5 mm (XPL) 81B_FW

Mineralogy:

- Quartz-rich; muscovite; clays; feldspar.
- Monocrystalline and polycrystalline quartz.

Texture:

- Coarse grain size: up to 1 mm;
- Sub-rounded grains; well-sorted;
- Matrix: ~ 15 %, see micrograph below.

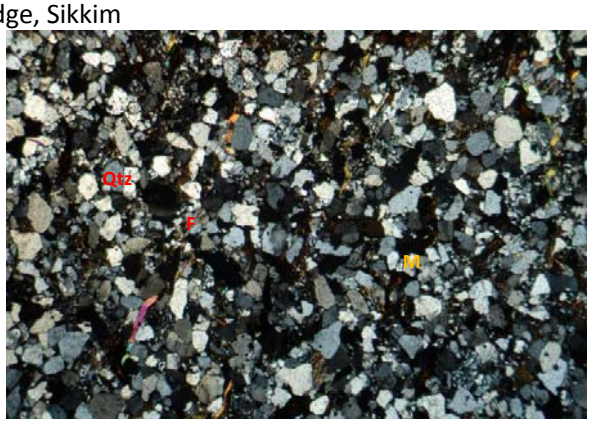

5 mm (XPL) 81C_HW

Mineralogy:

- Quartz-rich; muscovite; clays; feldspar.

Texture:

- Coarse grain size: up to 1 mm;
- Sub-rounded and broken grains;
- Altered rim in feldspar;
- Matrix: ~ 10 %.

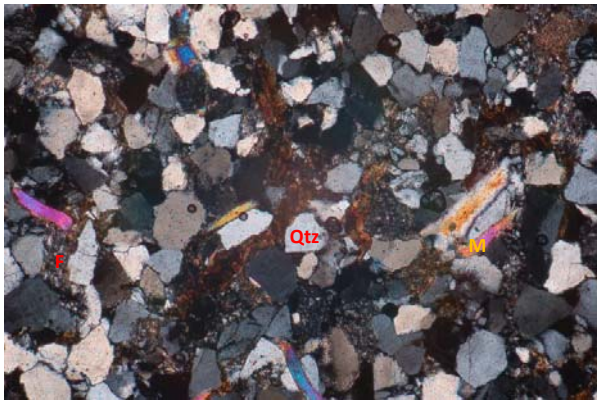

2.5 mm (XPL) 81B_FW

Texture: Altered rim in feldspar

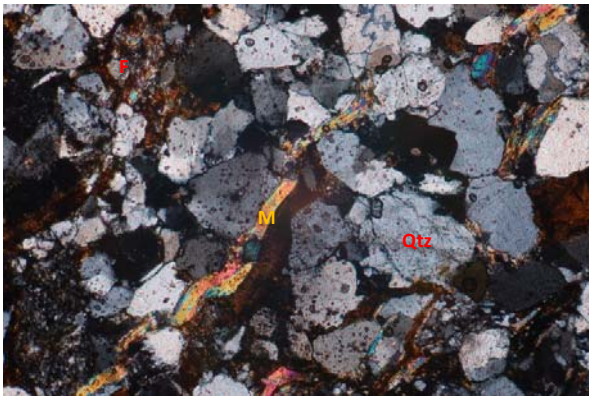

2.5 mm (XPL) 81C_HW

Texture: Altered rim in feldspar

Appendix B: Sample Preparation

B.1 Physical Pretreatment

B.1.1 Soaking and Blending

Aims: - to suspend clay minerals by first soaking the samples overnight and secondly using a laboratory blender and an ultrasonic bath, in order to further separate fine-grained aggregates to prepare for next treatments.

Equipment Required:

- Crushed Samples
- Scoopula
- Deionized Water
- Permanent Marker
- 1000mL Beakers
- Stirring Rods
- Glass Dishes
- Waring Industrial Blender
- Ultrasonic Bath

Procedure:
Before and after using any equipment, clean it by cleaning soap first and then acid alcohol.

1. Add 200 g crushed sample to labelled 1000 mL beaker with deionized water, up to 1000 mL;

2. Stir the sample by using stirring rod, so that the sample can somehow be in suspension;

3. Wash the particles attached on the rod back into the beaker using spray bottle;

4. Use a glass dish to cover the beaker and leave the sample to soak overnight (Figure B.1);

Figure B.1 Soaking crushed sample overnight

5. After soaking, stir the sample into suspension and pour them into the Waring Industrial Blender (Figure B.2);

6. Blend the sample at full power for about 3 minutes;

7. Pour the sample back into the beaker once it is totally in suspension;

8. Use spray bottle to wash the particles attached on the sides and bottom of the blender back into the beaker;

9. Use ultrasonic bath to separate fine-grained aggregates.

Then, the sample is ready for clay separation.

Figure B.2 Waring Industrial Blender

Note: The method is useful for sticky clay samples. So we used this method only for the 89 series samples.

B.2 Chemical Pretreatment

B.2.1 Acetic Acid Treatment for Carbonate Removal

Aims: - to test which crushed clay samples are rich in carbonates by adding a certain amount of acetic acid and to remove carbonates from the effervescing samples.

Safety Equipment:

- Lab Coat
- Safety Glasses
- Gloves
- Fume Hood

Equipment Required:

- Crushed Samples
- Deionized Water
- Glacial Acetic Acid
- Permanent Marker
- 30 mL Beakers
- 200 mL Beaker
- Graduated Cylinder
- Dropper Pipette
- Stirring Rods
- 50mL Conical Centrifuge Tubes
- Centrifuge

Procedure:

Note: Please always wear safety equipment with handling any chemicals and do chemical treatment in a fume hood.

Before and after using any equipment, clean it by cleaning soap first and then acid alcohol.

1. Test Carbonates

1) Put little sample for each into corresponding labelled 30 mL beaker;

2) Drop acetic acid into beakers by using dropper pipette;

3) Observe if any reaction occurs.

For the sample which appears effervescing, follow next steps to remove carbonates.

2. Removal of Carbonates

1) Prepare the mixture of acetic acid and deionized water by a ratio 1:4 within a fume hood: use graduated cylinder to measure them and pour them into a 200 mL beaker, followed by stirring the mixture; for example, 160 mL deionized water and 40 mL acetic acid are added into the mixture beaker.

2) Put 10 mL sample into a labelled 50 mL tube for each;

3) Measure 40 mL of the mixture and add them in the tube for each sample;

4) Leave the samples in the fume hood for more than half an hour and stir them again;

5) Once the samples stop effervescing, stir them well;

6) Centrifuge the samples at 4100 rpm for 3 minutes;

7) Decant the supernatant into an acetic acid waste beaker for disposal;

8) Fill up the sample tubes with deionized water to rinse out the sample and centrifuge them again;

9) Repeat 6) – 8) at least 5 times until the samples get cleaned.

B.2.2 Bleach Treatment for the Removal of Organic Materials

Aims: - to remove organic matters from samples to avoid their effects on X-ray diffraction analysis.

Safety Equipment:

- Lab Coat
- Safety Glasses
- Gloves
- Fume Hood

Equipment Required:

- Crushed Samples
- Deionized Water
- Sodium Hypochlorite (NaOCl)
- 0.5 M Hydrochloric Acid (HCl)
- Permanent Marker
- 500 mL Beaker
- Graduated Cylinder
- StableTemp Ceramic Hot Plate
- Glass Pot
- 50mL Conical Centrifuge Tubes
- Centrifuge

Procedure:

Note: Please always wear safety equipment with handling any chemicals and do chemical treatment in a fume hood.

Before and after using any equipment, clean it by cleaning soap first and then acid alcohol.

1. Dilute bleach (NaOCl) with very small amount of 0.5M HCl to adjust pH value to 9.5 (bluish green on litmus paper): ~ 40 mL of 0.5 M HCl into ~ 400 mL bleach in a 500 mL beaker, measured by graduated cylinder(Figure B.3);

2. Put 5 mL sample into a labelled 50 mL tube for each;

3. Measure 10 mL bleach dilution and add them in the tube for each sample;

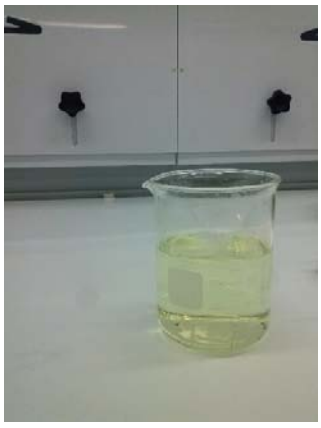

Figure B.3 Bleach Dilution

4. Shake the tubes for a while, turn on StableTemp Ceramic Hot Plate with the setting of 100 °C, and put a glass pot with water on the heating plate;

5. Heat the mixtures in the boiling-water pot for around 15 minutes and observe any change (Figure B.4);

6. Centrifuge the mixtures at 4100 rpm for 3 minutes and observe any change;

7. Decant the supernatant into a bleach waste beaker for disposal;

8. Repeat bleach steps 3 to 7 until organic material is sufficiently removed, that is shown by the evidence of a change in sample color from dark to white, gray, or red (Figure B.5);

Figure B.4 Heating the mixtures in the boiling-water pot at 100 °C

9. Fill up the sample tubes with deionized water to rinse out the sample and centrifuge them;

10. Decant the supernatant into a bleach waste beaker for disposal;

11. Repeat 9 and 10 at least 5 times until the samples get cleaned.

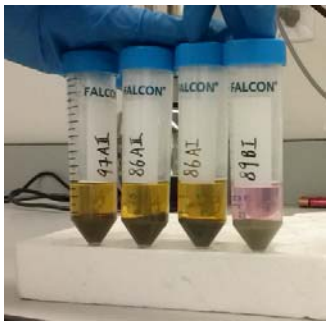

Figure B.5 The samples after heating and centrifuging once

Note: It is unnecessary to do chemical pretreatments for all samples. So the first step is testing carbonates and preliminarily identifying if organic matters are included or not by color. Generally, the presence of organic matters in the sample makes the sample color black.

B.3 Clay Separation

Aims: - to separate crushed clay samples into clay-size fractions of 2μm, 0.4μm, and 0.1μm.

Equipment Required:

- Crushed Samples
- Deionized Water
- Permanent Marker
- 500mL Beakers
- Stirring Rods
- Glass Dishes
- Plastic Water Pipe
- Dropper Pipette
- Evaporating Dishes
- Oven
- 50mL Conical Centrifuge Tubes
- Centrifuge
- Ultrasonic Bath

Procedure:

Before and after use any equipment, clean it by using cleaning soap first and then acid alcohol.

1. Gravity Settling for > 2μm

1) Add 100 g crushed sample to labelled 500 mL beaker with deionized water, up to 500 mL;

2) Stir the sample by using stirring rod, so that the sample can be in suspension;

3) Place the sample beaker in the ultrasonic bath to separate any flocculating particles for about 5 minutes;

4) Sit for about 3 hours 50 minutes to separate the sample into particle diameter of greater than 2μm (Figure B.6);

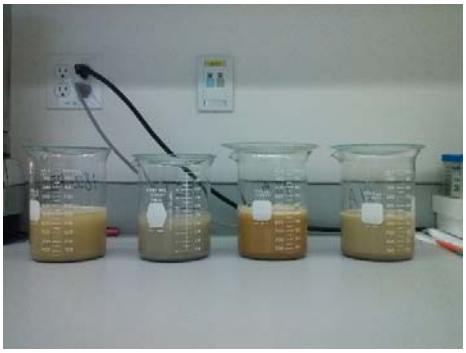

Figure B.6 Gravity Settling

Note: Use equation 3.2 to get gravity settling time. In this case, $T = 20\ ^{\circ}C$, $\eta = 0.001005$ Pa·s, $h = 0.05$ m, $D = 0.000002$ m, $d_p = 2650$ kg/m^3, $d_l = 1000$ kg/m^3, and $g = 9.807$ m/s^2, so $t = 13974.25$ s, then $t = 3.88$ hrs, which is about 3 hours 50 minutes.

5) Remove supernatant liquid by using plastic water pipe, or very gently decant the liquid to another 500mL beaker labelled with the sample name and '≤ 2μm' (Figure B.7);

6) Put all the sediment (> 2μm) in an evaporating dish labelled with the sample number and '> 2μm 'by using deionized water;

7) Put the evaporating dish in the oven at a temperature below 60 ˚C.

Figure B.7 Equipment of removing supernatant

2. Centrifuging to separate < 2μm matters

1) Add the supernatant liquid from gravity settling to labelled 50 mL conical centrifuge tubes (Figure B.8 a));

2) Centrifuge them at 2500 rpm for 45 seconds (Similar to Figure B.8 b));

Note: Use equation 3.3 to get settling time of a specific centrifuge for sedimentation of particles. Since 1 rev/s = 1 rpm/60, settling times for each centrifuge in this case are listed with specific parameters in Table B.1.

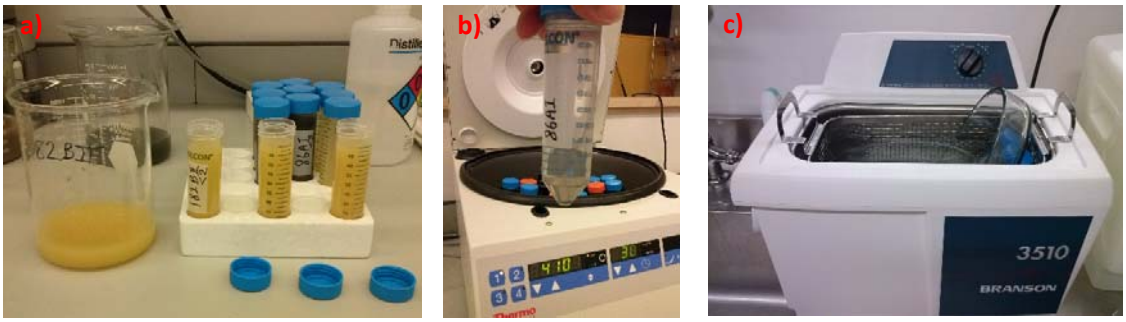

Figure B.8 a) Adding supernatant to labelled 50 mL tubes; **b)** After centrifuge at 4100 rpm for 30 minutes; **c)** Using Ultrasonic Bath to amalgomate ~ 0.1μm sediments into one labelled tube.

Table B.1 Settling times of each centrifuge for sedimentation of particles

Parameters	2μm		0.4μm		0.1μm	
T (°C)	20	25	20	25	20	25
η (poise)	0.01005	0.0091	0.01005	0.0091	0.01005	0.0091
R_1 (cm)	5.8	5.8	5.8	5.8	5.8	5.8
R_2 (cm)	16.1	16.1	16.1	16.1	16.1	16.1
N (rev/s)	41.66667	41.66667	68.33333	68.33333	68.33333	68.33333
r (cm)	0.0002	0.0002	0.00004	0.00004	0.00001	0.00001
ρ (g/cm^3)	2.5	2.5	2.5	2.5	2.5	2.5
ρ_0 (g/cm^3)	1	1	1	1	1	1
t_a (s)	14	14	35	35	35	35
t_d (s)	16	16	30	30	30	30
T (s)	~31	~30	~147	~137	~1713	~1555
T_{total} (s)	~45	~44	~182	~172	~1748	~1590
Note: *Setting Time,* $T_{total} = T + t_a$, due to the acceleration time included in the setting time in the centrifuge we used.						

3) Decant supernatant liquid from centrifuge tubes to 500mL beaker labelled with the sample name and '< 2μm';

4) Amalgomate ~ 2μm sediments from centrifuge tubes into one tube labelled with sample number and '2μm': first, using shaking and ultrasonic bath for about 15 minutes (Figure B.8 c)), and then using deionized water to remove all sediments;

5) Repeat 1) – 4) until all supernatant liquid (⩽ 2μm) from gravity settling processed;

Note: If the supernatant liquid from gravity settling does not have enough material to repeat the process, fill the supernatant centrifuge tubes with deionized water up to 50 mL and then centrifuge them.

6) Centrifuge the final '2μm' tube by adding deionized water up to 50 mL, decant supernatant liquid, and place the tube in an oven at a temperature below 60 °C until dry (Figure B.9 a));

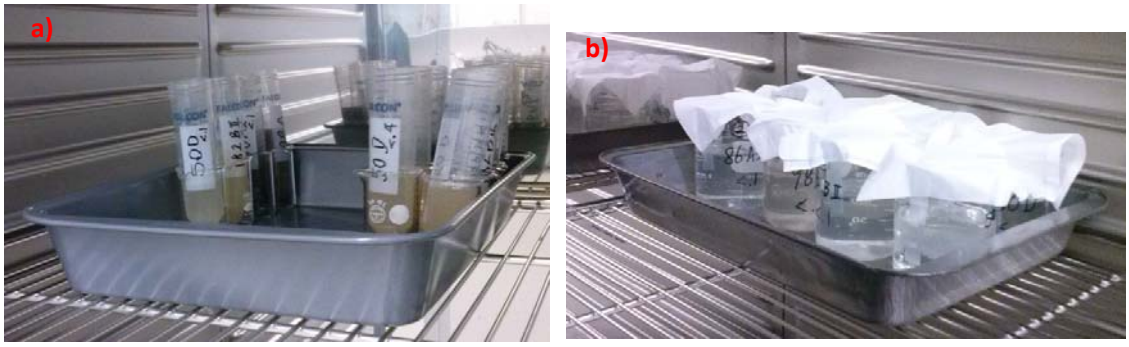

Figure B.9 a) Final '2μm', '0.4μm', and '0.1μm' tubes in the oven (< 60° C); **b)** Final < 0.1μm supernatant in the oven (< 60° C).

3. Centrifuging to separate < 0.4μm matters

It has the same procedure like centrifuging to separate < 2μm matters, except centrifuging at 4100 rpm for 3 minutes, as shown in Table 3.1.

4. Centrifuging to separate < 0.1μm matters

It has the same procedure like centrifuging to separate < 2μm matters, except centrifuging at 4100 rpm for 30 minutes, as shown in Table 3.1.

Finally, place the final supernatant beakers labelled with the sample name and '< 0.1μm' in the oven at a temperature below 60 °C until dry (Figure B.9 b)).

B.4 Weighting samples

Aims: - to weight clay-size fractions of 2μm, 0.4μm, and 0.1μm, in order to prepare for further quantitative analyses.

Equipment Required:

- Balance
- 30 mL Beaker as holder
- 50mL Conical Centrifuge Tubes

Procedure:

1. Balance a 30 mL beaker in the balance as 0 (Figure B.10 a));

2. Separately weight at least 10 new 50mL Conical Centrifuge Tubes by putting them in the holder of the 30 mL beaker and record their weights (Figure B.10 b));

3. Calculate the average of weight for each empty tube;

4. Separately weight the sample tubes with the fractions of 2μm, 0.4μm, and 0.1μm, in which the fraction samples get dried enough, and record their weights (Figure B.10 c));

Figure B.10 a) Balancing a 30 mL beaker as 0; **b)** Weighting empty tubes; **c)** Weighting sample tubes.

5. Calculate the weight of the fraction samples for each by the weight measured in step 4 subtracted by the mean weight of one empty tube (Figure B.11 & B.12).

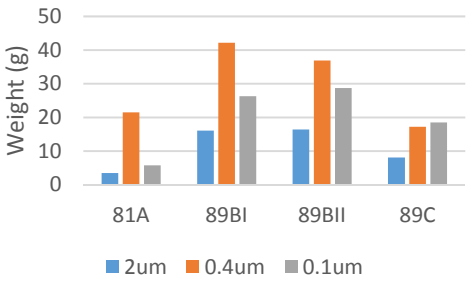

Figure B.11 The weight of Clay-size Fractions from the samples in Siwalik and MFT

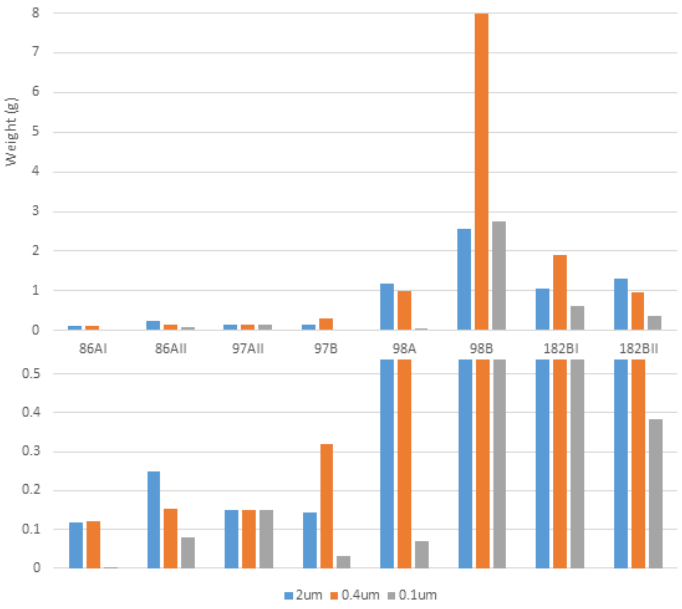

Figure B.12 The weight of clay-size fractions from the samples in MBT

Appendix C: Analytical Methods

C.1 X-Ray Diffraction Analysis

C.1.1 Preparation of Oriented and Non-Oriented Clay Aggregate

Aims: - to prepare both the oriented clay mineral aggregate and random orientation of the grains for further X-ray diffraction analysis by slide mounting and smear mount methods.

Equipment Required:

- Original Crushed Samples and Separation Fractions
- Balance
- Scoopula
- Frosted Slides (2.7 by 4.6 cm)
- Pen and Engraver Pen
- Deionized Water
- 30 mL Beakers
- Graduated Cylinder
- Stirring Rods
- Dropper Pipette
- Glass Dishes
- Spatula
- Kim Wipes Sheets
- Oven
- Fume Hood

Procedure:

Before and after use any equipment, clean it by using cleaning soap first and then acid alcohol.

1. The Slide Mounting Method

1) Label frosted slides on the glass side by using both pen and engraver pen, and place them in glass dishes (Figure C.1);

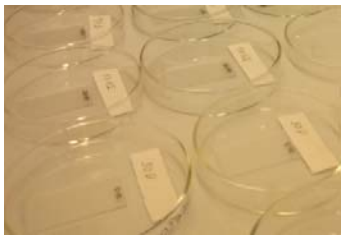

Figure C.1 Labelled frosted slides in glass dishes

2) Put all the dishes into the fume hood to wait for mounting;

3) Balance a 30 mL labelled beaker as 0, and weight about 100 mg sample by using scoopula to put sample into the beaker;

4) Measure 2 mL deionized water by graduated cylinder and add it into the beaker (Figure C.2);

Figure C.2 Adding 4 mL deionized water into 200 mg samples for mounting two slides each sample

5) Stir the mixture well until the sediment is in suspension;

6) Pipette around 4 mL of mixture onto the labelled slide (Figure C.3 a)-b)); Note: carefully drop to avoid overflowing.

7) Repeat 3) – 6) until all the samples have slide mounting;

8) Leave them to air-dry (Figure C.3 c)).

Figure C.3 a) Stirring the mixture; b) Slides Mounting; c) Air-drying sample slides in fume hood.

2. The Smear Mount Method

1) Put small amount sample powder onto a labelled frosted slide and add 2 or 3 drops of deionized water;

2) Mix them with spatula and evenly spread the mixture thin (Figure C.4 a));

3) Place these smear slides in glass dishes and leave them to air-dry in fume hood (Figure C.4 b)).

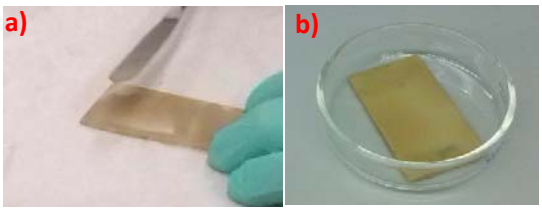

Figure C.4 a) Evenly spreading the mixture thin; **b)** Air-drying smear slides.

C.1.2 X-Ray Diffraction Analysis

Equipment Required:

- X-Ray Diffractometer
- Prepared glass and smear slides
- Slide holder
- Thick Glass
- Desiccator
- Ethylene glycol
- Graduated Cylinder
- Oven
- Long nose tweezers

Procedure:

1. Turn on the water cooling unit (XRD Chiller);

2. Switch certain slips based on the requirements for your analysis; in this case, two pairs of 0.3° and 0.15° slits were selected;

3. “Shut” the door and make sure that the light of XRD turns off;

4. Use a thick glass to make the slide flat on the holder (Figure C.5), open the door, and load sample slide with slide holder (Figure C.6);

5. Close the door and click “Window Open” button;

6. Set up “Power” with first 35 kV voltage followed by 30 mA current in gradually increased pace;

7. Using the software “MDI Datascan 4”, set up scan range properties like the following:
Start: 2°, End: 35°, Step: 0.05, and
Dwell: 1.5;

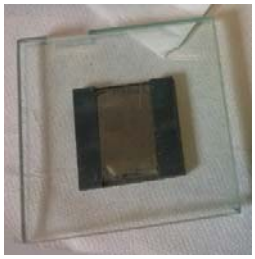

Figure C.5 Making slide sample flat

8. Set up file name using sample name and start run;

9. Repeat 3-5 and 7 to change sample slide until all the samples are completed;

10. “Shut” the door and take out the sample;

11. Close the door and gradually turn down the power in the order of first mA and second kV, which is opposite to the beginning.

Figure C.6 Loading slide sample into the X-Ray Diffractometer

Figure C.7 Ethylene glycol solvation in desiccator

C.1.3 Glycol and Heating Treatments

1. Ethylene Glycol Solvation

Before and after use any equipment, clean it by using cleaning soap first and then acid alcohol.

1) Measure 200 mL of ethylene glycol using Graduated Cylinder to add it into desiccator;

2) Insert a platform in the desiccator and place slide samples on it (Figure C.7);

3) Put the desiccator with a cover into the oven at about 60°C for 12 hours before XRD.

2. Heating Treatment

1) Set up the oven at about 550°C (Figure C.8 a));

2) Put the slide samples into the oven for about an hour before XRD (Figure C.8 b)).

Figure C.8 a) Setting up the oven at ~550°C; **b)** Taking out slide samples after an hour.

C.2 Scanning Electron Microscopy and Energy Dispersive Spectroscopy

C.2.1 Sample Preparation

Aims: - to prepare samples for SEM analysis by sample mounting and carbon coating to obtain a clear image.

Equipment Required:

- Non-separated Sample powder
- Deionized Water
- Scoopula
- Aluminium Specimen Mounts
- Aluminium Specimen Mounts holder
- Pen and Engraver Pen
- Dropper Pipette
- 30 mL Beakers
- Fume Hood

- LEICA EM CED 030 Carbon Coater

Procedure:

Before and after use any equipment, clean it by using cleaning soap first and then acid alcohol.

1. Sample Mounting

Figure C.9 Aluminium Specimen Mounts with 1/2 inch head and 1/8 inch pin.

1) Label the positions in the Aluminium Specimen Mounts holder with the sample numbers;

2) Place cleaned Aluminium Specimen Mounts on the positions of the holder (Figure C.9);

3) Add little sample powder into a labelled 30 mL beaker by using scoopula for each sample;

4) Add 5-6 drops of deionized water into the beaker;

5) Suck in and out to make the sample resolving into water well by using dropper pipette;

6) Pipette 3-4 drops of the mixture in the center of Aluminium Specimen Mount for each sample (Figure C.10);

7) Leave all the samples in the fume hood to dry overnight.

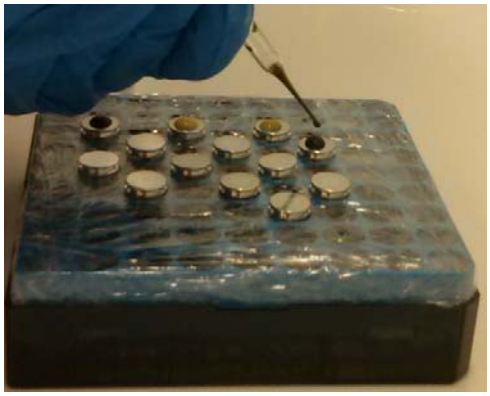

Figure C.10 Pipette drops of sample mixture in the center of Aluminium Specimen Mount

Figure C.11 LEICA EM CED 030 Carbon Coater. Image from Saint Mary University.

2. Carbon Coating

1) Mount a carbon source in the form of a thread in a vacuum system between two high-current electrical terminals;

2) Set up the vacuum with 10-15 Mbar;

3) Operate the carbon coater (Figure C.11). During the operation, the carbon source is heated to its evaporation temperature, so that a fine stream of carbon is deposited onto specimens.

C.2.2 Operation & Analysis

Aims: - to operate prepared samples for SEM/EDS analysis.

Equipment Required:

- Prepared Samples
- Disposable Gloves
- Tweezers
- SEM/EDS System of TESCAN MIRA3

Procedure:

1. Load seven prepared samples in the MIRA3 each time (Figure C.12). Note that samples should be handled with disposable gloves and tweezers to avoid degrading the SEM image because skin oil will outgas in the SEM vacuum system.

2. Set up the condition with the accelerating voltage of 20 kV, working distance of 17 mm, and the spot size of 3.4 nm in the software of MIRA3;

3. Click loading home stage and vent of vacuum, pump, and beam on;

4. Select sample, and adjust magnitude and focus;

Figure C.12 SEM/EDS System of TESCAN MIRA3. Image from tescan.com.

5. Select the position to do the EDS analysis following the instruction of the software "INCA-Point & ID", and save image;

6. Repeat steps 4-5 until all loaded samples are analyzed.

C.3 Transmission Electron Microscopy

Aims: - to operate prepared samples for TEM analysis.

Equipment Required:

- Separated Samples
- Conical Tubes
- Ultrasonic Bath
- Standard Micro Test Tubes
- Electrodeposited copper specimen grids
- Deionized Water
- Dropper Pipettes

- Pen/Pencil
- Plastic Dishes
- Filter Papers
- Tweezers
- Philips Tecnai-12 TEM system

Procedure:

1. Sample Preparation

1) For each dried separation sample, add the same volume of water with the volume of the sample in conical tube;

2) Use ultrasonic bath to make the sample dissolving well into the water;

3) Lay filter paper in each dish, separately put three electrodeposited copper specimen grids on the filter paper, and label sample names on the paper (Figure C.13);

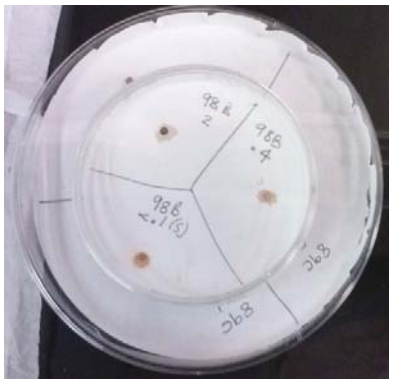

Figure C.13 Pipette separated sample dilution in electrodeposited copper specimen grid to dry

4) Dilute each separated sample to make the concentration of the dilution lower than 25% by taking one drop of the mixture into labelled standard micro test tube and adding 1-3 drops of deionized water;

5) Suck in and out to make the sample resolving into water well by using dropper pipette;

6) Pipette 1-2 drops in the grid for each sample and leave the dish to dry.

2. TEM Operation

The TEM system has already turned on with the high tension setting of 80 kV, as shown in Figure C.14.

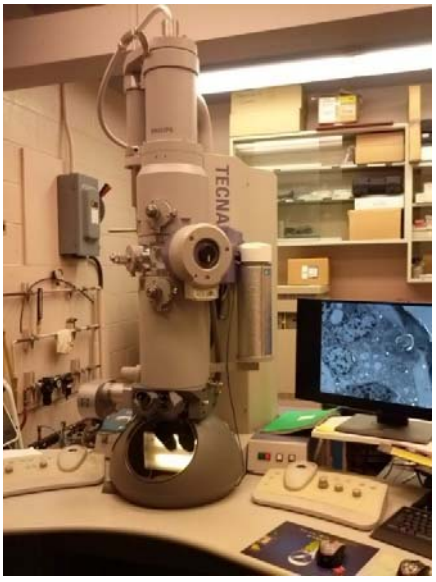

Figure C.14 Philips Tecnai-12 TEM

1) Click on the Col. Valves Closed icon to close Col. Valves;

2) Take specimen holder out from CompuStage; note that pull the holder straight out till it stops, then turn it clockwise to its stop, and pull it out;

3) Transfer one specimen on to the holder and Insert specimen holder (Figure C.15);

4) Select magnification at 6000x and click on the Col. Valves Closed icon to open Col. Valves;

5) Select the position and adjust magnification and focus to take a clear picture;

6) Save the image and move to the next position;

7) Repeat steps 5-6 until you have enough images for this specimen;

8) Repeat steps 1-7 for next specimen until all specimen are completed.

Figure C.15 Transfer one specimen on to the holder

Appendix D: Data Diagrams with Images

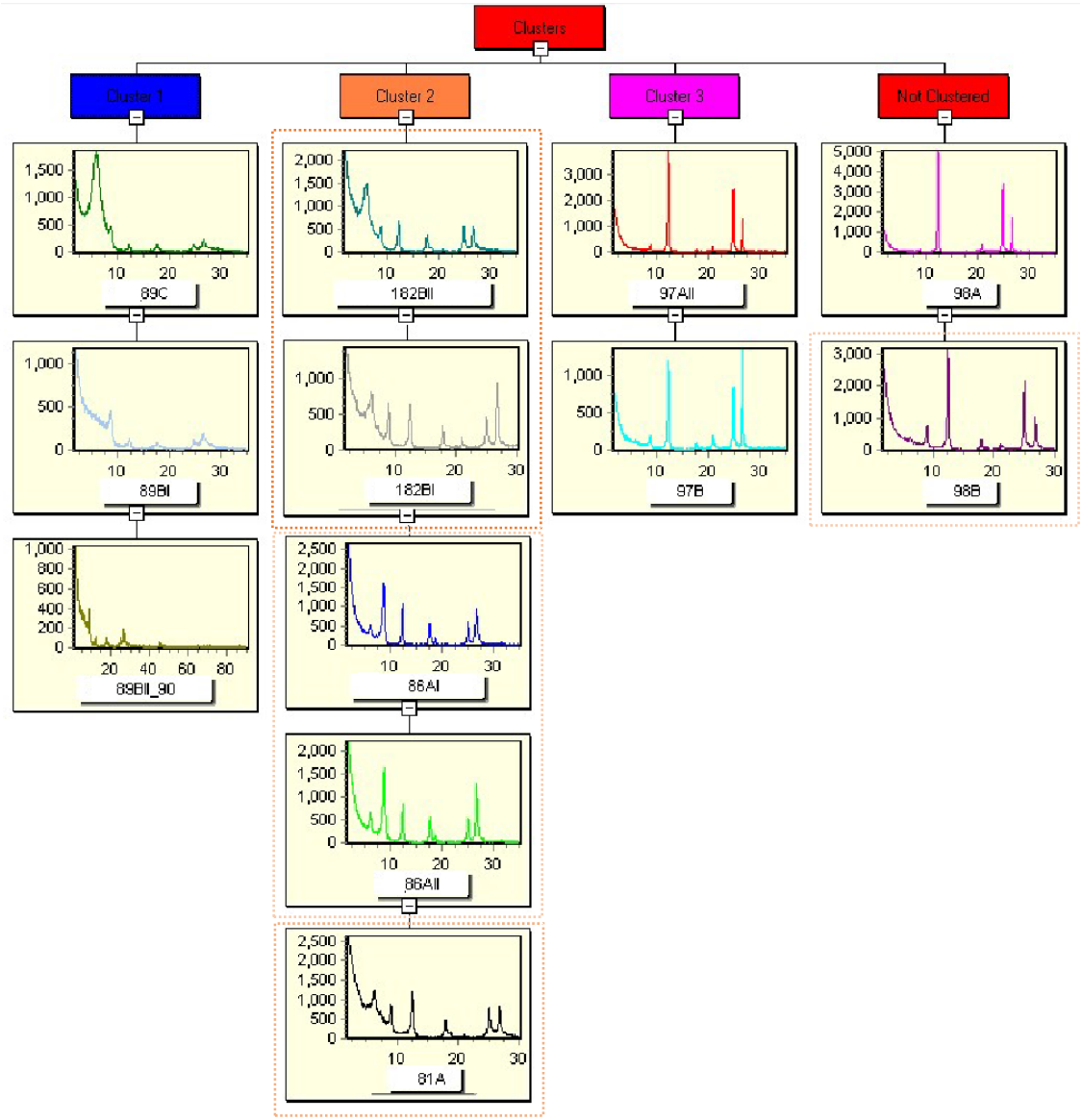

Figure C.1 Similarity between 12 clay samples based on clay minerals and associated minerals identified by XRD analysis. The orange round dot lines indicate subgroups. Note: 81A is from Sikkim.

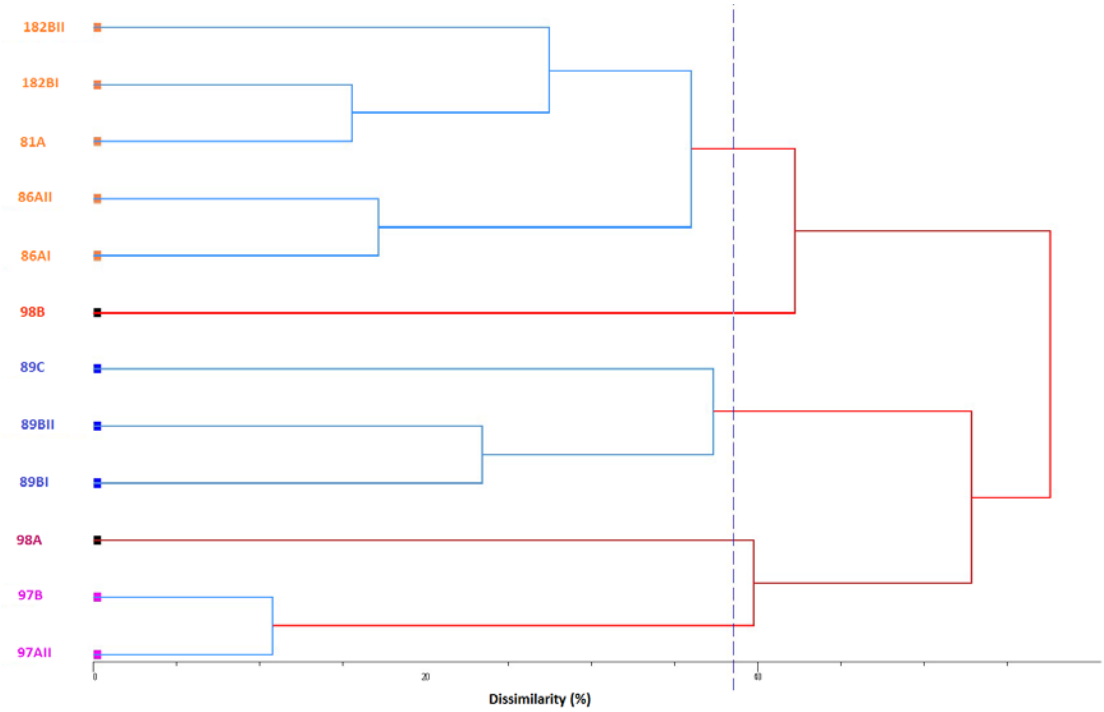

Figure C.2 Similarity between 12 clay samples based on clay minerals and associated minerals identified by XRD analysis. Note: the blue line means more similar where the red line is more dissimilar.
Note: 81A is from Sikkim.

X-Ray Diffractograms: Diuri Samples 86

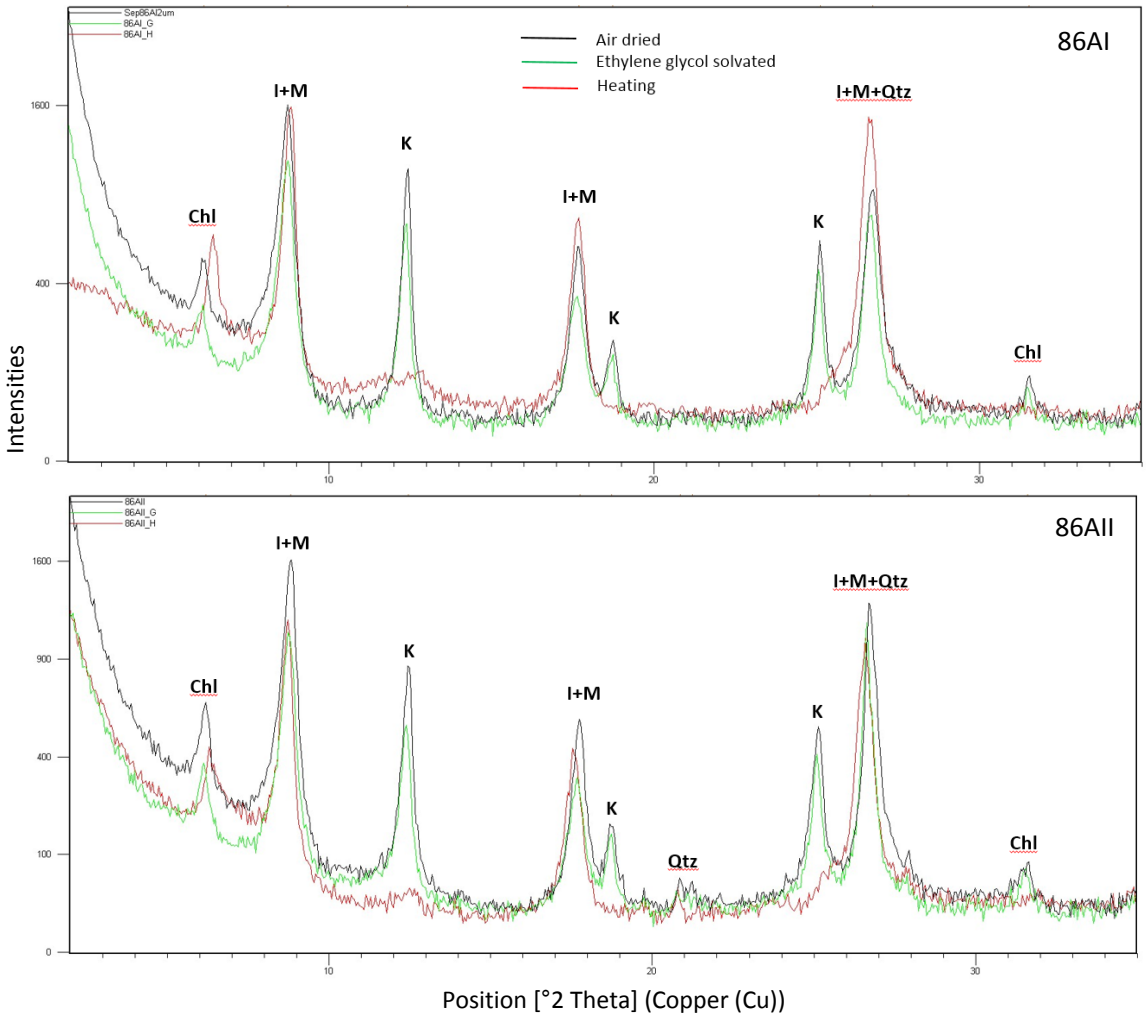

Figure C.3 X-Ray Diffractograms of Duiri samples 86 with identified clay and associated minerals

X-Ray Diffractograms: MBT samples 97 & 98A

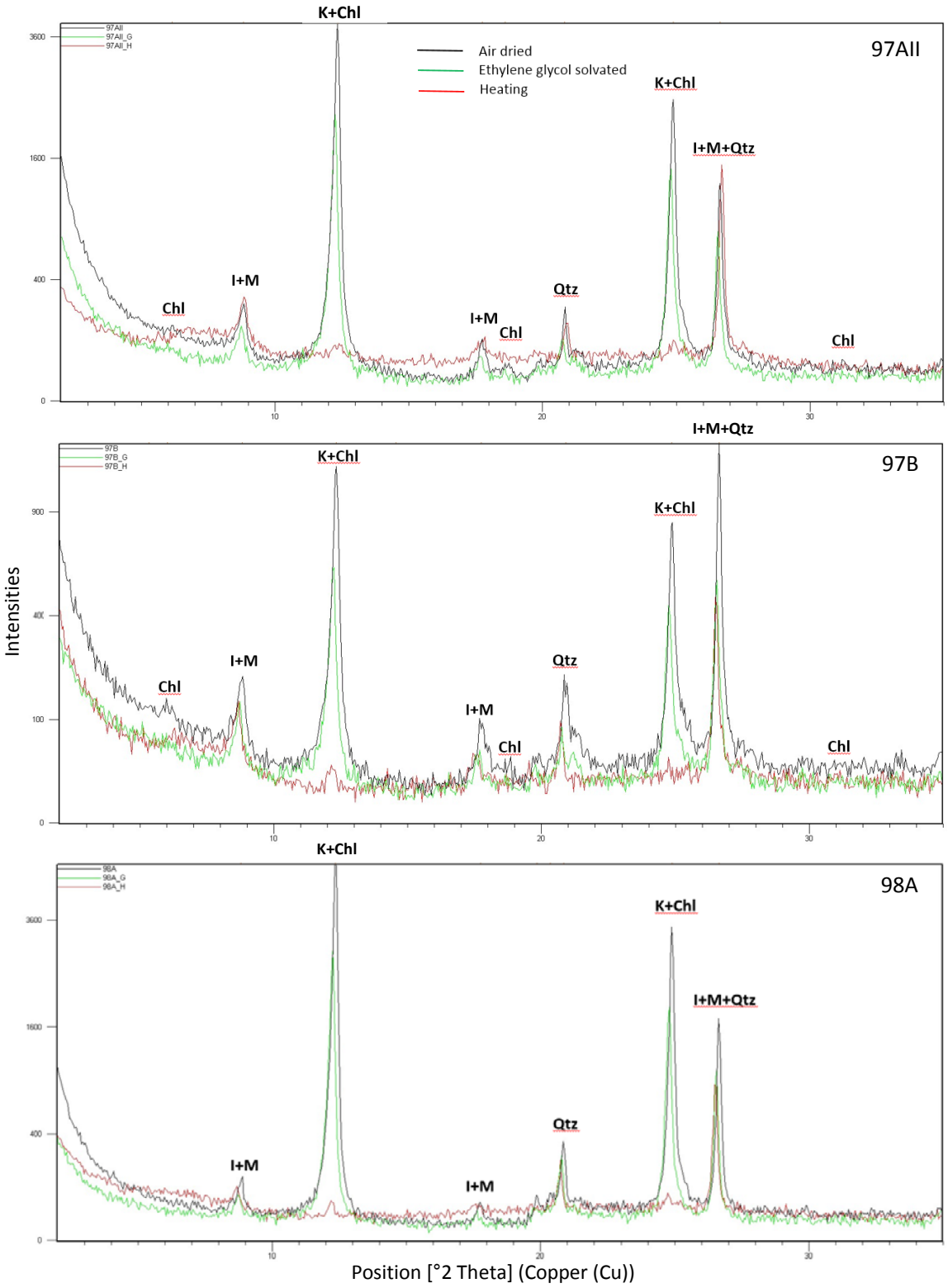

Figure C.4 X-Ray Diffractograms of MBT samples with identified clay and associated minerals

X-Ray Diffractograms: MBT sample 98B & Sikkim Siwalik 81A

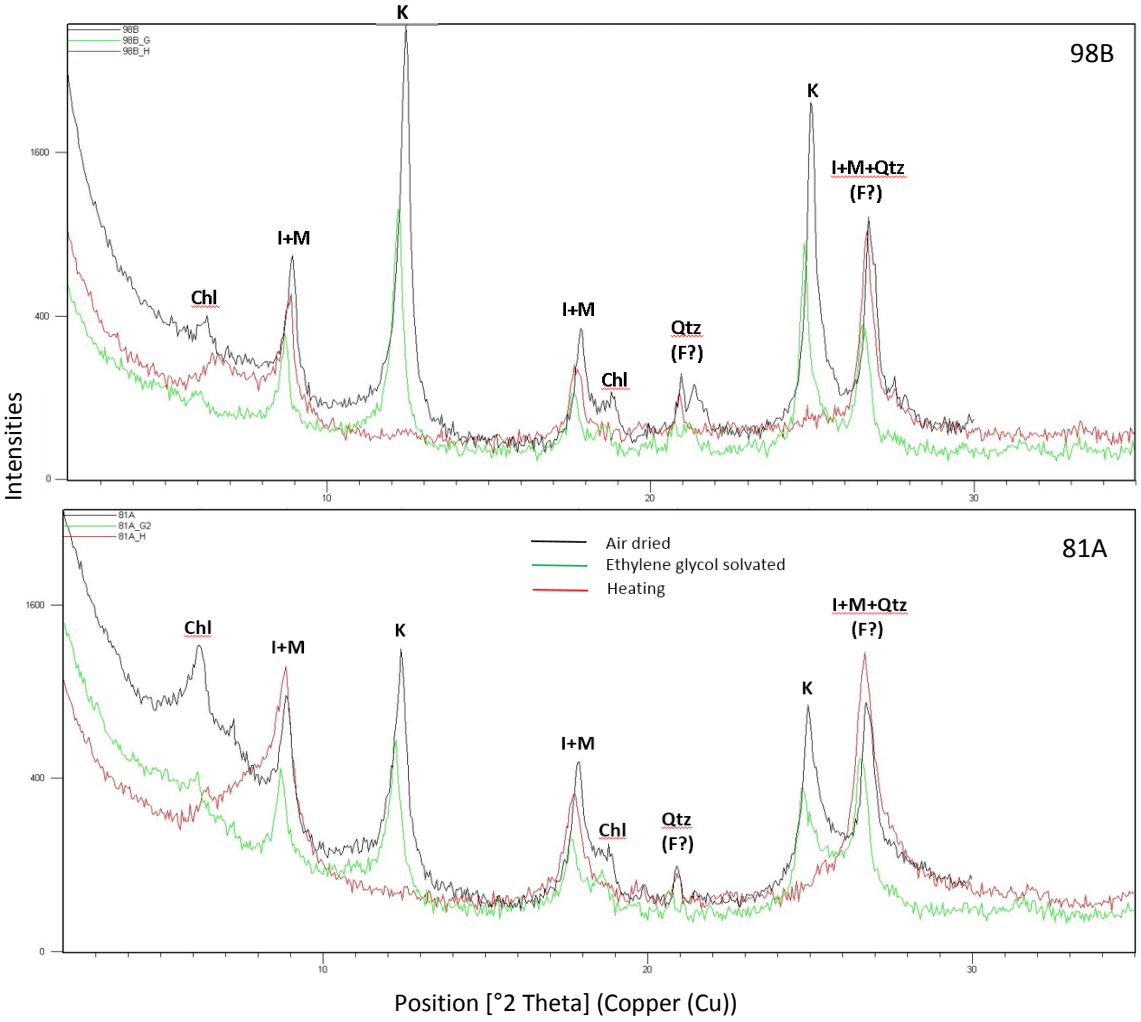

Figure C.5 X-Ray Diffractograms of MBT Samples 98B and Sikkim Siwalik 81A with identified clay and associated minerals

X-Ray Diffractograms: Siwalik samples 182

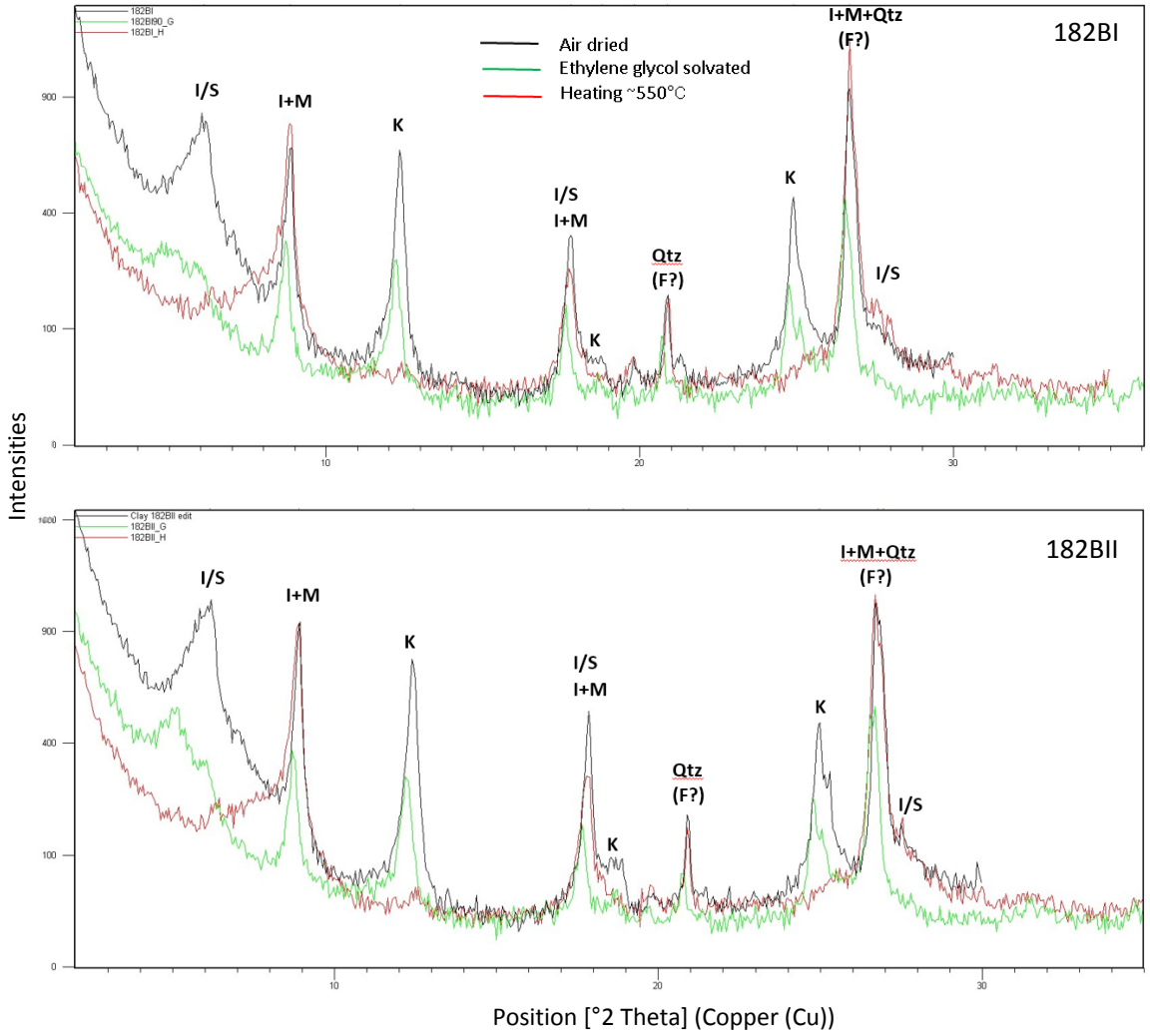

Figure C.6 X-Ray Diffractograms of Siwalik Samples 182 with identified clay and associated minerals

X-Ray Diffractograms: MFT Samples 89

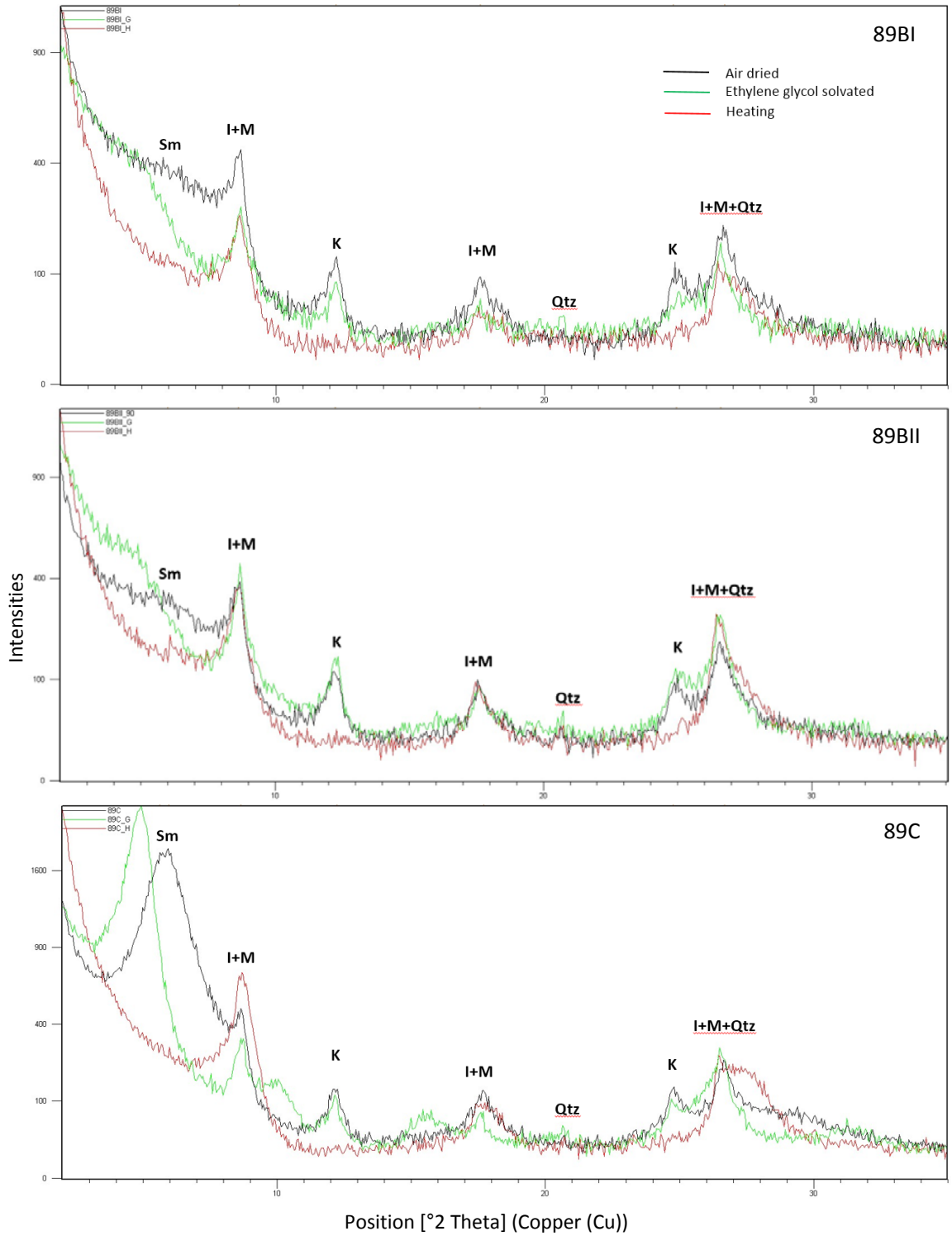

Figure C.7 X-Ray Diffractograms of MFT Samples 89 with identified clay and associated minerals

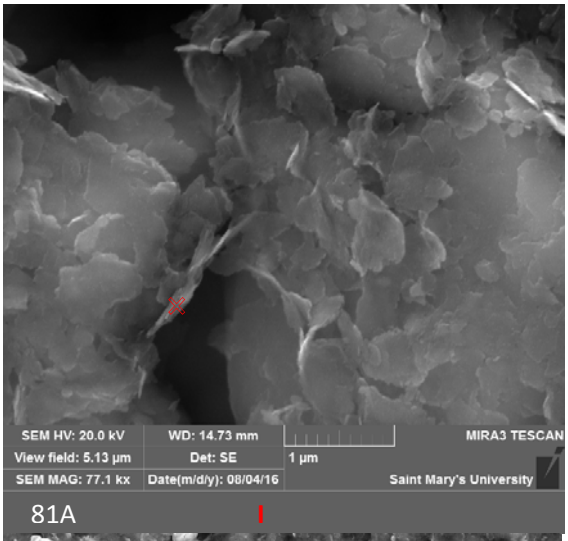

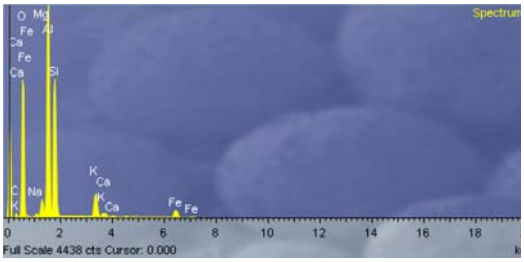

Point Composition labelled as a red cross in EDS

Based on XRD analysis, the circled point might be illite with needle-like shape, as well as the major elements of Si, Al and K, and a minor amount of Mg and Fe.

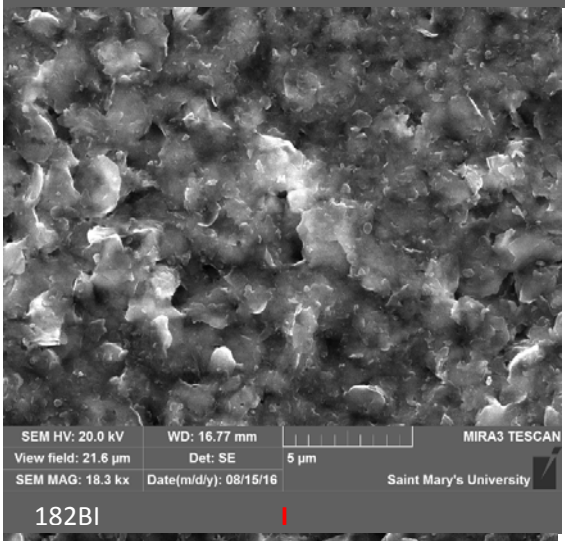

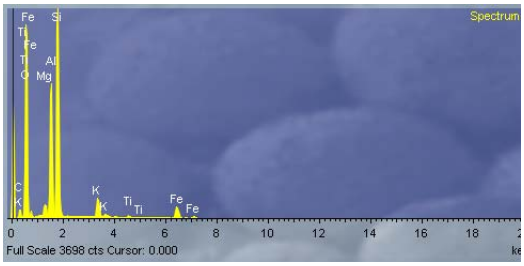

Average scan in EDS

Based on XRD analysis, the features of thin flakes with ribbon-like projections show that illite might be included in this sample.

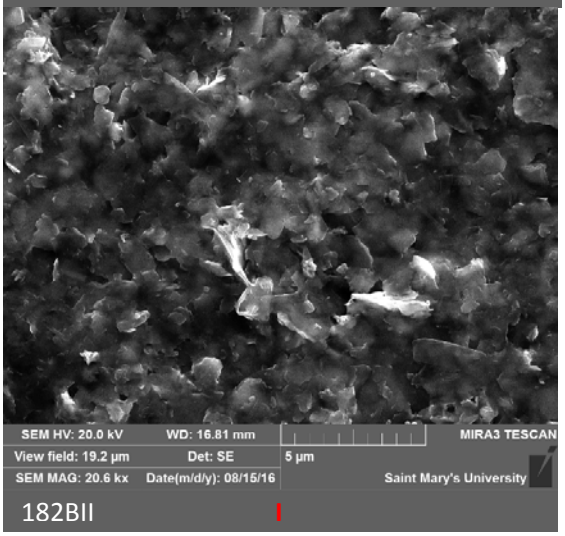

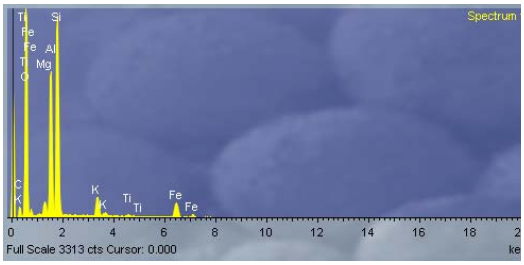

Average scan in EDS

Based on XRD analysis, the features of thin flakes with ribbon-like projections like 182BI show that illite might be included in this sample.

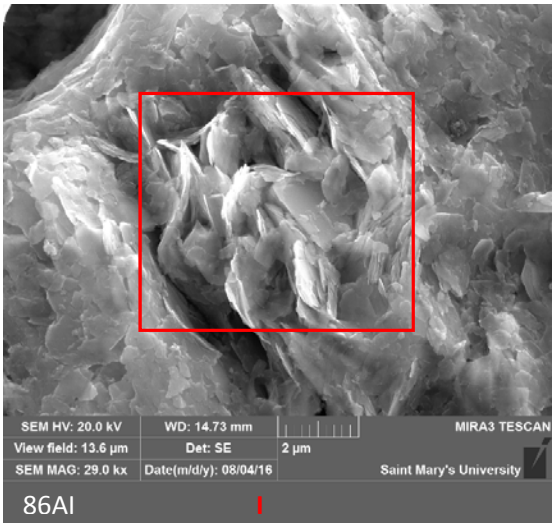

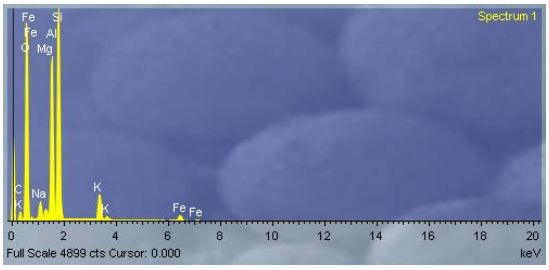

Average scan in the labelled rectangle in EDS

Based on XRD analysis, illite might be indicated by its flaky morphology and major elements mentioned before.

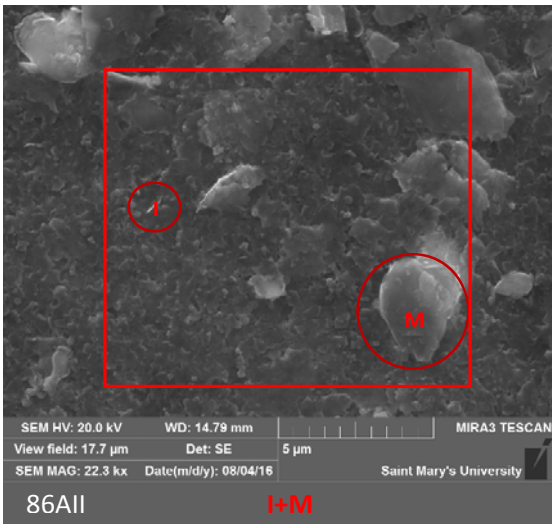

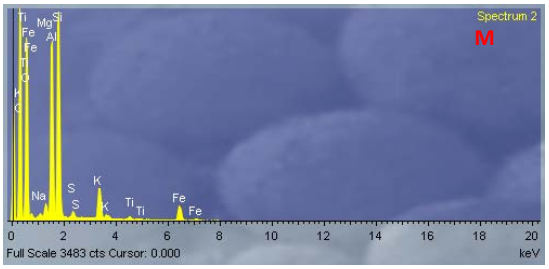

Point Composition labelled as the large red circle in EDS

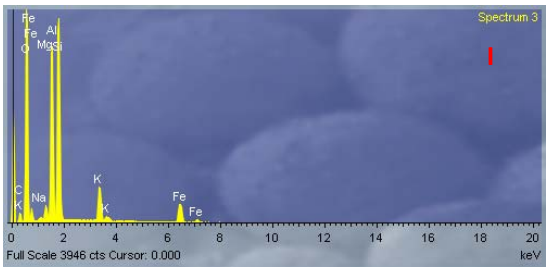

Point Composition labelled as the small red circle in EDS

Based on XRD analysis, round and oval shape labelled in the large red circle shows that glauconite, one of the mica minerals, is probably present Si, Al, Mg, K, Fe and Ti.

Besides, illite might be the mineral labelled in the small red circle showing the features of thin flakes with ribbon-like projections. Its EDS spectrum has similar major elements with mica.

According to the average scan in EDS, there might be two main minerals present in this sample, mica and illite.

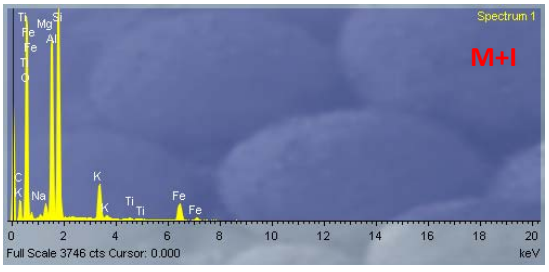

Average scan in the labelled rectangle in EDS

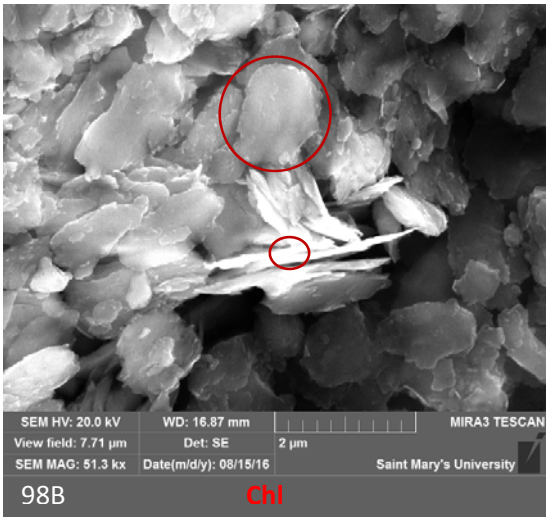

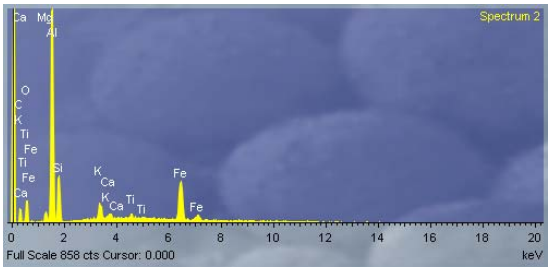

Point Composition labelled as the red circles in EDS

Based on XRD analysis, chlorite might be present with the features of small stacks of chlorite platelets, pseudo-hexagonal shape, and irregular edges. Also, iron-rich feature from EDS spectrum is another evidence for the presence of chlorite.

Figure C.8 SEM/EDS for Siwalik, Duiri, and MBT 98B separately showing Illite, Mica, and Chlorite minerals. Note: 81A is from Sikkim.

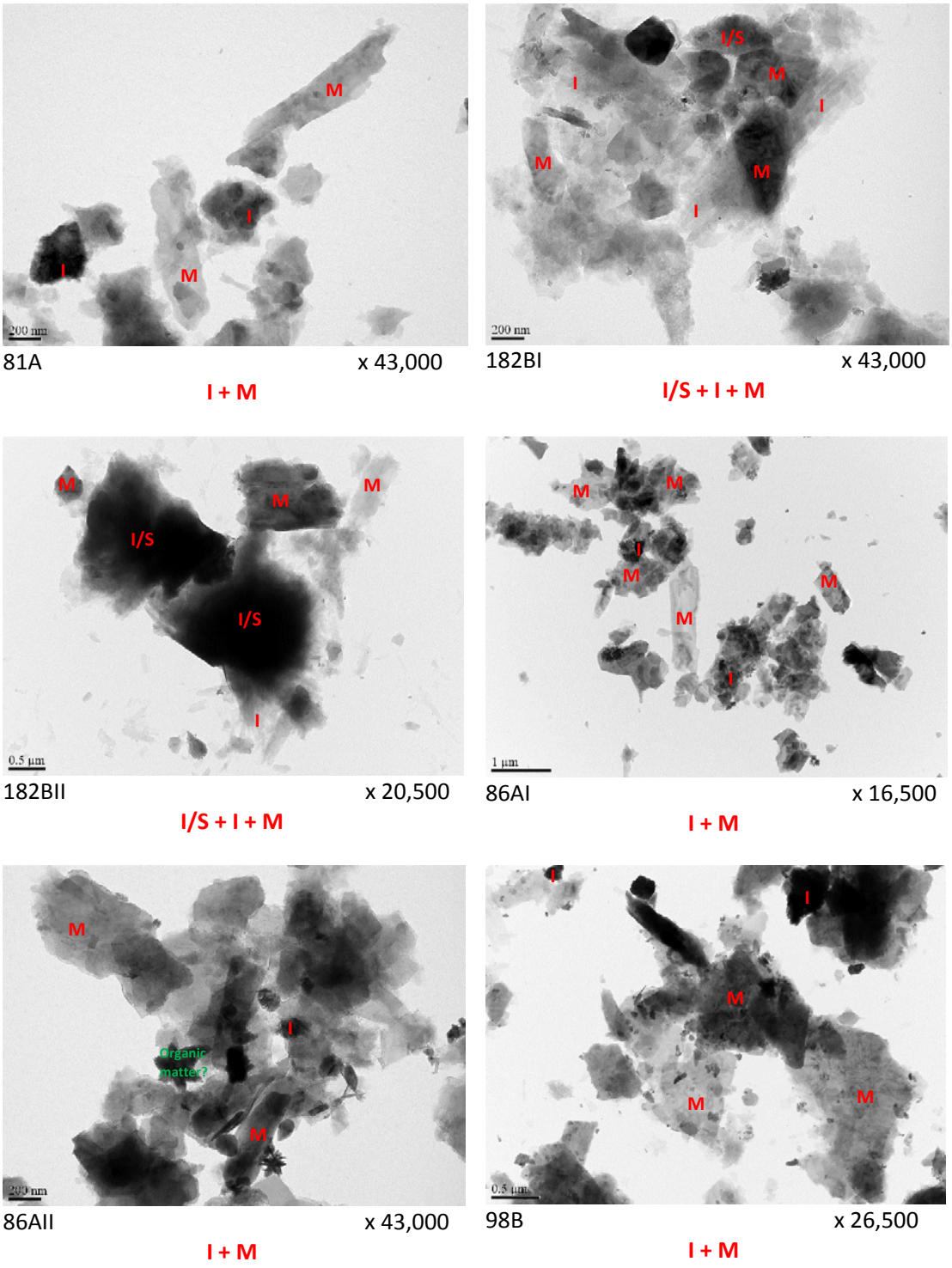

Figure C.9 TEM images for Siwalik, Duiri, and MBT 98B showing Illite, Illite-Smectite, and Mica minerals with micrographic features. Note: Illite consists of angular platy particles and some laths with relative smaller size while mica mainly shows large and platy particles with angular borders. However, Illite-Smectite has platy particles in addition to admixtures of smectite.

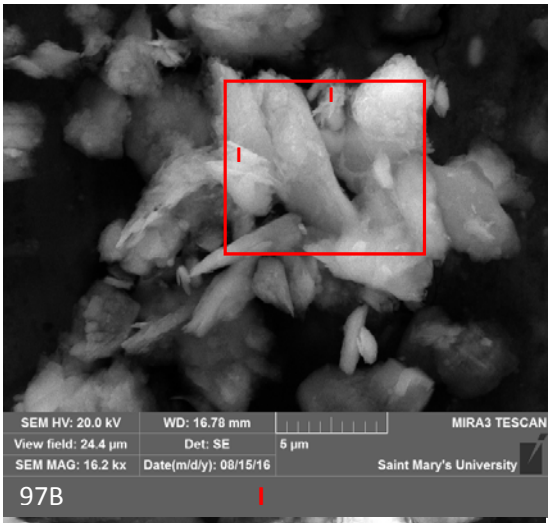

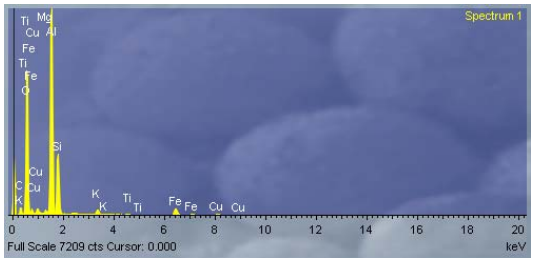

Average scan in the labelled rectangle in EDS

Based on XRD analysis, illite might be indicated by its thin and interwoven ribbon or needle shape.

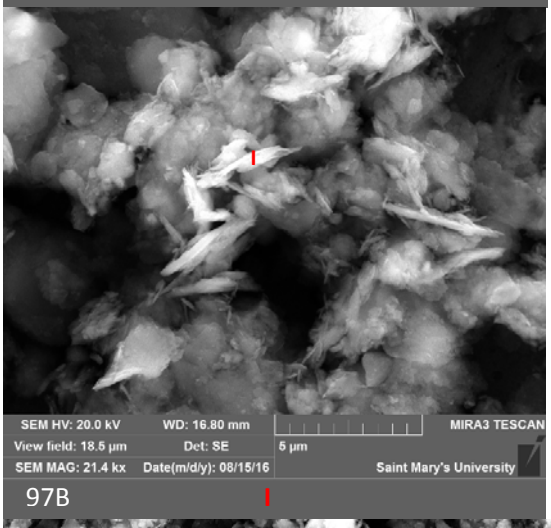

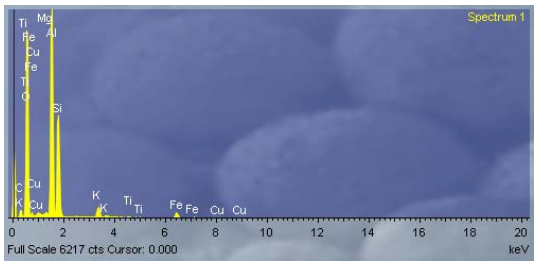

Point Composition in labelled position in EDS

Based on XRD analysis, illite might be indicated by its thin and interwoven ribbon or needle shape.

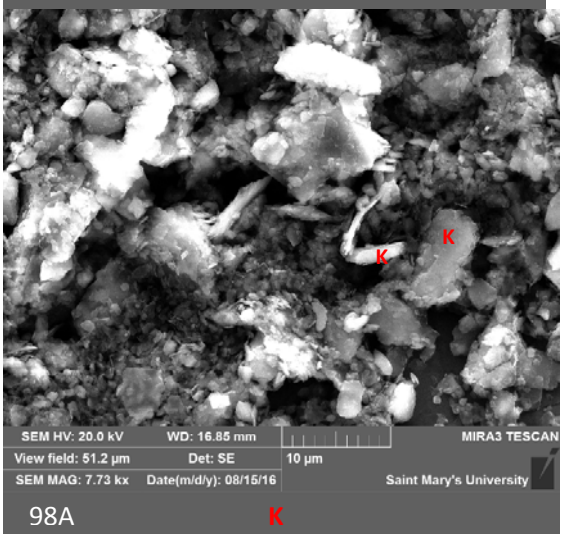

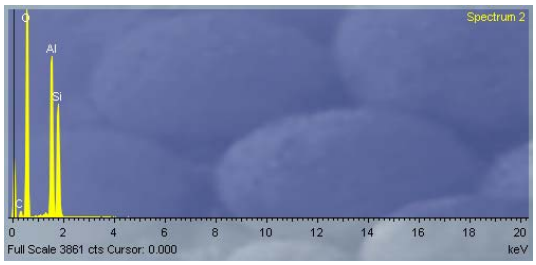

Point Composition in labelled position in EDS

Based on XRD analysis, kaolinite might be indicated by its blocky morphology and major elements of Si and Al.

Figure C.10 SEM images for MBT samples with EDS spectrums showing Illite and Kaolinite minerals

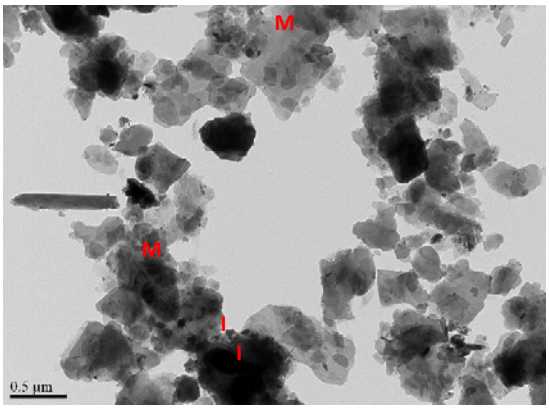

97AII x 26,500

I + M

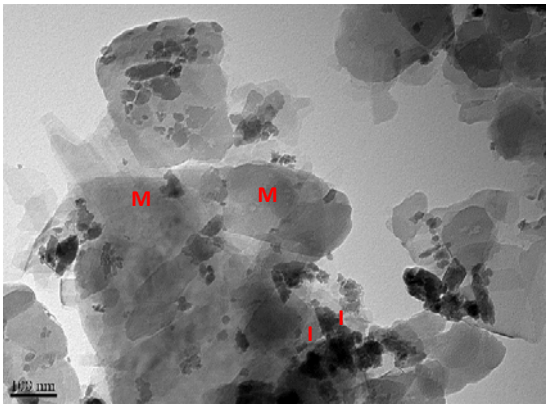

97B x 105,000

I + M

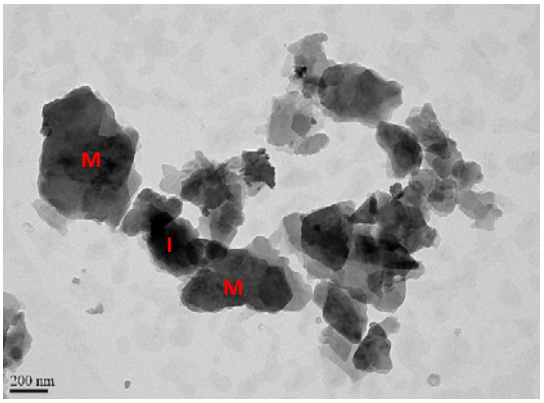

98A x 43,000

I + M

Figure C.11 TEM images for MBT samples showing Illite and Mica minerals with micrographic features. Note: Illite consists of angular platy particles and some laths with relative smaller size while mica mainly shows large and platy particles with angular borders. Note: 81A is from Sikkim.

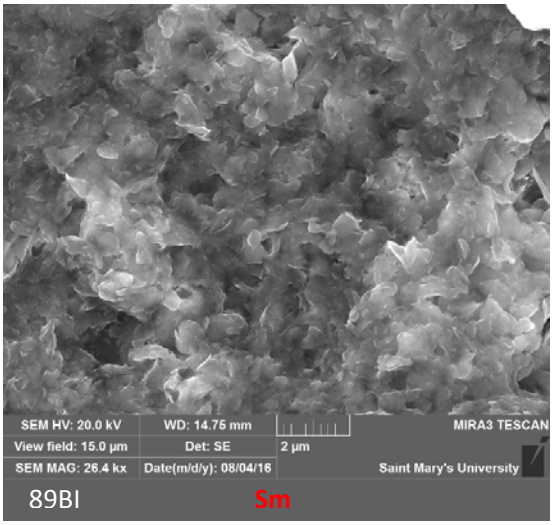

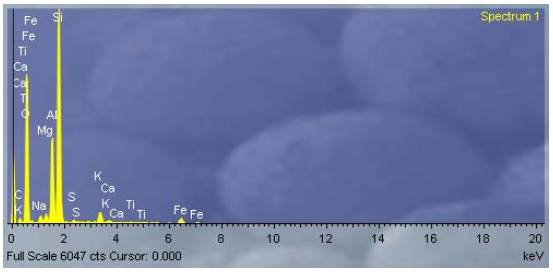

Average scan in EDS

Based on XRD analysis, slightly flaky smectite might be included in this sample with the major elements of Si, Al, Ca, Mg, Fe, and K.

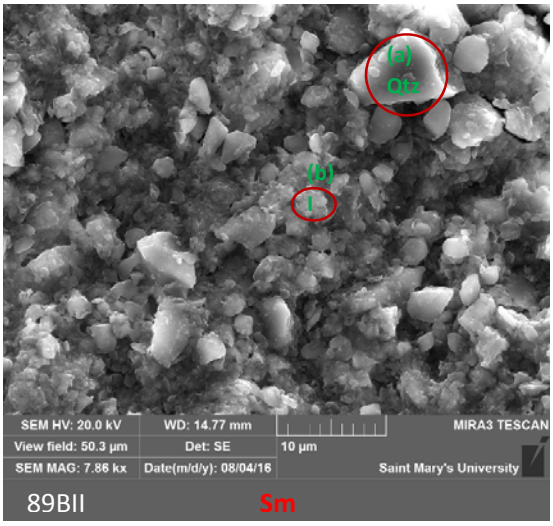

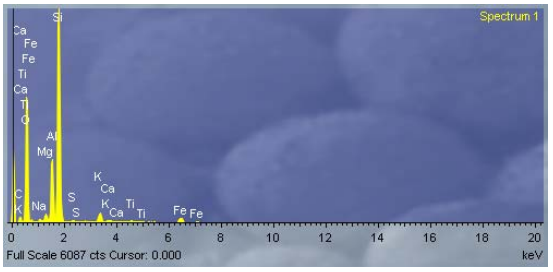

Average scan in EDS

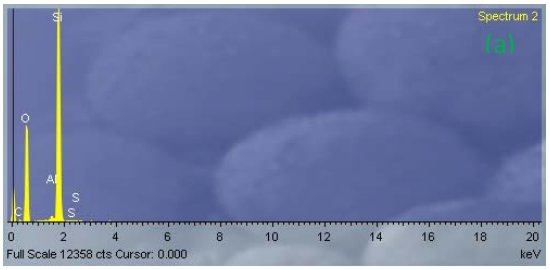

Point (a) Composition in EDS

According to the average scan in EDS, smectite may be included based on XRD analysis and its major elements.

From point analysis at (a), the main mineral is probably quartz while at point (b), illite may be included with thin flakes shape, the major elements of Si, Al and K, and a minor amount of Mg and Fe.

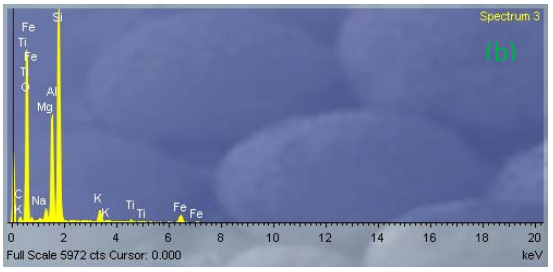

Point (b) Composition in EDS

Note: the red circles in the left SEM image locate the positions of point analysis.

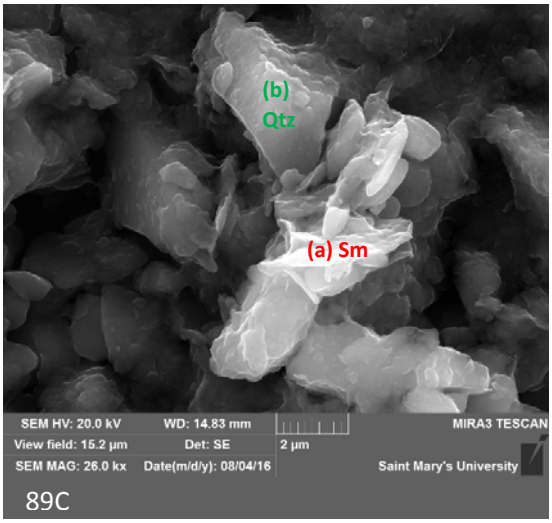

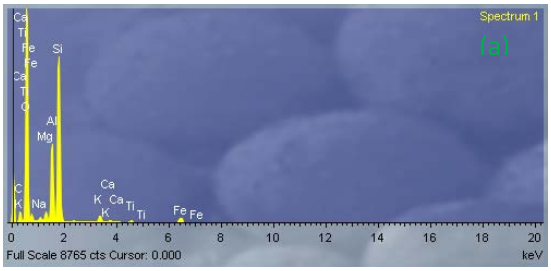

Point (a) Composition in EDS

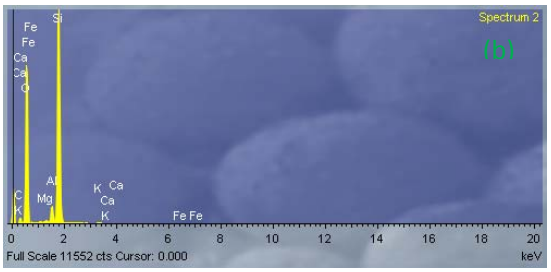

Point (b) Composition in EDS

Based on XRD analysis, slightly flaky smectite might be included in this sample with the major elements of Si, Al, Ca, Mg, Fe, and K at point (a). But quartz is probably included at point (b).

Figure C.12 SEM images for MFT samples 89 with EDS spectrums showing Smectites.
Note: 81A is from Sikkim.

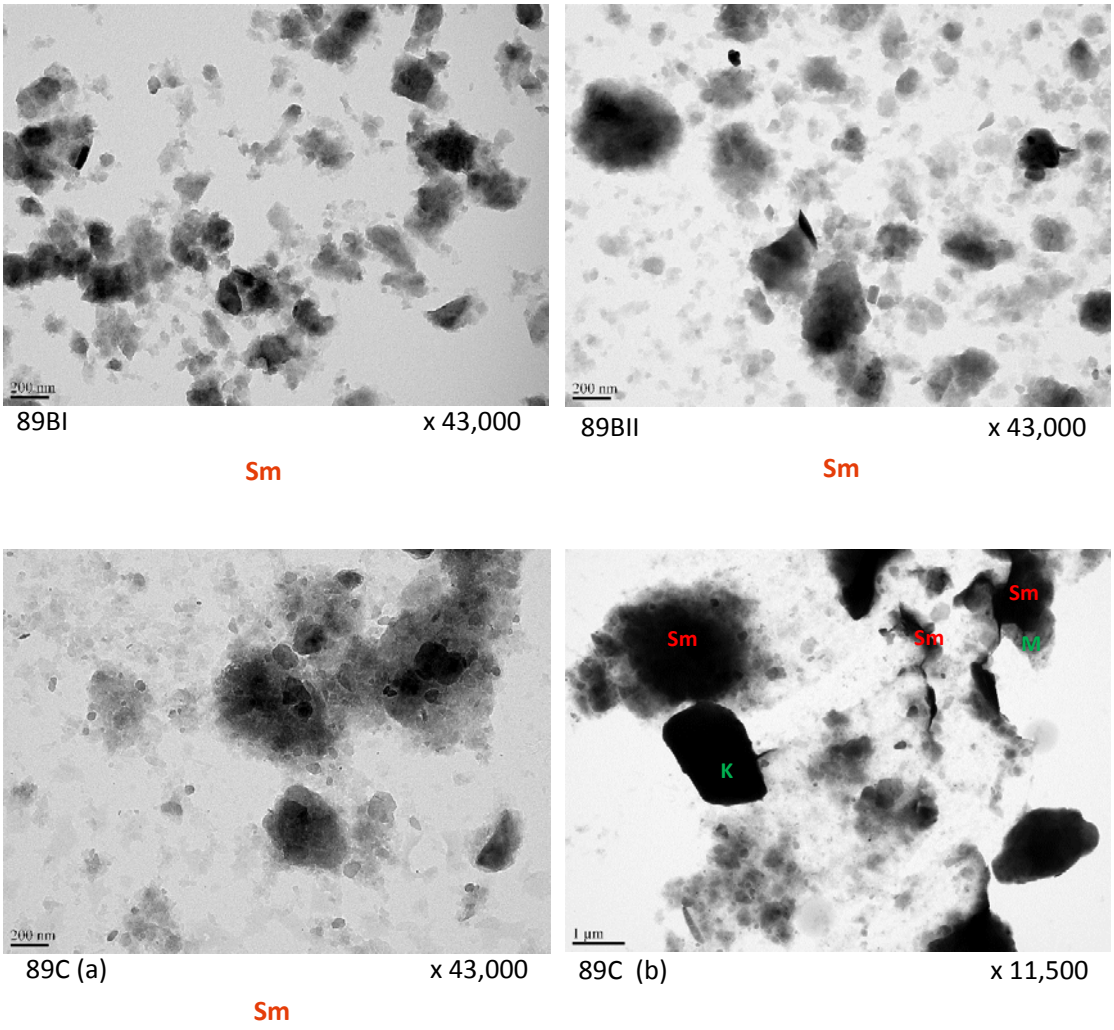

Figure C.13 TEM images for MFT samples 89 showing Smectites with micrographic features. Note: The amorphous admixtures in the TEM images of 89BI, 89BII, and 89C (a) might be smectite, which can be considered as aggregations of very small grains with a fluffy appearance. But in the TEM image of 89C (b), smectite might be identified by partly folded irregular lamellae, curled edges, or steep parts as darker colored spheres. In addition, kaolinite may be present with pseudo-hexagonal shape in 89C (b) while mica under smectite shows large and platy shape with angular borders. Note: 81A is from Sikkim.

Appendix E: Isotopic Data Table

Table E.1 Summary Table of Isotopic Data. The unit for all temperatures (T) in the table is ˚C. $\delta^{18}O$ and δD are the isotopic composition values of clay minerals while $\delta^{18}O_{K\text{-}W}$ and $\delta D_{K\text{-}W}$ are the isotopic composition values of meteoric waters. T in Sm refers to the temperature of clay formation based on smectite geothermometer while T in K is the temperature using kaolinite geothermometer. $\alpha_{H\text{-}W}$ refers to the hydrogen kaolinite-water fractionation whereas $\alpha_{O\text{-}W}$ refers to the oxygen kaolinite-water fractionation. O_T_k is the minimum temperature by using the $\delta^{18}O$ uncertainty (±0.2‰) while D_T_k is the maximum temperature by using the δD uncertainty (±3‰). Error in O_T_k is the temperature error obtained by the $\delta^{18}O$ uncertainty while Error in D_T_k is the temperature error obtained by the δD uncertainty. Using error propagation, the final temperature error is expressed as Error in T, which is ~ ± 1.6˚C.

Unit	Sample	$\delta^{18}O$ ‰	δD ‰	T in Sm	T in K	α_{H_K}	α_{O_K}	$\delta^{18}O_{k\text{-}w}$ ‰	$\delta D_{k\text{-}w}$‰	O_T_K	D_T_K	Error in O_T_K	Error in D_T_K	Error in T
Sikkim Siwalik	81A_0.1	11.0	-102.7	55.4	40.4	-30.08	21.33	-10.3	-72.6	39.3	41.6	1.01	1.28	1.63
	81A_0.4	10.9	-100.0	57.6	42.6	-29.77	20.93	-10.0	-70.3	41.6	43.9	1.03	1.30	1.66
	81A_2	10.7	-96.1	61.2	46.3	-29.26	20.30	-9.6	-66.8	45.2	47.6	1.07	1.35	1.72
Bhutan MFT	89BI_0.1	10.9	-99.7	57.8	42.8	-29.74	20.90	-10.0	-70.0	41.8	44.1	1.03	1.31	1.67
	89BI_0.4	11.6	-100.3	53.9	38.9	-30.30	21.60	-10.0	-70.0	37.9	40.1	1.00	1.26	1.60
	89BI_2	12.3	-100.6	50.4	35.2	-30.83	22.27	-10.0	-69.8	34.3	36.5	0.96	1.22	1.55
	89BII_0.1	11.2	-97.2	57.9	42.9	-29.73	20.89	-9.7	-67.5	41.8	44.2	1.03	1.31	1.67
	89BII_0.4	11.4	-95.8	57.8	42.8	-29.74	20.91	-9.5	-66.1	41.7	44.1	1.03	1.31	1.67
	89BII_2	12.0	-101.8	51.1	36.0	-30.73	22.14	-10.1	-71.1	35.0	37.2	0.97	1.22	1.56
	89C_0.1	15.1	-104.3	35.8	20.6	-33.19	25.23	-10.1	-71.1	19.8	21.7	0.83	1.05	1.34
	89C_0.4	15.1	-102.0	37.0	21.8	-32.99	24.98	-9.9	-69.1	20.9	22.8	0.84	1.06	1.36
	89C_2	14.9	-103.3	37.2	22.0	-32.96	24.94	-10.0	-70.3	21.1	23.0	0.84	1.06	1.36
Bhutan MBT	97B_0.4	12.5	-95.8	52.3	37.2	-30.54	21.90	-9.4	-65.2	36.2	38.4	0.98	1.24	1.58
	98A_0.4	13.4	-93.2	49.5	34.4	-30.96	22.43	-9.0	-62.2	33.5	35.6	0.95	1.21	1.54
	98B_0.4	12.8	-97.7	49.7	34.6	-30.93	22.40	-9.6	-66.8	33.6	35.8	0.96	1.21	1.54
Bhutan Siwalik	182BI_0.1	11.6	-105.6	50.7	35.6	-30.77	22.20	-10.6	-74.8	34.7	36.9	0.97	1.22	1.56
	182BI_0.4	11.6	-101.1	53.5	38.4	-30.37	21.69	-10.1	-70.7	37.4	39.6	0.99	1.25	1.60
	182BII_0.4	11.2	-103.7	53.8	38.7	-30.32	21.63	-10.4	-73.4	37.7	40.0	0.99	1.26	1.60
	Maximum			61.2	46.3			-9.0	-62.2					
	Minimum			35.8	20.6			-10.6	-74.8					

Table E.2 The data to reproduce the GMWL and LMWL lines in Figure 5.1

$\delta^{18}O$ ‰	δD_{GMWL} ‰	δD_{LMWL} ‰
-2.0	-5.13	-15.45
-3.0	-13.33	-22.69
-4.0	-21.53	-29.93
-5.0	-29.73	-37.17
-6.0	-37.93	-44.41
-7.0	-46.13	-51.65
-8.0	-54.33	-58.89
-9.0	-62.53	-66.13
-10.0	-70.73	-73.37
-11.0	-78.93	-80.61
-12.0	-87.13	-87.85
-13.0	-95.33	-95.09
-14.0	-103.53	-102.33
-15.0	-111.73	-109.57
-16.0	-119.93	-116.81
-17.0	-128.13	-124.05
-18.0	-136.33	-131.29
-19.0	-144.53	-138.53
-20.0	-152.73	-145.77